

VOLUME 36

NOVEMBER 1958

NUMBER 11

Canadian Journal of Physics

Editor: H. E. DUCKWORTH

Associate Editors:

- L. G. ELLIOTT, *Atomic Energy of Canada, Ltd., Chalk River*
J. S. FOSTER, *McGill University*
G. HERZBERG, *National Research Council of Canada*
L. LEPRINCE-RINGUET, *Ecole Polytechnique, Paris*
B. W. SARGENT, *Queen's University*
G. M. VOLKOFF, *University of British Columbia*
W. H. WATSON, *University of Toronto*
G. A. WOONTON, *McGill University*

Published by THE NATIONAL RESEARCH COUNCIL

OTTAWA

CANADA

CANADIAN JOURNAL OF PHYSICS

(Formerly Section A, Canadian Journal of Research)

Under the authority of the Chairman of the Committee of the Privy Council on Scientific and Industrial Research, the National Research Council issues THE CANADIAN JOURNAL OF PHYSICS and five other journals devoted to the publication, in English or French, of the results of original scientific research. Matters of general policy concerning these journals are the responsibility of a joint Editorial Board consisting of: members representing the National Research Council of Canada; the Editors of the Journals; and members representing the Royal Society of Canada and four other scientific societies.

EDITORIAL BOARD

Representatives of the National Research Council

A. Gauthier, *University of Montreal*
R. B. Miller, *University of Alberta*

H. G. Thode, *McMaster University*
D. L. Thomson, *McGill University*

Editors of the Journals

D. L. Bailey, *University of Toronto*
T. W. M. Cameron, *Macdonald College*
H. E. Duckworth, *McMaster University*

K. A. C. Elliott, *Montreal Neurological Institute*
Léo Marion, *National Research Council*
R. G. E. Murray, *University of Western Ontario*

Representatives of Societies

D. L. Bailey, *University of Toronto*
Royal Society of Canada
T. W. M. Cameron, *Macdonald College*
Royal Society of Canada
H. E. Duckworth, *McMaster University*
Royal Society of Canada
Canadian Association of Physicists

K. A. C. Elliott, *Montreal Neurological Institute*
Canadian Physiological Society
P. R. Gendron, *University of Ottawa*
Chemical Institute of Canada
R. G. E. Murray, *University of Western Ontario*
Canadian Society of Microbiologists
T. Thorvaldson, *University of Saskatchewan*
Royal Society of Canada

Ex officio

Léo Marion (Editor-in-Chief), *National Research Council*
J. B. Marshall (Administration and Awards), *National Research Council*

Manuscripts for publication should be submitted to Dr. H. E. Duckworth, Editor, Canadian Journal of Physics, Hamilton College, McMaster University, Hamilton, Ontario.

(For instructions on preparation of copy, see **Notes to Contributors** (inside back cover).)

Proof, correspondence concerning proof, and orders for reprints should be sent to the Manager, Editorial Office (Research Journals), Division of Administration and Awards, National Research Council, Ottawa 2, Canada.

Subscriptions, renewals, requests for single or back numbers, and all remittances should be sent to Division of Administration and Awards, National Research Council, Ottawa 2, Canada. Remittances should be made payable to the Receiver General of Canada, credit National Research Council.

The journals published, frequency of publication, and prices are:

Canadian Journal of Biochemistry and Physiology	Monthly	\$3.00 a year
Canadian Journal of Botany	Bimonthly	\$4.00 a year
Canadian Journal of Chemistry	Monthly	\$5.00 a year
Canadian Journal of Microbiology	Bimonthly	\$3.00 a year
Canadian Journal of Physics	Monthly	\$4.00 a year
Canadian Journal of Zoology	Bimonthly	\$3.00 a year

The price of regular single numbers of all journals is 75 cents.



Canadian Journal of Physics

Issued by THE NATIONAL RESEARCH COUNCIL OF CANADA

VOLUME 36

NOVEMBER 1958

NUMBER 11

ACTIVATION ENERGY FOR CREEP OF TIN¹

L. G. BONAR AND G. B. CRAIG

ABSTRACT

The literature reports values ranging from 8000 to 26,000 cal per g-atom for the activation energy for the creep of tin. The present investigation analyzed the results of constant stress creep tests during steady state creep, and by means of temperature cycling. A value of approximately 9000 cal per g-atom for the creep of high purity tin in the temperature range 300 to 350° K was obtained.

INTRODUCTION

The activation energy concept as applied to creep has received considerable attention in the past few years. The activation energies reported for creep of tin vary widely in the temperature range 300 to 500° K. Thus, below 360° K, values from 8000 to 23,000 cal per g-atom are reported. However, above approximately 360° K, all investigators agree on an activation energy in the vicinity of 21,000 cal per g-atom. Table I shows the values which have been reported, and also the values obtained in this investigation.

Dorn and co-workers (1957, 1955) claim that the activation energy below approximately 360° K is the same as the activation energy above this temperature. Breen and Weertman (1955, 1956, 1957), however, have shown clearly in their investigations that over the temperature range 298° K to ≈360° K the activation energy is 11,000 cal g-atom. This value agrees quite well with the analysis of the data of Tyte (1938) which was conducted by Breen and Weertman, and also by the authors. Tyte's data yield a value of about 8000 cal g-atom.

The present investigation, therefore, was conducted in the temperature range 300° K to 350° K.

EXPERIMENTAL PROCEDURE

Spectrographically pure tin (99.998%) and zone-refined tin (99.999% + estimated) were extruded into $\frac{1}{8}$ -in. diameter wire and tested using an Andrade-Chalmers (1932) constant stress, beam-type creep machine. Thermostated water baths maintained temperature within $\pm 0.5^\circ \text{C}$. Extensions were measured directly with cathetometers accurate to 0.01 and 0.001 cm.

¹Manuscript received June 10, 1958.

Contribution from the Department of Metallurgical Engineering, University of Toronto, Toronto, Ontario.

RESULTS

After the samples had entered the secondary stage of creep, the creep rate was determined. The logarithm of the creep rate was then plotted against the reciprocal of the absolute temperature. The slope of the line thus yielded the activation energy divided by the gas constant (Fig. 1).

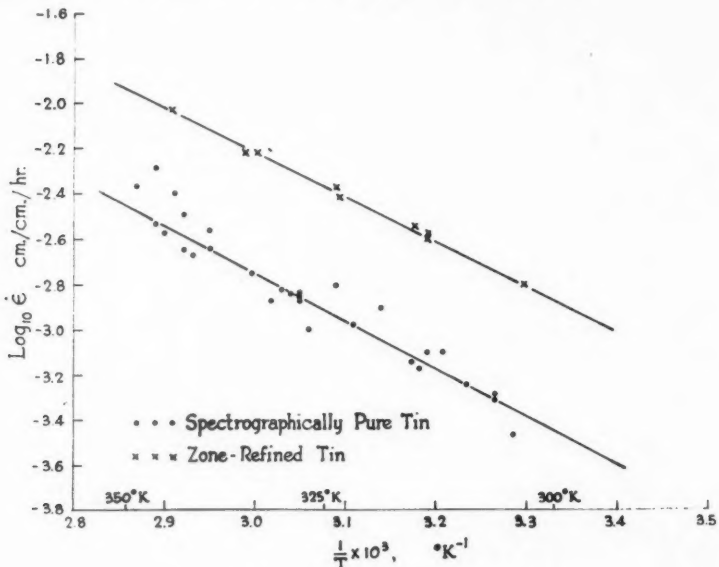


FIG. 1. Activation energy plot for creep of tin.

The method of temperature cycling developed by Frenkel, Sherby, and Dorn (1955) was also employed. A typical creep curve resulting from this procedure is shown in Fig. 2. The activation energies could then be calculated according to the formula

$$\Delta H = [R \log_e (\dot{\epsilon}_1 / \dot{\epsilon}_2)] / (1/T_1 - 1/T_2),$$

ΔH = activation energy,

$\dot{\epsilon}_1$ = creep rate before change of temperature,

$\dot{\epsilon}_2$ = creep rate after change of temperature,

T_1 = temperature before change,

T_2 = temperature after change,

R = gas constant.

Only one run was completed successfully on the zone-refined tin owing to difficulty with excessive grain growth which occurred at room temperature after extrusion.

The experimental results are recorded in Table I.

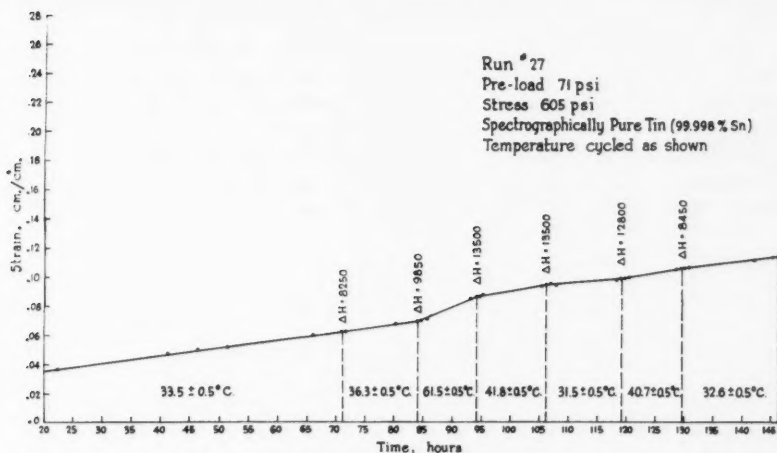


FIG. 2. Typical creep curve determined by the temperature cycling method.

TABLE I
ACTIVATION ENERGY FOR THE CREEP OF TIN

Activation energy, cal/g-atom	Reference	Temperature, °K	Remarks
23,300	1	320-336	26 tests, 99.4% Sn. Polycrystals
22,700	1	351-394	34 tests, 99.4% Sn. Single crystals
21,000	2	298-478	
19,000	3	453-498	Grain boundary shear. Analysis by 2 and 4
11,000	4	298-=360	99.9% Sn. Break in curve
26,000	4	=360-490	99.9% Sn. Break in curve
8,000	5	292-343	Analysis by authors and by 4. Break as for 4
17,400	6		Quoted by 4. Grain boundary relaxation
19,000	7	298-373	Single crystals. Break in curve. 99.99% Sn
11,000	10	298-403	Single crystals. Break in curve. 99.99% Sn
22,000	10	403-490	Single crystals. Break in curve. 99.99% Sn
12,000	11	298-393	Single crystals in compression. Break in curve. 99.99% Sn
24,500	11	393-490	Single crystals in compression. Break in curve. 99.99% Sn
9,600	(This investigation)	300-350	"spec." Sn. Log $\dot{\epsilon}$ vs. $1/T$
11,000 ± 3,000	"	300-350	"spec." Sn. Cycling. Average of 16 determinations
9,000	"	300-350	Zone-refined Sn. Log $\dot{\epsilon}$ vs. $1/T$
8,950 ± 1,500	"	300-350	Zone-refined Sn. Cycling. Average of 8 determinations

DISCUSSION

The four activation energies determined in this investigation are in satisfactory agreement. The slightly higher mean value for the cyclic temperature tests on "spec" pure tin can be partially accounted for if the data of Tyte (1938) and of Breen and Weertman (1955), as shown in Figs. 3 and 4, are considered. A break in the $\log_{10} \dot{\epsilon}$ vs. $1/T$ curves is obvious in each figure. This break occurs over a temperature range with the "exact" temperature of the break appearing to be stress dependent. Figure 1 of this investigation also

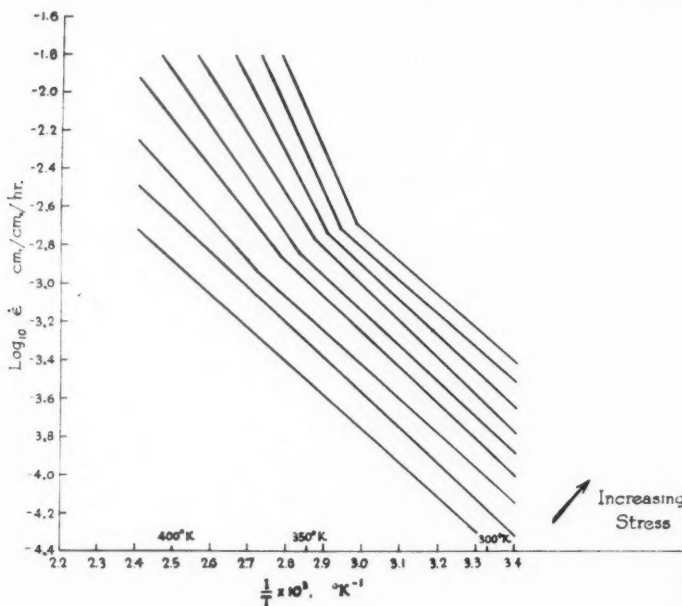


FIG. 3. Activation energy for creep of tin after Tyte (1938).

shows a slight upward curvature at one end. This upward curvature could explain the high mean value of 11,000 cal g-atom obtained for the spectrographically pure tin when the cyclic temperature method is used to obtain the activation energy. The investigations of Breen and Weertman (1956) and Weertman (1957) also show a break in the $\log_{10} \dot{\epsilon}$ vs. $1/T$ curves.

The activation energy for creep is not measurably affected by minor impurities, which is in accord with the work of Sherby and Dorn (1952).

CONCLUSIONS

The activation energy for the creep of high purity tin in the temperature range 300° K to 350° K is approximately 9000 cal g-atom.

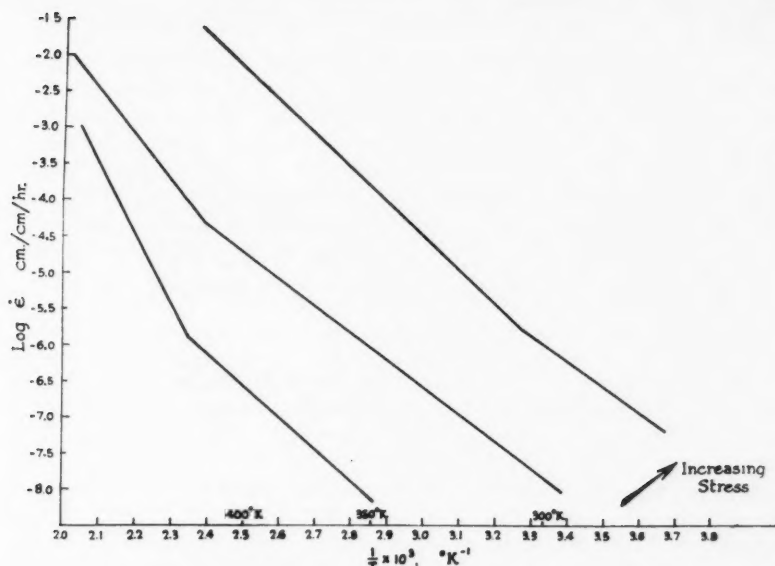


FIG. 4. Activation energy for creep of tin after Breen and Weertman (1955).

REFERENCES

- ANDRADE, E. N. da C. and CHALMERS, B. 1932. Proc. Roy. Soc. A, **138**, 348.
 BREEN, J. E. and WEERTMAN, J. 1955. Trans. AIME, **203**, 1230.
 FRENKEL, R. E., SHERBY, O. D., and DORN, J. E. 1955. Acta Met. **3**, 470.
 PUTTICK, K. E. and KING, R. 1952. J. Inst. Metals, **80**, 537.
 ROTHERHAM, L., SMITH, A. D. N., and GREENOUGH, G. B. 1951. J. Inst. Metals, **79**, 439.
 SEITZ, F. 1943. The physics of metals (McGraw-Hill Book Co.).
 SHERBY, O. D. and DORN, J. E. 1952. Trans. AIME, **194**, 959.
 TYTE, C. L. 1938. Proc. Phys. Soc. **50**, 153.
 WEERTMAN, J. 1957. J. Appl. Phys. **28**, 196.
 WEERTMAN, J. and BREEN, J. 1956. J. Appl. Phys. **27**, 1189.
 WISEMAN, C. D., SHERBY, O. D., and DORN, J. E. 1957. Trans. AIME, **209**, 57.

THE ELECTRON NEUTRINO ANGULAR CORRELATION IN THE BETA DECAY OF THE FREE NEUTRON¹

J. M. ROBSON

ABSTRACT

The electron neutrino angular correlation coefficient has been measured for the beta decay of the free neutron by measuring the momentum spectrum of the electrons emitted in a restricted angular range from the direction of the recoil protons. Experiments were made for two different angular ranges and yielded a best value for the angular correlation coefficient of +0.07 with an error of ± 0.12 . This error includes the statistical error in the form of its standard deviation and an allowance for all known systematic errors.

INTRODUCTION

Before the discovery that parity is not conserved in the beta-decay process, measurements of the electron neutrino angular correlation were essentially the only experimental approach to our understanding of the form of the interaction occurring in the beta-decay process. The discovery of parity non-conservation has provided new experimental approaches to this problem but measurements of the electron neutrino angular correlation still provide the most widely applicable method of determining the interaction. This paper describes a measurement of the angular correlation coefficient for the beta decay of the free neutron. Preliminary results were reported at the 1955 meeting of the Royal Society of Canada in Toronto, Ontario, and in abbreviated form were reported elsewhere (Robson 1955). Since those reports, additional data have been accumulated and a more careful investigation has been made of the systematic errors inherent in the measurements. The final result including all data is very similar to the value previously quoted though the fuller appreciation of the systematic errors has resulted in the final error being slightly larger.

Since the neutrino cannot be readily detected it is necessary to infer the electron neutrino angular correlation from measurements based on the detection of the electron and the recoil nucleus. There are several possible methods including a direct measurement of the momentum distribution of the recoil nuclei (Herrmannsfeldt *et al.* 1957; Good and Lauer 1957; Maxson *et al.* 1955), the angular distribution between the electrons and recoil nuclei (Rustad and Ruby 1955) and the momentum distribution of the electrons within a limited angular range from the direction of the recoil nuclei (Alford and Hamilton 1957). All these measurements are dependent on the electron neutrino angular correlation coefficient and therefore give estimates of its value. The present experiment was based on the last of the above-mentioned techniques. This

¹Manuscript received July 9, 1958.
Contribution from Physics Division, Atomic Energy of Canada Limited, Chalk River, Ontario.

Issued as A.E.C.L. No. 690.

method was chosen since it afforded the best method of reducing the effects of unavoidable background radiation.

The full theoretical expressions for the momentum distribution of the electrons from the beta decay of the neutron have been given by Jackson, Treiman, and Wyld (1957) for parity non-conservation and possible time reversal violation. Since in this experiment unpolarized neutrons were used, great simplifications occur in the formula and if we further simplify by using the notation C_i^2 to represent the full expressions $C_i^2 + C_i'^2$ for the coupling constants corresponding to parity non-violation and parity violation of the i th interaction, the formula becomes

$$n(p)dp d\Omega = CF(p)p^2(E_0 - E)^2 dp(1 + \alpha\beta \cos\vartheta) \sin\vartheta d\vartheta,$$

where β is the ratio of the electron velocity to the velocity of light,

ϑ is the angle between the electron and neutrino,

$d\Omega$ is the element of solid angle between the electron and neutrino,

α is the electron neutrino angular correlation coefficient.

$$\alpha = \frac{-C_S^2 + C_V^2 + C_T^2 - C_A^2}{C_S^2 + C_V^2 + 3C_T^2 + 3C_A^2}$$

and would equal -1 for a pure scalar interaction,

$+1$ for a pure vector interaction,

$+\frac{1}{3}$ for a pure tensor interaction,

$-\frac{1}{3}$ for a pure axial vector interaction.

In this expression for the momentum distribution, the so-called Fierz interference term has been neglected. Experiments on the ratio of K capture to positron emission in the decay of Na^{22} (Sherr and Miller 1954), and the shape of allowed spectra indicate that this interference term is small. The effect of its possible presence will be discussed in the discussion at the end of this paper.

The corresponding expression for the momentum distribution emitted at a fixed angle φ from the proton recoils can readily be obtained by applying the conservation of linear momentum between the electron, the neutrino, and the proton. It becomes:

$$n(p)dp d\Omega = Cp^2(E_0 - E)^2 dp[f_0(p) + \alpha f_1(p)] \frac{\sin\varphi d\varphi}{2}$$

where $f_0(p)$ and $f_1(p)$ are now functions of the electron momentum and the angle φ . Full expressions for $f_0(p)$ and $f_1(p)$ are given in the Appendix at the end of this paper.

If the apparatus detects events which have an angle φ between the directions of the proton and the electron with an efficiency $g(\varphi)$, the observed momentum spectrum of the electrons in coincidence with the protons will be:

$$\begin{aligned} n(p)dp &= CF(p)p^2(E_0 - E)^2 dp \int_0^\pi \left(f_0(p)g(\varphi) + \alpha f_1(p)g(\varphi) \right) \frac{\sin\varphi d\varphi}{2}, \\ &= CF(p)p^2(E_0 - E)^2 dp(F_0 + \alpha F_1), \end{aligned}$$

where F_0 and F_1 are functions of the electron momentum and are given in the Appendix. $F(p)$ is the Coulomb correction term for $Z = 1$.

Thus, provided $g(\varphi)$ is not independent of φ , a measurement of the momentum distribution of the electrons in coincidence with the protons can be compared with the above expression for this distribution and a value of a derived by the least squares method of fitting the experimental points to the theoretical curve. Two experiments were carried out with different experimental arrangements giving different functions for $g(\varphi)$. In the first, referred to hereafter as series I, $g(\varphi)$ was such that coincidences were recorded for φ between approximately 150° and 170° . In the second, referred to hereafter as series II, $g(\varphi)$ was such that the coincidences were recorded for φ between approximately 165° and 180° . The actual variations of $g(\varphi)$ with φ which resulted from these two experimental arrangements will be discussed later.

Section 2 of this paper will describe the experimental equipment used for these measurements with a general description in 2(a) followed by detailed descriptions of particular aspects of the apparatus in Sections 2(b) to 2(f). Section 3 describes the experimental procedure, Section 4 the theoretical spectrum shapes, and Section 5 the experimental results. These are then discussed in Section 6.

2. DESCRIPTION OF THE APPARATUS

2(a). GENERAL DESCRIPTION

The source of neutrons was a collimated beam from the NRX reactor obtained in a manner indicated in Fig. 1 and to be described in detail in Section 2(b). The collimated beam entered a large vacuum tank, passed through a center electrode assembly surrounding the part of the beam from which decay events were recorded, and then proceeded on to be finally stopped

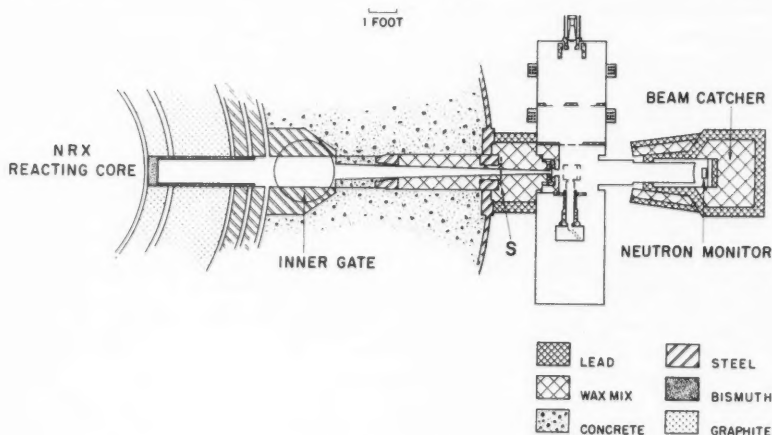


FIG. 1. Plan view of the collimation arrangements used to obtain the beam of neutrons from the NRX reactor, the experimental apparatus, and the beam catcher.

in a beam catcher. The details of the vacuum tank and its associated apparatus can be seen from Fig. 2, which shows a plan view of the equipment as used for the series II runs. The apparatus used for series I differed only in the arrangement of the baffles in the beta spectrometer and has been described elsewhere (Robson 1955).

The apparatus on the left side of Fig. 2 is a lens type beta spectrometer which selected the beta particles of the required momentum. It also defined the region of the beam from which decay electrons could be recorded and also the angles which these electrons had to subtend to its axis. It defined the size of the effective source of neutrons and played a dominant role in determining the form of the function $g(\varphi)$.

The center electrode assembly surrounding the effective source was held at a potential of +7 kv relative to the grounded vacuum tank. It was equipped with guard rings to maintain a uniform potential inside the assembly so that the protons resulting from neutron decay events in the effective source recoiled in an essentially field free region. Those which recoiled with an angle lying within about $\pm 10^\circ$ of the projection of the spectrometer axis were able to escape from the center electrode assembly through a gridded aperture $1\frac{1}{4}$ in. in diameter and were then accelerated and focused onto the first surface of an electron multiplier. Thus, if an electron was recorded by the counter of the beta spectrometer and the corresponding proton by the electron multiplier, the geometry of the apparatus ensured that the decay event had occurred in that part of the neutron beam located near the center of the center electrode assembly and that the angle between the electron and proton lay in the restricted range of approximately 150° to 170° for series I and 165° to 180° for series II. A more detailed discussion of these angles will be given in Section 4.

The main advantage of this experimental approach is that the two counters are located at a considerable distance away from the neutron beam and are therefore less affected by the high gamma radiation intensity which accompanies collimated neutron beams.

2(b). THE NEUTRON BEAM

The neutron beam was obtained with the aid of a series of collimators located in a horizontal beam hole of the NRX reactor as shown in Fig. 1. The hole through the reactor shield is about 12 in. in diameter and is equipped with a large iron stopcock known as the inner gate, which, when closed, placed a total thickness of 14 in. of iron in the path of the beam. This reduced the intensity of the beam to a level at which it was possible to work on the apparatus without radiation hazard. Behind this gate a bismuth plug was located at the extreme inner end of the beam hole adjacent to the reactor core. The plug was 4 in. thick with a $\frac{1}{2}$ in. thick cylindrical skirt. It attenuated the direct reactor gamma rays by a large factor and resulted in a reduction in the number of gamma rays in the final collimated beam of a factor of about three. Its presence only reduced the thermal neutron intensity of the beam by about 15%, presumably replacing those neutrons from the core which are scattered out of the beam with neutrons scattered from the reflector

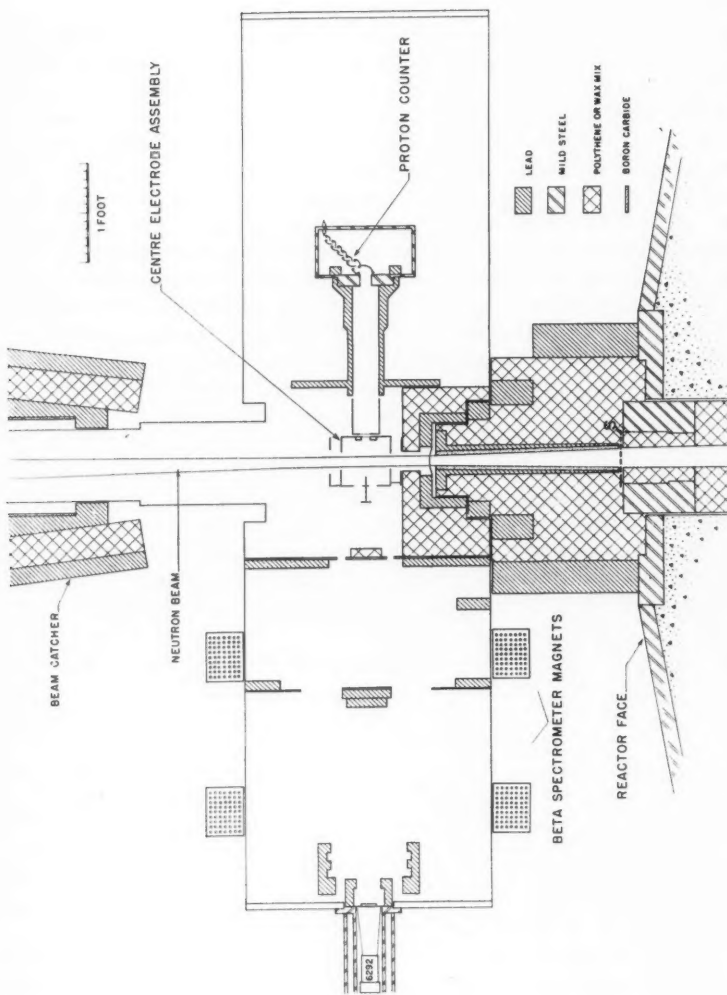


FIG. 2. Plan view of the apparatus mounted outside the face of the NRU reactor. The detailed arrangement of the spectrometer corresponds to the series II runs.

into the beam. Its effectiveness in reducing the fast neutrons in the beam is not known though presumably it considerably reduces the very high energy neutrons by inelastic scattering.

Outside of the inner gate a series of collimators tapered to a diameter of $1\frac{5}{8}$ in. at the entrance to the vacuum tank. These collimators looked at a diameter of 11 in. at the bismuth plug. Various materials were used in the collimators changing from ordinary concrete in the innermost region to a boron - lead oxide - wax mixture in the intermediate region and finally to an unlined boron carbide casting in the outer region near the experimental apparatus. At the point where the collimators emerge from the main reactor shield a slot was located into which a boron carbide shutter could be inserted to shut off the thermal neutrons in the beam without appreciably attenuating the fast neutrons or gamma rays. This slot is shown as S in Figs. 1 and 2.

The measured composition of the beam at the effective source region is listed in Table I.

TABLE I
COMPOSITION OF THE COLLIMATED BEAM

Component	Beam intensity Inner gate open	Beam intensity Inner gate closed
Thermal neutrons	$1.6 \times 10^{10}/\text{sec}$	$<2 \times 10^6/\text{sec}$
Neutrons between 0.3 ev and 15 ev	$\sim 4 \times 10^9/\text{sec}$	$\sim 6 \times 10^6/\text{sec}$
Neutrons above 15 ev	$\sim 4 \times 10^9/\text{sec}$	$\sim 8 \times 10^6/\text{sec}$
Neutrons above 200 kev	$\sim 1.5 \times 10^9/\text{sec}$	$\sim 3 \times 10^6/\text{sec}$
Gamma radiation	$\sim 10^4 \text{ r/hr}$	$\sim 1 \text{ r hr}$

2(c). THE BETA SPECTROMETER

The spectrometer was of the lens type using two thin electromagnets with their fields in the same direction along the axis. Its function was threefold: (i) to define the region of the neutron beam from which decay events could be detected, (ii) to accept electrons whose direction lay only within defined limits, and (iii) to select electrons with a known momentum. The first two requirements were met by using two annular ring entrance apertures which geometrically defined the region from which electrons could enter the spectrometer and the directions in which they must be travelling. The last requirement was met by the normal focusing properties of a spectrometer. The first of the entrance apertures was located in the central electrode assembly and the second about 12 inches away from the neutron beam.

The spectrometer was operated with as poor a resolution as was possible subject to the requirements that its behavior had to be in accordance with the theoretical prediction and that it could be accurately calibrated. The poor resolution was required to obtain as high a counting rate as possible and the accurate calibration was required to avoid the introduction of serious errors in the least squares fitting of the experimentally observed spectrum to the theoretical shape. These conditions were best met by using ring focusing in series I and point focusing in series II. To minimize the possibility of detecting scattered electrons of incorrect momentum, the vacuum tank was

considerably larger in radius than the maximum radius of an electron trajectory and the detector was arranged to respond only to electrons of approximately the correct momentum focused by the spectrometer.

The electron detector was a scintillation counter using anthracene mounted on a tapered lucite light pipe, oil-sealed to a selected DuMont type 6292 photomultiplier. The photomultiplier was selected for low dependence of the gain with counting rate and for resolution in this particular arrangement. It was shielded from the spectrometer magnetic field by a double iron-pipe magnetic-shield assembly. The pulses from the photomultiplier were passed through a single channel pulse height selector before being used for coincidences with the proton pulses from the electron multiplier. The window of the pulse height selector was arranged to cover the range of pulse amplitudes corresponding to electrons of the momentum selected by the spectrometer and was adjusted for each setting of the spectrometer. This pulse height selection served the double purpose of greatly reducing the unwanted background counting rate due to gamma rays and of further reducing the possibility of detecting scattered electrons from neutron decay events that did not have the correct momentum corresponding to the spectrometer setting. The setting of the window was made by two methods: (i) using electrons transmitted through the spectrometer from a source mounted at the sensitive volume at the center of the central electrode assembly and (ii) using electrons emitted from the surface of the central electrode assembly by stray radiation from the reactor beam. Figure 3(a) illustrates the differential spectrum of the pulses obtained using a radioactive source and Fig. 3(b) the differential spectrum using the reactor beam. In the latter case the continuous spectrum not associated with the peak corresponding to the electrons of correct momentum was subtracted by extrapolation under the peak. In both Figs. 3(a) and 3(b) the

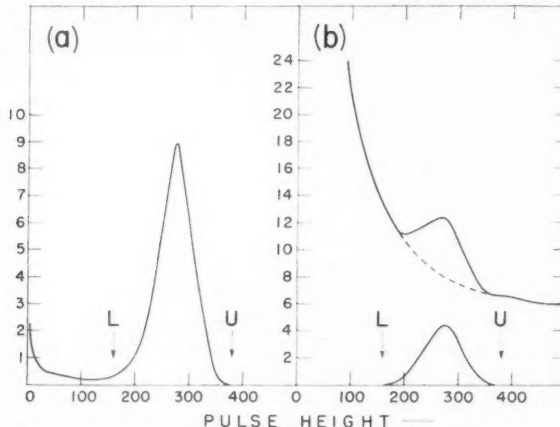


FIG. 3. Differential pulse height curves for the electron counter. "a" shows the spectrum from a radioactive source and "b" the spectrum obtained using electrons scattered from the surface of the central electrode assembly with the inner gate open.

lower and upper settings of the window are shown as L and U. It might be thought that settings obtained by the first method would be more reliable than those obtained by the second; however, the second method has the advantage that it is carried out under the identical conditions of operation used in the actual coincidence runs and, after it became apparent that the settings achieved by the two methods were very closely the same, more and more reliance was placed on the second method.

The obvious advantages of the use of pulse height selection on the output of the scintillation counter are obtained at the expense of a certain amount of uncertainty as to how constant was the fraction of the pulses within the window of all the pulses due to correct momentum electrons. Using curves of the type shown in Fig. 3(a) the lower setting was chosen on the basis of a constant fraction of 92% of the total area under the curve excluding the noise pulses. However, as more reliance was placed on the second method of setting the window there was a small uncertainty in the actual fraction achieved. This uncertainty was considerably less than the statistical error of the final counting rates and has been allowed for in the estimate of the final error.

Before the experiment was set up at the reactor face, consideration was given to a system of degaussing to eliminate the effect of the earth's magnetic field. It was discovered, however, that the earth's field was less than 0.1 gauss over the spectrometer when located at the reactor face. This low value was due to the steel girder construction of the building, which reduced the field generally throughout the building to subnormal values, and the presence of a large steel platform located about 10 feet above the apparatus and connected to the thick steel face of the reactor. Over the range of energies involved in this experiment this low residual field caused negligible distortion of an observed spectrum, and further degaussing was not employed.

Sources of Cs¹³⁷, Au¹⁹⁸, RdTh, and Hg²⁰³ were used to establish a momentum calibration for the spectrometer and to measure its resolution and effective solid angle. In these measurements the sources were mounted at the center of the sensitive volume and in area approximated to the cross-sectional area of the effective neutron source. They were held at the same potential as the central electrode assembly so that the 7-kv decelerating potential difference was present in the same manner as during the actual runs on neutron decay events. Details of the performance of the spectrometer as set up for series I and series II are listed in Table II. Figure 4 shows the electron distribution from the dominant $\Delta J = 2$ parity change transition of Cs¹³⁷ plotted as the ratio of the observed counts per unit momentum interval divided by $a_1 F p^2 q^2$, where p is the electron momentum, q the neutrino momentum, F the Coulomb correction factor, and a_1 the unique shape correction factor $q^2 L_1 + q L_1$ (Rose *et al.* 1953). The small contribution from the ground state transition and the background have been subtracted and the mean of the points normalized to unity. Perfect operation of the spectrometer would give $C = 1$ for all points; it can be seen that departures from this are small and considerably less than the errors in the rates obtained from neutron decay events which lay in the

TABLE II
CHARACTERISTICS OF THE BETA SPECTROMETER

	Series I	Series II
Geometric angles	$18^\circ \rightarrow 28^\circ$	$12^\circ \rightarrow 18^\circ$
Measured solid angle	2.5%	0.8%
Calculated solid angle*	2.6%	1.0%
Measured resolution (full width at half maximum)	7.7%	8.5%
Magnification	1.0	0.65
Diameter of counter (inches)	3.0	1.5

*The calculated solid angle is less than would be expected from the geometric angles of the entrance baffle system owing to the presence of structural supports not shown in Fig. 2 but required to locate the central parts of the various baffles.

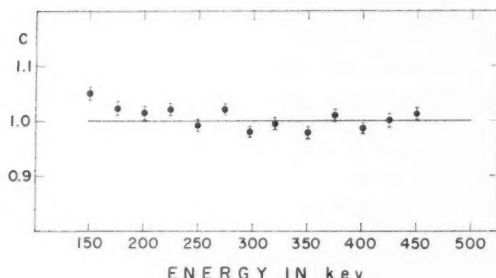


FIG. 4. Electron distribution from the dominant $\Delta J = 2$ parity change transition of Cs^{137} plotted as the ratio of the observed counts per unit momentum interval to $a_1 F p^2 q^2$.

region 4% to 10%. Below 200 kev the points rise because of finite source thickness and in the neighborhood of the end point they rise because of errors in the correction for the poor resolution of the instrument and the imperfections in the calibration. These checks indicated that the spectrometer was adequately linear at the time the checks were made; to allow for possible variations between calibrations, allowance was made in the final error to cover non-linearities and calibration errors which might have occurred during the long periods in which the instrument was in use.

The use of two entrance apertures to the spectrometer defined the region of the neutron beam from which decay events could be detected. This was investigated experimentally by mounting a small source on a device which would allow its location relative to the intercept of the spectrometer axis and the neutron beam axis to be varied. In this way the response of the spectrometer could be investigated as a function of the location of the source. It was found that the effective neutron source was limited in length to approximately three centimeters, and in other directions by the size of the neutron beam. The form of the limitation in length is shown in Figs. 13 and 14; a further discussion of these source dimensions will be found in Sections 4 and 5 of this paper.

The current for the spectrometer coils was electronically stabilized by comparing against standard cells the potential developed by the current passing through a cooled constantan resistor. The comparison was made by a 400-c.p.s. chopper whose output after amplification controlled the generator supplying the current to the coils. The short term and long term stability achieved by this technique was better than 0.1%. The pressure in the vacuum tank was maintained at less than 2×10^{-6} mm of mercury throughout all runs by means of an oil diffusion pump equipped with a water-cooled baffle followed by a Freon-cooled baffle held at -40°C . A liquid-nitrogen trap was also employed and maintained full of liquid nitrogen for the duration of the experiment. It was found necessary to defrost and clean the Freon baffle and the liquid-nitrogen trap about once a month. Apart from this no trouble was experienced in maintaining the required vacuum over the extended duration of the experiment.

2(d). THE PROTON COLLECTION SYSTEM

The proton collection system was designed to accept all the protons from the source volume that recoiled in directions enabling them to escape from the field-free region established by the center electrode assembly. The escape direction was defined by a gridded circular aperture on the axis of the spectrometer but on the side of the assembly furthest away from the spectrometer so that the escaping protons had angles near 180° from the beta-spectrometer axis. The system was designed to accept all protons from zero recoil energy up to the maximum possible recoil energy (755 electron volts) and was designed to keep the proton counter as far from the beam as possible. With the geometric arrangements used the protons in this experiment ranged in recoil energy from 100 ev to 700 ev with most of them in the range 400 ev to 650 ev. The system can be seen in Fig. 2 and will now be described.

Those protons which are produced in the source volume with a direction of recoil which enables them to emerge through the gridded aperture are accelerated through 1 kv across the gap between the central electrode and the gridded end of the first circular tube held at +6 kv. They are then focused by the symmetrical two-tube lens, formed by the gap between the two circular tubes, through the entrance aperture of the proton counter.

The trajectories of the protons through the first gap can be accurately calculated since it is in essence a parallel plate condenser. With a voltage difference of 1 kv across it, all protons up to the maximum possible recoil energy from any point in the source volume can reach the second gap without striking the walls of the first tube. A higher voltage across this gap would of course have had advantages as far as the further focusing of the protons is concerned but would have led to an undesirable perturbation of the field inside the central electrode, and might have caused the acceptance of protons of the wrong recoil direction.

The trajectories through the second gap and on to the proton counter were calculated using the data for symmetrical two-tube lenses given by Klemperer (1953). The calculations were made for various proton recoil energies and

directions and allowance was made for spherical aberration. Spherical aberration is of considerable help in this application since it reduces the focal length of the lens for trajectories which depart considerably from the central axis. This tends to compensate for the increase in focal length which would otherwise occur owing to the higher proton recoil energy causing the departure of the trajectories from the central axis. The calculations indicated that with 6 kv across the lens, all protons which reach the second gap and whose initial recoil energy lies between zero and the maximum recoil energy of 755 volts, should pass through the entrance aperture of the proton counter. Thus with 1 kv across the first gap and 6 kv across the second gap, the electrostatic system does not limit the source volume and can accept all protons for which the beta spectrometer can accept the corresponding electron. The calculations also indicated that because of the large entrance aperture of the proton counter the system should not be at all critical as to the voltage across the second gap.

In order to test this system, coincidence runs were made with the voltage across the first gap fixed at 1 kv and with various voltages across the second gap. The runs were made with the beta spectrometer set at 400 kev. At this electron energy the proton recoils should have the widest spread in energy and should thus provide the best test of the system. The results of these runs are shown in Fig. 5, from which it can be seen that the coincidence rate was essentially independent of the voltage across the second gap between

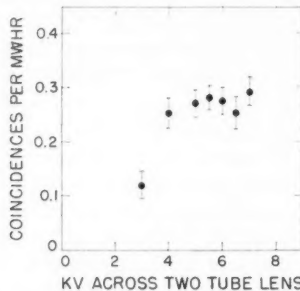


FIG. 5. Coincidence rate between the proton and electron counter plotted against the voltage across the electrostatic focusing lens in the proton collection system.

limits of 4 kv and 7 kv. Below 4 kv the rate dropped, presumably because the higher energy proton recoils were beginning to miss the entrance aperture of the counter because of insufficient bending at the second gap. Above 7 kv trouble with breakdown occurred owing to the high radiation field. The constancy between 4 kv and 7 kv gives evidence that the system was performing as predicted and was accepting all the protons for which the beta spectrometer could accept the corresponding electron.

The proton detector was a laboratory-constructed 14-stage electron multiplier using electrodes fabricated from commercial annealed beryllium copper.

The arrangement of the electrodes is shown in Fig. 6 and was arrived at by trial and error using the steel ball and rubber membrane method of obtaining the trajectories of the electrons between the stages. The arrangement is

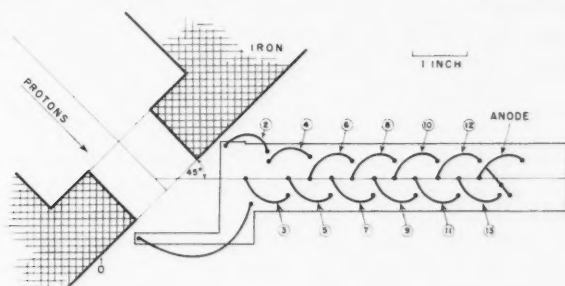


FIG. 6. The electron multiplier used as a proton counter.

similar to that described by Snell and Miller (1948) and the over-all behavior of the multiplier was similar to the behavior described by these workers. The multiplier was activated by induction heating the entire assembly to about 510° C at a pressure of 200 microns of normal untreated tank oxygen. The resulting stage gain of the multiplier was about 3.3 per stage when operated at 400 volts per stage and was very stable with time except during the first few hours after the voltage was applied. It could be made relatively gamma insensitive by keeping the potential of the first electrode at ground potential so that the secondary electrons from the iron shield were not attracted onto the first surface. The gamma sensitivity could, however, be greatly increased by raising the potential of the first electrode to about 200 volts above the grounded iron shield so that the secondaries from the shield were attracted onto this first electrode. Magnetic shielding of the electron multiplier was provided in the form of a mild steel housing with an additional soft iron shield near the first electrode. This shielding was sufficient to make the gain of the multiplier independent of the current through the beta spectrometer coils.

2(e). ELECTRONICS

The electronics were of conventional vacuum tube design and are shown in block form in Figs. 7 and 8. For all of the runs of series I and for the first set of runs of series II, hereafter referred to as series IIa, the arrangement shown in Fig. 7 was used. With this arrangement the coincidences between the protons and electrons were obtained with the aid of a time sorter so that their distribution in time could be examined. For this arrangement the proton side consisted of a wide-band linear amplifier, fast discriminator, and pulse shaper producing a pulse of 0.1-microseconds duration which was fed to all the coincidence units. The electron side consisted of the single channel pulse height analyzer and a pulse shaper producing a pulse of 0.20 micro-

seconds which was fed through delay cables to the coincidence units. A minimum of five and a maximum of eleven identical coincidence units were used with a delay on the electron pulse input of 0.18 microseconds between each unit. For most of the runs six units were used which formed a time sorter covering the range 0.50 microseconds to about 1.70 microseconds. These

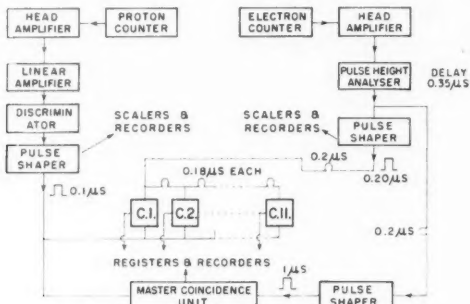


FIG. 7

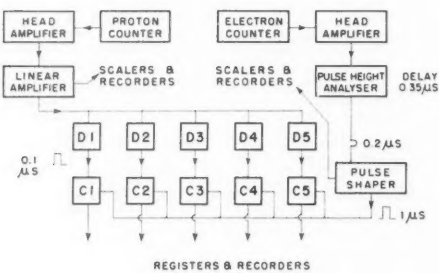


FIG. 8

FIG. 7. Block diagram of the electronics used to record the coincidences in series I and IIa.
FIG. 8. Block diagram of the electronics used to record the coincidences in series IIb.

delays are such that the pulse from the proton counter must be later than the pulse from the electron counter by an amount in the above-mentioned range in order to record a coincidence. Thus the first unit of the time sorter recorded events in which the proton pulse was between 0.50 and 0.80 microseconds later than the corresponding electron pulse. In parallel with this time sorter a single master coincidence unit recorded all events where the proton pulse was between 0.50 microseconds and 1.70 microseconds later than the electron pulse.

A further set of runs was taken with a different arrangement of the electronics in which the time sorter was not used but five separate discriminators and coincidence units recorded the coincidences at different proton discriminator biases. For this set of runs, referred to hereafter as series IIb, the geometrical

arrangement of the apparatus was identical with that used in series IIa. The electronic arrangement is shown in Fig. 8, which, with the discussion of Fig. 7 in mind, is self-explanatory.

Considerable effort was devoted to making the circuits as stable and reliable as possible; in particular the high voltages supplied for the counters were obtained from chopper type stabilizing units using standard cells as reference potentials.

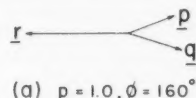
2(f). NEUTRON BEAM MONITORING

Three beam monitors were used, all recording independently. These were: (a) a plutonium-fission ionization chamber mounted in the beam catcher, (b) a halogen-filled Geiger counter wrapped in cadmium with a high stability feedback d-c. amplifier monitoring the current from its collector wire, and (c) a halogen-filled Geiger counter with standard pulse counting circuits. The halogen-filled counters were located close to the beam in the shielding. Monitors (a) and (b) were used in the actual analysis of the runs with (c) being used as a remote indicating device and reserve monitor. The measurement of the d-c. current from monitor (b) proved to be a remarkably reliable method of monitoring the beam intensity.

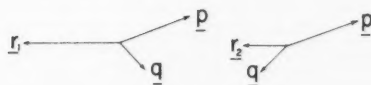
3. EXPERIMENTAL PROCEDURE

3(a). RANGE OF ELECTRON MOMENTA INVESTIGATED

Before discussing the experimental procedure a discussion will be given of the range of electron momenta over which data can usefully be taken. A study of Fig. 9 will show that if the electron-proton angle is fixed and if the electron momentum p is less than the neutrino momentum q , there is only one proton recoil momentum r which will satisfy the conservation of linear momentum, whereas if p exceeds q there are two possible proton recoil momenta which will conserve momentum. These two will be referred to as the high momentum recoils and the low momentum recoils. For the neutron decay $p = q$ for $p = 1.07$, equivalent to an electron kinetic energy of 237 kev. For a given



(a) $p = 1.0, \phi = 160^\circ$



(b) $p = 1.5, \phi = 160^\circ$

FIG. 9. The conservation of linear momentum between the electron p , the neutrino q , and the recoil r with a fixed angle of 160 degrees between p and r . The top figure indicates the situation where p is less than q resulting in only one possible value of r ; the lower figure shows the two possible values of r which can occur if p is larger than q .

electron momentum p it is possible to calculate the corresponding ranges of proton recoil momenta for the geometric arrangements used. These can then be combined with the limits of the distance which the protons travel in the field-free region to obtain the spread in the transit times of the protons in the field-free region. The proton transit times in the rest of the proton system can then be added to obtain the total transit time limits for the proton from the decay events to their arrival at the electron multiplier. Representative values of these total transit times are listed in Table III.

TABLE III

TRANSIT TIMES IN MICROSECONDS OF THE PROTONS CORRESPONDING TO VARIOUS ELECTRON MOMENTA, p . HIGH AND LOW REFER TO THE HIGH MOMENTUM RECOIL GROUP AND THE LOW MOMENTUM RECOIL GROUP

p	Series I		Series II	
	High	Low	High	Low
1.0	0.74→0.93	—	0.74→0.90	—
1.1	0.74→0.93	5.63→10.65	0.74→0.90	6.25→10.65
1.2	0.74→0.98	1.84→3.19	0.74→0.90	2.05→3.19
1.3	0.74→0.98	1.27→2.48	0.74→0.92	1.41→2.08
1.4	0.73→1.07	0.98→1.79	0.73→0.95	1.13→1.79
1.5	0.73→1.10	0.91→1.39	0.73→0.96	0.98→1.39
1.6	0.73→1.06	0.89→1.25	0.73→1.02	0.86→1.25
1.7	0.73→1.03	0.87→1.13	0.73→0.99	0.83→1.13
2.0	0.73→0.95	0.81→0.95	0.73→0.92	0.79→0.95

It can be seen from Table III that the spread in proton transit times is less than one microsecond for p below 1.07 and above about 1.42. In the region between 1.07 and 1.4, however, the spread for the low momenta recoil group is quite large. In the actual experiment it was impractical to record data where the spread in transit times exceeded one microsecond since the required long resolving time of the coincidence unit would have allowed too many random coincidences to be recorded. However, in the range $p = 1.07$ to 1.23 it was calculated that the fraction of the low momenta group was less than three per cent of the high momenta group; consequently some data were taken in this range and corrected for the loss of the low momenta group. This correction was considerably less than the statistical error of the data.

The situation can be summarized as follows:

- (i) Below $p = 1.0$ the number of events is too few to warrant the time necessary to accumulate statistically useful data. No data were taken in this range of electron momenta.
- (ii) From $p = 1.0$ to 1.07; only high momenta recoils occur and the resulting spread in transit times is less than 0.5 microseconds. Data were taken in this range.
- (iii) From $p = 1.07$ to 1.23; the number of low momenta recoils is less than three per cent of the number of high momenta recoils. Data were taken in this range and corrected for the loss of low momenta recoils.

- (iv) From $p = 1.23$ to 1.45 ; the spread in transit times of the low momenta recoils is large and their numbers are relatively large. Data taken in this range were not used in the analysis of the results.
- (v) Above $p = 1.45$; the spread in transit times of the low momenta group is less than 0.5 microseconds and overlaps that of the high momenta group. Data were taken in this range.

3(b). METHOD OF TAKING THE DATA

Data were taken by counting the coincidences between the scintillation counter and the electron multiplier at various settings of the current through the beta spectrometer coils. At each current setting data were taken at five different bias settings of the discriminator in the electron multiplier channel. In series I and IIa this involved taking five separate runs whereas in series IIb the data for the five bias conditions were obtained simultaneously. For each run in series I and IIa both the time sorter data and the over-all coincidence data were recorded whereas in series IIb only the over-all coincidence data were available. Random coincidences were calculated from the individual counter rates and the resolving times of the coincidence circuits, and were subtracted from the total coincidences to give the genuine coincidences resulting from the neutron decay events. The resolving times were measured before and after each run by measuring random coincidences with the aid of radioactive sources. The electron multiplier was made more sensitive to gamma rays for these random coincidence measurements in the manner described in Section 2(d).

A typical time sorter curve is shown in Fig. 10 for a $p = 1.46$ run of series I. Random coincidences have been subtracted and amounted to about 100 coincidences for each time sorter channel. In this figure the proton transit time is shown as the center of the individual channels so that each point represents coincidences between about -0.14 microseconds and +0.14 microseconds from the plotted abscissa.

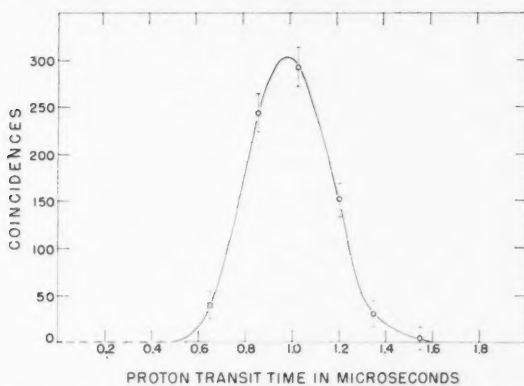


FIG. 10. Time sorter results for a series I run taken at $p = 1.46$.

To prove that the coincidences were due to neutron decay events, runs were made with (a) a boron shutter located at S of Fig. 2, which eliminated the thermal neutrons from the beam, and (b) with no voltage on the center electrode assembly so that protons could not reach the electron multiplier. These checks, in conjunction with the fact that the coincidences occurred at the correct delay for neutron decay events, indicated that the coincidences were in fact due to neutron decay events.

The total number of coincidences could be obtained for an individual run of series I or series IIa by two methods: (a) by dividing the area under the time sorter curve of genuine coincidences by the average resolving time of the time sorter channels and (b) by using the number of genuine coincidences recorded by the over-all coincidence unit. These two methods agreed well as to the total number of coincidences. In the case of series IIb only the latter method was available. From the individual runs of a set taken at a fixed spectrometer current an integral bias curve was plotted against the electron multiplier discriminator bias. On the basis of a large number of such bias curves it appeared that over the range of bias settings used, the integral bias curves were well fitted by an exponential. A best estimate for the number of coincidences at a particular spectrometer setting was therefore obtained by least square fitting the data of the individual runs to an exponential bias curve and using the intercept at zero bias. The purpose of using this method of taking electron multiplier bias curves at each setting was to overcome any possible long term drifts in the gain of the electron multiplier; during the experiment, however, the slopes of the exponentials remained constant within statistical errors indicating the high stability of the electron multiplier when operated continuously in a good vacuum. Figure 11 shows one set of runs plotted as an integral bias curve together with the corresponding least squares exponential. The normalizing of the individual runs was made on the basis of the neutron monitor readings with an arbitrary unit of megawatts as a convenient measure of the beam strength. The megawatt unit was established on a certain date to correspond to a reactor thermal megawatt

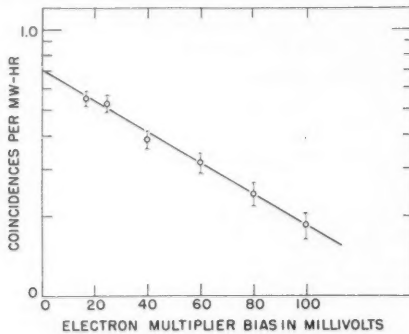


FIG. 11. Coincidence results for a set of series I runs shown as an integral electron multiplier bias curve. The abscissa refer to the pulse size at the last electrode of the electron multiplier.

but owing to load changes in the reactor our megawatt unit differed on occasion from the reactor thermal megawatt by up to 20 per cent. In general each run lasted for about 800 megawatt hours.

4. THEORETICAL SPECTRUM SHAPES

In order to obtain the theoretical spectrum shape it was necessary to estimate the efficiency $g(\varphi)$ with which the apparatus could detect events which have an angle φ between the direction of the proton and the electron. The significance of $g(\varphi)$ was discussed in Section 1. It was estimated by performing Monte Carlo type calculations with the aid of the FERUT computer of the University of Toronto. The author is deeply indebted to Dr. J. M. Kennedy of the Theoretical Physics Branch of Atomic Energy of Canada Limited for arranging and co-ordinating these Monte Carlo calculations and the subsequent numerical integrations which led to the theoretical spectrum shapes.

In essence the Monte Carlo calculations were performed by selecting at random a point in the effective source volume and then selecting a proton recoil direction at random. If the resulting trajectory of the proton was such that it would be detected by the proton system this event was investigated further and a corresponding electron direction was chosen at a fixed angle φ from the proton direction but with the plane of the angle φ again randomly chosen. The trajectory of this electron was then investigated to see whether it would enter the second entrance aperture of the beta spectrometer and be detected. If it could be detected this event was recorded as an event, with a certain value of φ which could be detected by the system. By repeating this sequence a large number of times and for different chosen values of the electron proton angle φ it was possible to obtain the shape of the variation of $g(\varphi)$ with φ .

The input data required for the Monte Carlo calculations was the effective source volume. As discussed in Section 2(a) the effective source volume was defined by the neutron intensity across the beam diameter in a plane perpendicular to the neutron beam and by the acceptance of the beta spectrometer in the direction of the beam. The neutron density across the beam was measured by the induced activity in copper wires and is shown for a horizontal diameter in Fig. 12. The vertical diameter distribution was almost identical. Also shown in this figure are two alternative weighting functions used to weight the random selection of decay event location in different Monte Carlo runs. The measurement of the length distribution has been discussed in Section 2(c); the results for series I are shown in Fig. 13 together with four alternative weighting functions used in the Monte Carlo runs. The corresponding results for series II are shown in Fig. 14. Several sets of Monte Carlo runs were made corresponding to different choices of the weighting functions for the source dimensions. These are listed in Table IV.

The results of the Monte Carlo calculation of $g(\varphi)$ for set II are shown for both series I and series II in Fig. 15. These curves therefore indicate the efficiency of the apparatus for detecting events where the angle between the

TABLE IV

NOTATIONS TO INDICATE THE DIFFERENT MONTE CARLO RUNS CORRESPONDING TO DIFFERENT ASSUMPTIONS AS TO THE SOURCE DIMENSIONS

Monte Carlo set	Radial distribution	Length distribution
I	R	A
II	R	B
III	S	A
IV	R	C
V	R	D

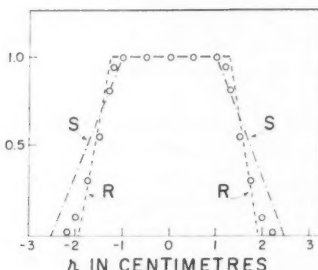


FIG. 12. The points represent the measured neutron density across the neutron beam at the center of the sensitive volume. The lines represent alternative approximations used in the Monte Carlo runs. For a fuller explanation see text.

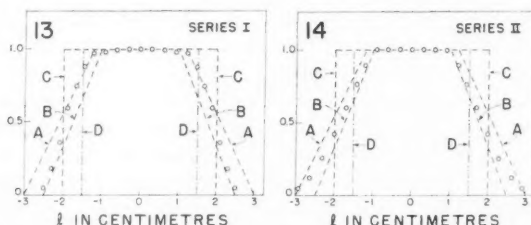


FIG. 13. The points represent the measured longitudinal distribution along the sensitive volume for series I. The lines represent alternative approximations used in the Monte Carlo runs. For a fuller explanation see text.

FIG. 14. The points represent the measured longitudinal distribution along the sensitive volume for series II. The lines represent alternative approximations used in the Monte Carlo runs. For a fuller explanation see text.

electron and proton is φ with the source dimension assumptions listed in Table IV. The results for the other Monte Carlo sets were quite similar for φ less than 170° but differed slightly in the region of φ from 170° to 180° .

From the Monte Carlo results for $g(\varphi)$ the corresponding functions F_0 and F_1 were computed by desk calculator or with the aid of an IBM 602A; these computations were made by the computing staff of the Theoretical Physics Branch of Atomic Energy of Canada Limited under the direction of Dr. J. M.

Kennedy. Figure 16 shows the functions F_0 and F_1 plotted against electron momentum for series I Monte Carlo set II together with a plot of the Fermi

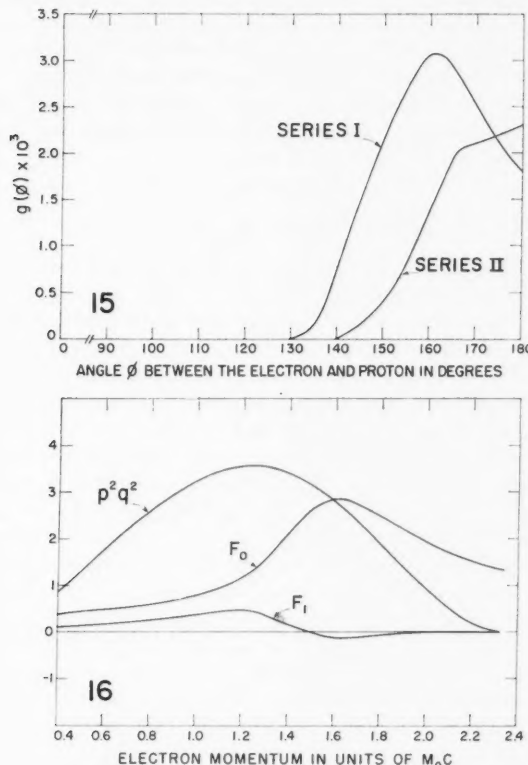


FIG. 15. The efficiency $g(\varphi)$ of the apparatus for detecting an event occurring anywhere in the source volume with an angle φ between the direction of the electron and the recoil proton.

FIG. 16. The functions F_0 and F_1 obtained from the Monte Carlo runs for series I under the assumptions as to the source volume listed as set II. Also shown is the Fermi distribution $p^2(E_0 - E)^2$ for the neutron decay spectrum.

distribution $p^2(E_0 - E)^2$ for the neutron beta spectrum. The final theoretical spectrum shapes were obtained by forming the products

$$x_0 = p^2(E_0 - E)^2 F_0,$$

$$x_1 = p^2(E_0 - E)^2 F_1,$$

and correcting the resultant functions x_0 and x_1 for the resolution of the beta spectrometer to obtain the number of electrons per unit momentum interval

$$n(p) = x_0'(p) + \alpha x_1'(p),$$

where $x_0'(p)$ and $x_1'(p)$ are the resolution corrected functions $x_0(p)$ and $x_1(p)$ and α is the electron neutrino angular correlation coefficient. The resolution corrections were in general less than two per cent and since the correction was being made to a theoretical curve for perfect resolution rather than the usual case where they are made to an experimental curve of imperfect resolution, they could be made with considerable confidence. The slowly varying Coulomb correction factor for a beta-minus decay into a nucleus of charge $Z = 1$ was not applied to the theoretical spectrum shapes but was used as a divisor of the observed number of events per unit momentum interval. The effect of the Coulomb correction factor was almost negligible.

5. EXPERIMENTAL RESULTS

The experimental data accumulated by the methods described in Section 3(b) were used to give values for the observed number of coincidences per unit momentum interval at various electron momenta. These values were then compared to the theoretical spectrum shape $x_1'(p) + \alpha x_0'(p)$ to yield the least squares best value for α and its statistical error. Least squares fits were made to all the sets of Monte Carlo runs listed in Table IV with the exception that Monte Carlo set IV was not used for series II data. Set IV was the first set to be tried on the Ferut Computer and the particular values of φ for which it was calculated were not suitable for the geometric conditions of series II though they were well suited to the conditions of series I. The results of the least squares fitting are listed in Table V. It can be seen that the variation in the resulting value of α for the different Monte Carlo sets is considerably less than the error in α owing to the statistics of the counting rates. Since the Monte Carlo sets cover a wide range of assumptions about the dimensions of the effective source it can be concluded that the error introduced by not exactly reproducing the dimensions in the Monte Carlo calculations is not serious.

TABLE V
VALUES OF THE ELECTRON NEUTRINO ANGULAR CORRELATION COEFFICIENT α OBTAINED BY LEAST SQUARES FITTING OF THE EXPERIMENTAL DATA OF SERIES I, II_a, AND II_b TO THE THEORETICAL SPECTRUM SHAPES PREDICTED FROM THE MONTE CARLO SETS I TO V

Monte Carlo set	Series I	Series II _a	Series II _b
I	+ .07	- .04	+ .03
II	+ .10	+ .05	+ .11
III	+ .08	0	+ .06
IV	+ .06	+ .01	+ .09
V	+ .06		
Statistical error in α for all sets	$\pm .11$	$\pm .17$	$\pm .14$

The experimental data for series I and series II_b are plotted in Figs. 17 and 18 together with the least squares best fits for the pure interactions. Monte Carlo set I was used in these figures. Figure 19 shows both series I

and series IIa data on the same plot to show the relative shapes of the spectra for the two geometric conditions used in the two series. The shift of the peak of the spectrum of series IIa corresponds to the smaller mean value of the electron proton angle.

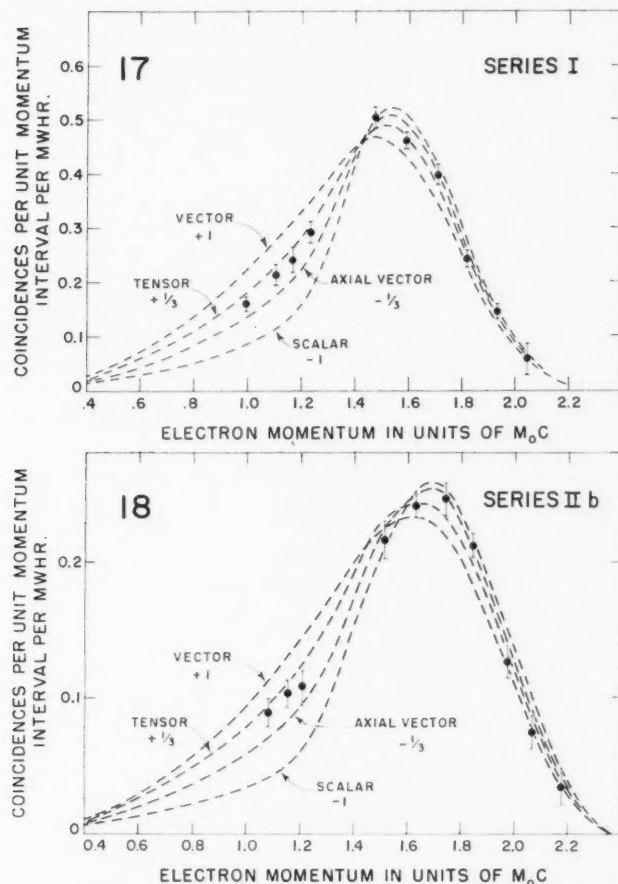


FIG. 17. The experimental data of series I shown with the least squares best fits for the pure interactions.

FIG. 18. The experimental data of series IIb shown with the least squares best fits for the pure interactions.

The adopted values for α from these three series of runs were $\alpha = +.08$ for series I, $\alpha = +.01$ for series IIa, and $\alpha = +.07$ for series IIb. The errors in these values of α will now be discussed.

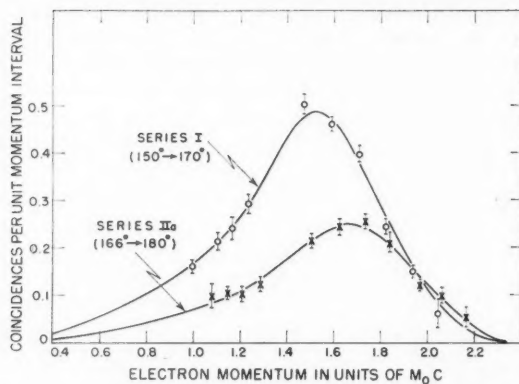


FIG. 19. The spectrum shapes of series I and series IIa shown on the same scale to show the differences resulting from the geometric conditions of the two series.

(a) Statistical errors. These were computed during the least squares fitting of the data to the theoretical curves using the statistical errors of the coincidence counts. Expressed as standard deviations they amount to $\pm .11$ for series I; $\pm .17$ for series IIa, and $\pm .14$ for series IIb. The standard deviation in the weighted mean of series IIa and IIb is $\pm .11$.

(b) Error due to the imperfect representation of the actual source dimensions in the Monte Carlo calculations. These were estimated as $\pm .03$ for series I and $\pm .04$ for the series II runs from the variation of a for the different assumptions used in the different Monte Carlo sets and listed in Table V.

(c) Error due to possible beta spectrometer calibration errors. Errors in the beta-spectrometer calibration directly affect the resulting computed value of a since they imply that the experimental points were fitted to the theoretical spectrum shapes at consistently incorrect momenta. An estimate of this error was made by repeating least squares fits for various displacements of the calibration. It was found that for a calibration error of 1% the resultant error in a was 0.11 for series I and 0.13 for series IIa and IIb. The spectrometer resolution was 7.7% for series I and 8.5% for series IIa and IIb expressed as full width at half maximum. Allowance was made for a possible calibration error of 1/10th the resolution width leading to possible errors of $\pm .09$ in series I and $\pm .11$ in series IIa and IIb. This is the most serious of the known systematic errors.

(d) Error due to possible non-linearity of the spectrometer between calibration points. This was estimated by making least squares fits for a possible non-linearity of 1/10th the resolution width over the range of interest. It is a less serious error than a consistent calibration error because it does not affect all of the experimental points to the same degree. It amounted to $\pm .03$ for series I and $\pm .04$ for series IIa and IIb.

(e) Error due to the window settings in the pulse height selection of the beta-counter output. This error was minimized by making several independent

runs at each spectrometer setting. It was estimated by allowing that in an individual run an error of $\pm 5\%$ could have occurred in the counting rate owing to errors in the window setting. This would lead to an error in the values of a of about $\pm .02$ if all these errors were independent. This error was somewhat arbitrarily doubled to allow for a possible dependence in the error on the spectrometer setting.

(f) Error due to the Monte Carlo statistics. About 1000 successful Monte Carlo events were used to derive the theoretical spectrum shapes for each Monte Carlo set. With four independent Monte Carlo sets this introduces a standard deviation in the resulting value of a for each series of about $\pm .05$.

In combining these errors it was assumed that series IIa and series IIb were taken under identical conditions. They were therefore combined to form an over-all result for series II of $+ .05$ with a standard deviation of $\pm .11$. This was then combined with the other errors listed above to provide a final result for series II. In this combination it was assumed that the errors listed as (b) to (f) above were independent and should therefore be combined in quadrature. Series I with its different geometrical arrangement was considered independently from series II. The final results for series I and II were then combined to yield a best value for the electron neutrino angular correlation coefficient in the beta decay of the free neutron of $a = + .07 \pm .12$. Table VI tabulates the errors and their combination into the final result.

TABLE VI
SUMMARY OF KNOWN ERRORS

Type of error	Series I	Series II (IIa and IIb combined)
Counting statistics	$\pm .11$	$\pm .11$
Source volume errors	$\pm .03$	$\pm .04$
Spectrometer calibration errors	$\pm .09$	$\pm .11$
Non-linearity errors	$\pm .03$	$\pm .04$
Window errors	$\pm .04$	$\pm .04$
Monte Carlo statistics	$\pm .05$	$\pm .05$
Over-all error	$\pm .16$	$\pm .18$

6. DISCUSSION

The result quoted for the angular correlation coefficient has assumed that the Fierz interference terms between the scalar and vector interactions in the Fermi part of the decay and between the tensor and axial vector interactions in the Gamow-Teller part of the decay are zero. From the evidence in the case of the Gamow-Teller part of the decay (Sherr and Miller 1954) it appears that the Fierz term, b_{GT} , is less than .06; in the case of the Fermi part the limit has not been so well established but from the deduction of Michel based on a revision of an analysis originally made by Gerhart and Sherr on the $f\ell$ values of $0 \rightarrow 0$ transitions (Michel 1957) it appears that b_F is less than .30. From a study of the spectrum of N^{13} Daniel and Schmidt-Rohr (1958) have concluded that b_F is less than .11. A large value of these interference terms

would have an effect on the interpretation of the experimental data since it would change the shape of the theoretical spectrum shapes deduced from the Monte Carlo results. With a limit of 0.3 for the Fermi, and .06 for the Gamow-Teller part of the Fierz term b , however, the effect would amount to a change in a of less than .04. It has therefore been neglected in the analysis of this experiment.

The ratio of the Gamow-Teller coupling constant to the Fermi coupling constant is generally considered to be $C_{GT}/C_F = 1.14 \pm .05$ (Michel 1957; Kofoed-Hansen and Winther 1956). Using this value the expected values of the electron neutrino angular correlation coefficients are listed in Table VII for four assumptions as to the form of the beta-decay interaction. It can be seen that the experimental result is consistent with a beta-decay interaction of the form ST or AV but is not consistent with an interaction of the form SA or VT.

TABLE VII
EXPECTED VALUE OF a FOR VARIOUS COMBINATIONS OF INTERACTIONS

Form of interaction	Angular correlation coefficient
S, T	$+ .06 \pm .02$
A, V	$- .06 \pm .02$
V, T	$+ .47 \pm .01$
S, A	$- .47 \pm .01$
This experiment	$+ .07 \pm .12$

ACKNOWLEDGMENTS

The author would like to express his appreciation for the help received from Dr. J. M. Kennedy in arranging the Monte Carlo computations and the associated calculations leading to the theoretical spectrum shapes. He would also like to thank Mr. G. C. Dixon for help in constructing, testing, and using the experimental apparatus.

APPENDIX

The formulae for the terms used in the expressions describing the momentum distribution of the electrons in coincidence with the protons are given below.

$$f_0^\pm(\varphi) = \frac{1 + \lambda^2 \cos 2\varphi}{\sqrt{1 - \lambda^2 \sin^2 \varphi}} \mp 2\lambda \cos \varphi,$$

$$f_1^\pm(\varphi) = \left\{ -\lambda \sin^2 \varphi \mp \cos \varphi \sqrt{1 - \lambda^2 \sin^2 \varphi} \right\} f_0^\pm(\varphi),$$

$$\lambda = p/q = \text{ratio of electron momentum to neutrino momentum.}$$

The two signs arise from the possibility that if the electron momentum p exceeds the neutrino momentum q there are two different proton momenta which will satisfy momentum conservation with an electron at a fixed angle

from the proton (see Fig. 9). These two cases are referred to in the text as the high momentum recoils and the low momentum recoils.

For both recoils considered together

$$f_0(\varphi) = f_0^+(\varphi) \quad \text{and} \quad f_1(\varphi) = f_1^+(\varphi) \quad \text{for } \lambda \leq 1,$$

$$f_0(\varphi) = f_0^+(\varphi) + f_0^-(\varphi) \quad \text{and} \quad f_1(\varphi) = f_1^+(\varphi) + f_1^-(\varphi) \quad \text{for } \lambda > 1,$$

$$F_0(p) = \frac{1}{2} \int_0^\pi f_0(\varphi) g(\varphi) \sin \varphi d\varphi,$$

$$F_1(p) = \frac{1}{2} \beta \int_0^\pi f_1(\varphi) g(\varphi) \sin \varphi d\varphi.$$

REFERENCES

- ALFORD, W. P. and HAMILTON, D. R. 1957. Phys. Rev. **105**, 673.
 DANIEL, H. and SCHMIDT-ROHR, U. 1958. Nuclear Phys. **7**, 516.
 GOOD, M. L. and LAUER, E. J. 1957. Phys. Rev. **105**, 213.
 HERRMANNSFELDT, W. B., MAXSON, D. R., STÄHELIN, P., and ALLEN, J. S. 1957. Phys. Rev. **107**, 641.
 JACKSON, J. D., TREIMAN, S. B., and WYLD, H. W. 1957. Phys. Rev. **106**, 517.
 KLEMPERER, O. 1953. Electron optics, 2nd ed. (Cambridge University Press).
 KOFOED-HANSEN, O. and WINther, A. 1956. Kgl. Danske Videnskab. Selskab., Mat.-fys. Medd. **30**, No. 20.
 MAXSON, D. R., ALLEN, J. S., and JENTSCHKE, W. K. 1955. Phys. Rev. **97**, 109.
 MICHEL, L. 1957. Revs. Mod. Phys. **29**, 223.
 ROBSON, J. M. 1955. Phys. Rev. **100**, 933.
 ROSE, M. E., PERRY, C. L., and DISMUKE, N. M. 1953. Oak Ridge National Laboratory ORNL-1459.
 RUSTAD, B. M. and RUBY, S. L. 1955. Phys. Rev. **97**, 991.
 SHERR, R. and MILLER, R. H. 1954. Phys. Rev. **93**, 1076.
 SNELL, A. H. and MILLER, L. C. 1948. Atomic Energy Commission Document AECD-1956.

ASYMMETRY OF THE CONCENTRATION FRONT DURING MISCIBLE DISPLACEMENT IN POROUS MEDIA¹

A. E. SCHEIDECKER AND V. C. LARSON

ABSTRACT

During many feasible experiments concerning miscible displacement in porous media, it has been noted that the concentration front is slightly asymmetric. It is possible that this is due to an asymmetry in the boundary conditions which is present in most practicable displacement experiments. The present paper endeavors to investigate the influence of asymmetric boundary conditions upon the shape of the concentration front: The diffusivity equation basic to the theory of miscible displacement has been solved for the case of injection of fluid of constant concentration at one end of a long, linear porous medium. The solution has been effected by an electrical analogue computer. Curves showing the asymmetry are given.

1. INTRODUCTION

The statistical approach to the study of flow through porous media has shown itself as especially satisfactory in the discussion of miscible displacement processes which are important in studies of groundwater flow and of new methods of oil recovery. It appears that the experimental evidence as reported in the literature is in general agreement with the predictions to which the consideration of statistical models leads.

The usual solutions of the differential flow equations (cf. Scheidegger 1957, 1958) have one very important characteristic feature: They are all symmetrical about the mean concentration of the fluid under consideration. In the case of a linear displacement experiment, this means that the shape of the invading concentration front is exactly symmetrical about the half-concentration point. Most published data seem to be in reasonable agreement with this pattern, but there appear to be cases where the displacement front is skewed.

One possible cause for the development of a skewed displacement front may be that the boundary conditions during an injection test are not really those that are usually postulated in order to arrive at the symmetric shape for the front: The latter would occur only in the case of a linear porous medium that extends to infinity in the positive as well as in the negative direction. In practice, however, a porous medium cannot be made infinitely long. One will, in general, inject fluid of a certain kind at one end at $x = 0$ and observe its intrusion into a linear porous medium. It is to be expected that the shape of the front will be asymmetrical in such an experiment, simply because the boundary conditions are asymmetrical.

It is the purpose of the present paper to investigate the effect of the asymmetry of the boundary condition upon the shape of the displacement front. Only the ordinary statistical theory without autocorrelation will be considered. The basic diffusivity equation has been solved for the prevailing

¹Manuscript received August 4, 1958.

Contribution from the Imperial Oil Research Laboratory, Calgary, Alta.

boundary condition by an electrical analogue machine. It will be shown that, for most common porous media, the asymmetry of the concentration front due to the asymmetry of the boundary condition is quite negligible under ordinary conditions. The conditions under which the asymmetry *does* become important are established and curves which must be referred to under these circumstances are provided.

2. FORMULATION OF THE PROBLEM

The differential equation for miscible displacement (without autocorrelation) in a linear porous medium is

$$(2.1) \quad \frac{\partial \psi}{\partial t} = D \frac{\partial^2 \psi}{\partial x'^2}$$

where ψ is the concentration of the invading fluid, D is a factor of dispersion, and x' is a length measured from the mean position of the injection front; i.e.

$$(2.2) \quad x' = x - vt$$

where v is the pore velocity of injection and x is the true (length) co-ordinate of the point under consideration.

It is proposed to solve eq. (2.1) for the case where at $x = 0$, fluid of constant concentration

$$(2.3) \quad \psi(x = 0, t) = \text{const.}$$

is injected at one end ($x = 0$) into the linear porous medium. In the primed co-ordinate system, the boundary condition (2.3) becomes

$$(2.4) \quad \psi(x' = -vt) = \text{const.}$$

This problem, in fact, can be solved analytically by introducing higher transcendental functions (Aronofsky 1957). However, the availability of an electric analogue computer at the Imperial Oil Research Laboratory makes it profitable to obtain the solution by that means, especially since the analytical solution still requires a fair amount of computation to obtain actually a displacement curve.

3. THE ELECTRICAL ANALOGUE

The differential equation for miscible displacement in a porous medium as shown in (2.1) is a diffusivity equation. It is well known that the solution of the diffusivity equation can be simulated by an electrical network containing resistors and condensers. In order to establish the relationships between the required solution of the diffusivity equation (2.1) and the quantities measured in an electrical network, it is necessary to analyze the latter.

The basic electrical network which is to supply the solution to the problem is shown in Fig. 1. Here V_n denotes the voltage at the n th junction point, C_n is the n th capacitor, and R_n the n th resistor. For our applications, all the capacitors and resistors are assumed to be identical.

The continuity condition for the current (i) at the $(n + 1)$ th junction point yields

$$(3.1) \quad i_{R_n} = i_{C_{n+1}} + i_{R_{n+1}}.$$

The voltage across the n th resistor is given by

$$(3.2) \quad V_{n+1} - V_n = -i_{R_n} R_n.$$

Similarly, the current into the n th capacitor is given by

$$(3.3) \quad i_{C_n} = C_n \dot{V}_n.$$

Eliminating the currents from the above system and setting $C = C_n$, $R = R_n$ (since all capacitors and resistors are equal) yields

$$(3.4) \quad C \dot{V}_n = i_{R_{n-1}} - i_{R_n},$$

$$(3.5) \quad C \dot{V}_n = -\frac{1}{R} [(V_n - V_{n-1}) - (V_{n+1} - V_n)].$$

This can be written, since Δn (the steps of n) are equal to 1

$$(3.6) \quad R C \dot{V}_n = \left. \frac{\Delta V}{\Delta n} \right|_n - \left. \frac{\Delta V}{\Delta n} \right|_{n-1} = \left. \frac{\Delta^2 V}{\Delta n^2} \right|_n$$

and, if the steps be many

$$(3.7) \quad R C \dot{V} \cong \frac{\partial^2 V}{\partial n^2}.$$

This is the diffusivity equation.

In order to compare the diffusivity equation of the electrical analogue with that describing miscible flow through porous media, one has to bring both into a dimensionless form.

(a) Electrical Analogue

Introducing the dimensionless variables

$$(3.8) \quad \tau = t/(RC),$$

$$(3.9) \quad \nu = V/V_0,$$

where V_0 is some constant reference voltage, yields

$$(3.10) \quad \frac{\partial \nu}{\partial \tau} = \frac{\partial^2 \nu}{\partial n^2},$$

which is dimensionless.

(b) Porous Media

Introducing the dimensionless variables

$$(3.11) \quad \tau = t/t_0,$$

$$(3.12) \quad \xi = \frac{x}{\sqrt{Dt_0}},$$

$$(3.13) \quad \phi = \psi/\psi_0$$

yields

$$(3.14) \quad \frac{\partial \phi}{\partial t} = \frac{\partial^2 \phi}{\partial \xi^2},$$

which is again dimensionless.

(c) *Boundary Conditions*

Finally, one has to formulate the equivalent boundary conditions for the two cases.

In the *original*, one has

$$(3.15) \quad \psi = \psi_0 \quad \text{for } x = -vt,$$

which is, in dimensionless variables

$$(3.16) \quad \phi = 1 \quad \text{for } \xi = \frac{-vt}{\sqrt{Dt_0}} = \frac{-vt_0}{\sqrt{Dt_0}} \tau.$$

This signifies for the *analogue*

$$(3.17) \quad \nu = (V/V_0) = 1 \quad \text{for } n = -\alpha t = \alpha RC\tau,$$

where α is the number of steps per unit time (i.e. $1/\alpha$ is the time in which the boundary condition recedes by one step). This leads to the following equivalent

$$(3.18) \quad \alpha RC \sim \frac{vt_0}{\sqrt{Dt_0}}.$$

(d) *Comparison*

One can now compare the dimensionless forms in the two cases (porous media and electrical analogue) and set up a table of equivalents (see Table I) where the time in the original has been denoted by T .

TABLE I

Analogue	Original
n	$x/\sqrt{(Dt_0)}$
t/RC	T/t_0
V/V_0	ψ/ψ_0
αRC	$v\sqrt{(t_0/D)}$

Suppose now that a run has been made in the analogue with the parameters R , C , α (and V_0 , of course) given. It will be shown that this can be made to correspond to any porous flow problem with the values D , v given.

One simply has (from the very last equivalence)

$$(3.19) \quad t_0 = D\alpha^2 R^2 C^2 / v^2;$$

hence for the time ratio (t = analogue, T = original)

$$(3.20) \quad \frac{t}{T} = \frac{RC}{t_0} = \frac{v^2}{D\alpha^2 RC}$$

and for the ratio n/x

$$(3.21) \quad \frac{n}{x} = \frac{v}{D\alpha RC}.$$

4. RESULTS

The network indicated in Fig. 1 was set up on Imperial's analogue machine. A total of 150 capacitor-resistor (RC) units was available, of which half was used to represent the displaced fluid (+ units), the other half the displacing fluid (-units). Accordingly, at time $t = 0$, all the + capacitors were discharged, all the - capacitors were kept at constant voltage. After each time step $\Delta T = 1/\alpha$, one of the - capacitors was disconnected from the battery.

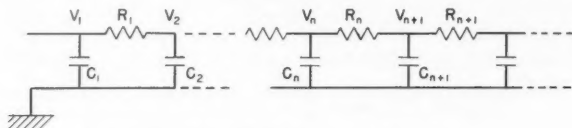


FIG. 1. Network of the analogue machine.

Two series of runs were made. In series I, RC was equal to 4 seconds, $1/\alpha$ was equal to 5 seconds/step. In series II, RC was equal to 0.8 seconds, $1/\alpha = 5$ seconds/step. Since data could be read simultaneously only at four points of the network, several runs had to be made in each series to obtain a complete set of results. The results obtained are shown graphically in Figs. 2-4.

The various figures show the skewedness of the displacement front very well. However, if the electrical analogue is compared with average porous media, it turns out that the skewedness can be significant only at the very beginning of the displacement experiment. Thus, let a typical linear displacement experiment be performed as follows: The pore velocity of injection we assume as

$$(4.1) \quad v = 10^{-2} \text{ cm/sec.}$$

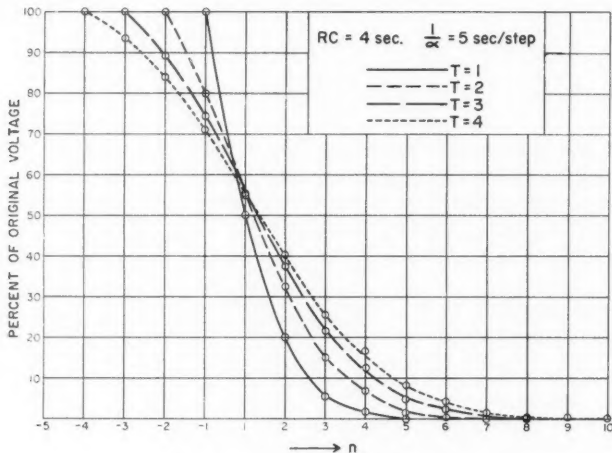


FIG. 2. Data from series I runs for short times.

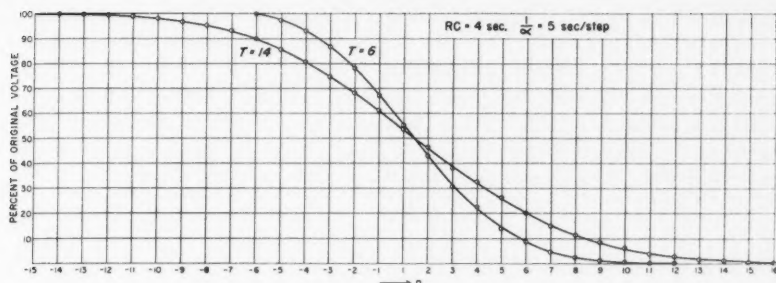


FIG. 3. Data from series I runs for long times.

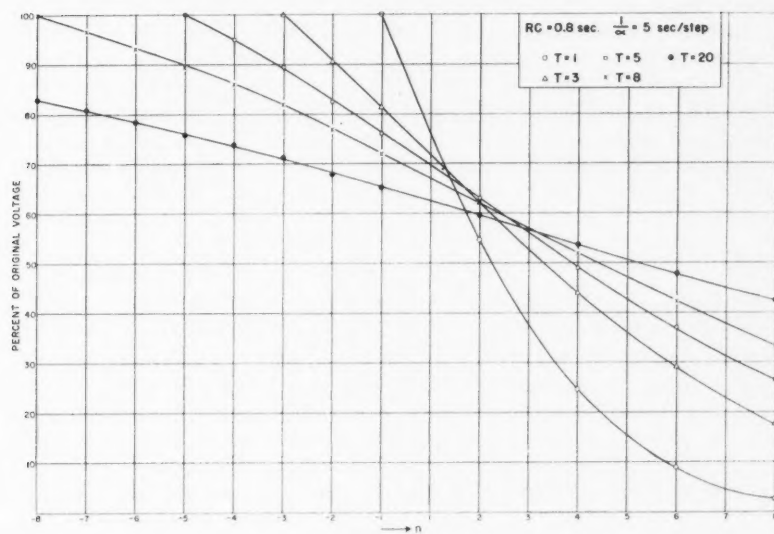


FIG. 4. Data from series II runs.

A typical factor of dispersion D (Aronofsky 1957) is

$$(4.2) \quad D = 10^{-4} \text{ cm}^2/\text{sec.}$$

In series I, RC was equal to 4 seconds, $1/\alpha$ equal to 5.0 seconds; hence, from (3.20) and (3.21)

$$(4.3) \quad t/T = 6.25,$$

$$(4.4) \quad n/x = 125 \text{ cm}^{-1}.$$

This means that 1 cm of the porous medium is represented by 125 RC units in the electrical analogue, and that 6.25 seconds in the analogue correspond to 1 second in the porous medium. From Fig. 3, it appears that after $t = 14$

steps, the skewedness is barely visible. This corresponds to 11.2 seconds in the miscible displacement process during which the front will have penetrated 1.1 mm into the porous medium.

For common values of D , the skewedness of the front should therefore be quite insignificant. However, if D becomes large or if phenomena in the immediate neighborhood of the inflow face are under scrutiny, the curves shown in Figs. 2-4 must be referred to.

ACKNOWLEDGMENTS

The present study was performed at the Production Research and Technical Service Laboratory of Imperial Oil Limited in Calgary. Without the stimulating atmosphere at the Laboratory under the directorship of Mr. J. W. Young, this would not have been possible. The authors wish to thank the management of Imperial Oil Limited for the permission to publish this paper.

REFERENCES

- ARONOFSKY, J. S. 1957. Trans. A.I.M.E. **210**, 345.
SCHEIDECKER, A. E. 1957. The physics of flow through porous media (Univ. of Toronto Press, Toronto).
SCHEIDECKER, A. E. 1958. Trans. Am. Geophys. Union (in press).

DISCOVERY OF Pr¹³⁷¹

CARL DAHLSTROM,² J. S. FOSTER, AND A. L. THOMPSON

ABSTRACT

The neutron-deficient isotope Pr¹³⁷ has been discovered by proton bombardment of natural cerium, chemical separation, and mass determination. Its half-life is 1.5 ± 0.1 hours and the end point of its positron spectrum is 1.7 ± 0.1 Mev. No gamma rays were observed.

INTRODUCTION

In the course of a general study of neutron-deficient isotopes of praseodymium formed under proton bombardment of cerium oxide, the extracted Pr portion of a target exposed at 40 Mev clearly showed Pr¹³⁷ in a mass spectrograph. Thus separated, this isotope repeatedly showed an easily measurable half-life of 1.5 hours. Radiations appeared to be limited to the continuous positron spectrum with end point at 1.7 Mev. The reason that the existence of an isotope with this half-life was questioned by Handley and Olson (1954) is that it does not decay into Ce^{137m} with the 255-kev γ -ray previously thought to be the main means of identifying Ce¹³⁷ (Danby, Foster, and Thompson 1958).

EXPERIMENTAL PROCEDURE

1. Irradiations

The cerium oxide target was prepared by heating available ammonium hexanitrate cerate* at less than 300° C to avoid the formation of a troublesome insoluble oxide. Targets were prepared by packing about 15 mg of the cerium oxide so produced into a 1/8-in. diameter tube formed by wrapping 0.001-in. dural foil round a drill rod. The free edges of this foil were clamped to a dural block which in turn was attached to the water-cooled internal probe. This cooling was necessary to prevent the formation of the insoluble oxide during bombardment. Irradiations from 1/2 to 2 hours' duration were carried out with 20- to 40-Mev protons.

2. Chemical Separation

Cerium differs from its immediate neighbors in that it may exhibit a valence of +4 as well as +3, the normal rare earth valence. The chemical separation of praseodymium from cerium therefore depends upon the oxidation of cerium to its +4 valence state and precipitation of its phosphate, leaving the praseodymium in solution. The detailed procedure was as follows:

The cerium oxide was dissolved by thorough wetting with concentrated nitric acid and heating after the addition of hydrogen peroxide. After disso-

¹Manuscript received August 12, 1958.

Contribution from the Radiation Laboratory, McGill University, Montreal 2, Quebec, Canada.

²Now at Defence Research Board, Ottawa, Canada.

*Primary standard material from G. Frederick Smith Company.

lution, the hydrogen peroxide was removed by repeated evaporation with nitric acid. The cerium in 2 milliliters of ice-cold concentrated nitric acid was oxidized with potassium bromate. After dilution with cold water the cerium was precipitated as phosphate by the addition of phosphoric acid. The precipitate was coagulated by heating to about 50° C and removed by filtration. After the addition of ammonium hydroxide the praseodymium was carried down with the hydroxides of residual cerium and small amounts of lanthanum, praseodymium, and neodymium impurities in the target material (about 20 micrograms in all). This was dissolved in nitric acid and reprecipitated as hydroxide. After washing with acetone and air-drying, the precipitate was dissolved in one drop of nitric acid and transferred to the ion source filament under a heat lamp. The complete series of operations normally took about one and one-half hours.

3. Mass Separations

The mass spectrograph is a Nier sector type instrument in which the ion beam is deflected along a circular path of 6-in. radius and through an angle of 90°. The dispersion along the collector is about 1.5 mm per mass unit at mass 150. The magnetic field of 2700 oersteds is supplied by 10 pairs of magnetron magnets placed at convenient locations round the magnet.

After the loaded filament was mounted in the mass spectrograph, an ion collector in the form of copper foil 2 in. \times 0.002 in. was carefully rubbed with fine emery paper, to remove the oxide, and inserted into the plate holder. The closed system was then pumped down to 10^{-5} mm of Hg in some minutes and the ion accelerating potential set at 750 volts. Under these conditions the isotopes were focused near the high mass end of the collector. The filament current was then slowly raised until the ion current began to register on the output meter of the d-c. amplifier. After adjustment of the focusing potentials for maximum ion current the filament temperature was again slowly raised until the ion current was about 10^{-10} amp. In a few minutes the current became steady and then the accelerating potential was reduced to 700 volts and the filament temperature set to give an ion current of about 2×10^{-10} amp. Under these conditions, the masses were focused near the center of the collector and the sample was depleted in half an hour.

After the copper foil collector had been removed from the spectrograph, no-screen X-ray film was gently pressed against its front surface and three pinholes were made through both foil and film so they might be placed in register later.

After suitable exposure (upwards of 15 minutes) the film was developed to reveal lines corresponding to the positions of active isotopes. Estimates of line intensities at 20 Mev and 40 Mev are represented in Fig. 1. When dry, the film was again placed in register with the foil and the positions of active isotopes marked by pin points. The foil was then cut into narrow strips containing the individual isotopes which were examined separately.

The decay studies were made with an end-on Geiger-Müller tube with 3 mg/cm² mica window set in a lead housing and connected to a scaling circuit.

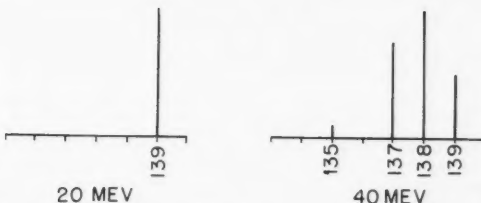


FIG. 1. Mass line intensities (relative) for praseodymium isotopes produced by the bombardment of cerium by protons of energy 20 and 40 Mev.

RESULTS

Mass assignments were made with reference to 4.5-hour Pr¹³⁹, the mass of which was established by Stover (1951) through its well-known daughter Ce¹³⁹ (Hollander, Seaborg, and Perlman 1953). A strong 4.5-hour activity alone was observed under 20-Mev bombardment.

Following 40-Mev bombardment, the same activity was observed and the mass of the immediate neighbour Pr¹³⁸ with 2.0-hour half-life was confirmed.

In addition, a previously unknown activity with a half-life of 1.5 ± 0.1 hours appeared at mass 137.

The decay curves for all three mass separated isotopes are shown in Fig. 2. The positron end-point in the decay of Pr¹³⁷ was shown to be 1.7 Mev from an aluminum absorption curve analyzed by the method of Bleuler and Zunti (1946). No gamma rays were observed from this isotope.

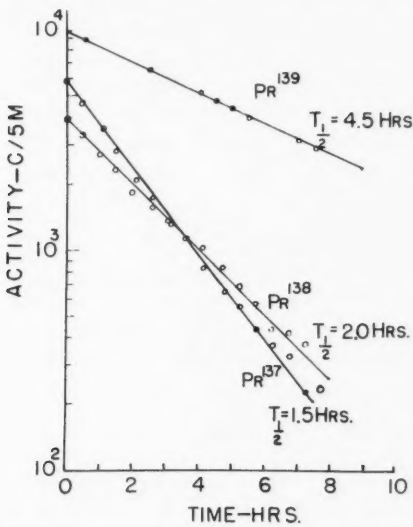


FIG. 2. Decay curves for mass-separated praseodymium of mass 137, 138, and 139.

ACKNOWLEDGMENT

During the period of this investigation, one of us (C.D.) held a Studentship from the National Research Council.

REFERENCES

- BLEULER, E. and ZUNTI, W. 1946. Helv. Phys. Acta, **19**, 376.
DANBY, G. T., FOSTER, J. S., and THOMPSON, A. L. 1958. Can. J. Physics, **36**, 1487.
HANDLEY, T. H. and OLSON, E. L. 1954. Phys. Rev. **96**, 103.
HOLLANDER, J. M., PERLMAN, I., and SEABORG, G. T. 1953. Revs. Modern Phys. **25**, 469.
STOVER, B. J. 1951. Phys. Rev. **81**, 8.

SUCCESSIVE DECAYS FROM Pr^{137} AND Ce^{137m} : DECAY OF ADJACENT PRASEODYMIUM ISOTOPES¹

G. T. DANBY,² J. S. FOSTER, AND A. L. THOMPSON

ABSTRACT

The decay of Pr^{137} entirely to a 9.0-hour ground state of Ce^{137} was independently discovered. By allowed electron capture, Ce^{137} decays predominantly to a low-lying state of La^{137} , with only a 3% branching to a 440-kev excited state. The 440-kev transition is at least predominantly $E2$ in character.

A 34.4-hour isomeric state produced by the $\text{La}^{139}(\rho, 3n)\text{Ce}^{137m}$ reaction decays by a 254.5-kev $M4$ transition to the 9-hour ground state. A 0.6% branching was found from the isomeric state directly to a small group of apparently high spin states in La^{137} .

Studies of mass-separated isotopes confirmed the existence of 1.5-hour Pr^{137} and 1.0-hour Pr^{136} . The K -capture to positron branching ratios observed in the decay of Pr^{139} , Pr^{138} , Pr^{137} , and Pr^{136} show that these isotopes decay by allowed transitions to their cerium daughters. Characteristic gamma rays were observed.

INTRODUCTION

Since the discovery of Pr^{137} (Dahlstrom, Foster, and Thompson 1958) was not confirmed by others (Handley and Olson 1954), this work was initially undertaken 4 years ago to discover the reasons. The clarification rests not only on the fact that Pr^{137} decays entirely to a newly observed 9-hour ground state of Ce^{137} , but also on the recognition that the '36-hour' γ -ray formerly used to identify Ce^{137} in reality arises from a 254.5-kev $M4$ transition from 34.4-hour Ce^{137m} to the ground state. Meantime these isomeric and ground states of cerium were independently found by Brosi and Ketelle (1955, 1956).

In addition, however, the mass separations of Pr^{137} and its neighbors Pr^{139} , Pr^{138} , and Pr^{136} have permitted a study of positron and gamma-ray spectra from individual isotopes and this study has been supplemented by more precise measurements of conversion electron spectra from chemically separated sources of praseodymium and cerium. Moreover, the K -capture to positron branching ratios were measured for all four mass-separated praseodymium isotopes. In each case, experiment compared with theory indicates an allowed transition to the ground state of the cerium daughter.

STUDIES OF MASS-SEPARATED PRASEODYMIUM ISOTOPES

The detailed target arrangements as well as the methods used in chemical separations for both praseodymium and cerium studies are given in Appendix I. This also includes the methods of preparing sources for the β - and γ -ray spectrometers and the surface deposits for the hot filament source in the mass spectrograph.

¹Manuscript received August 12, 1958.

Contribution from the Radiation Laboratory, Department of Physics, McGill University, Montreal 2, Quebec, Canada.

²Now in Accelerator Development Department, Brookhaven National Laboratory, Upton.

(A) MASS SEPARATIONS

Mass separation was essential to the measurement of X-rays and positrons from individual decay systems, since these radiations are common to all isotopes investigated. Fortunately, for this purpose, ion emission from praseodymium is about 100 times as efficient as from cerium. Consequently, each separated sample was initially almost entirely praseodymium and this made the analysis of the decay of the parent to its cerium daughter much simpler. Owing, however, to the time required to prepare sources and the low over-all efficiency of the spectrograph, these studies are fully effective only for isotopes of greater than 1-hour half-life.

The purity of the mass-separated samples was ensured after a redesign of the collector system as detailed in Appendix II, where some improvements in the efficiency of the mass spectrograph are also described.

(B) DETECTION OF γ -RADIATIONS

The γ -rays from mass-separated isotopes were detected and recorded by a 28-channel "kicksorter" (Bell and Skarsgard 1956). This instrument was also used in the study of annihilation radiation and X-rays. The NaI (Tl) crystal detector of moderate size is in contact with a 6292 DuMont photomultiplier mounted in a lead castle lined with iron. By earlier calibrations with standard sources, the efficiency of this detector for γ -rays is known as a function of energy for source distances down to 3 cm from the crystal. This calibration was used in later γ -ray studies of chemically separated sources.

With the relatively weak samples from the mass spectrograph, however, the simultaneous handling of four sources required the maximum counting rates realized by placing the samples in contact with the crystal cover. Each separated active foil was mounted between two layers of scotch tape and then stretched across a lucite ring which fitted round the crystal cover. When annihilation radiation was counted, an additional 1/4 in. thick aluminum disk was placed over the foil, thus sandwiching the source between disk and crystal cover.

An extension to the earlier calibration of the detector was therefore made to estimate the absolute efficiencies of counting K X-rays and positrons when the sources are so close to the crystal. Stronger sources of K X-rays (Ce^{139} , lanthanum 33 kev) and positron annihilation radiation (Na^{22}) were counted when placed (1) at 3 cm and (2) against the crystal cover. From (1) the emission rates were determined and from (2) the counting efficiencies were calculated for the contact position. A detailed discussion of efficiencies is given in Appendix III.

(C) OBSERVATIONS ON MASS-SEPARATED Pr ISOTOPES

A preliminary survey with the mass spectrograph was made by collecting the active isotopes on a plane foil which was then placed in contact with X-ray film. For irradiations at 45 to 55 Mev on natural cerium, short contact exposures made immediately after mass separation revealed intense lines at masses 139, 138, 137, and 136. This indicates that lighter isotopes, if present, are too short-lived for this method of study.

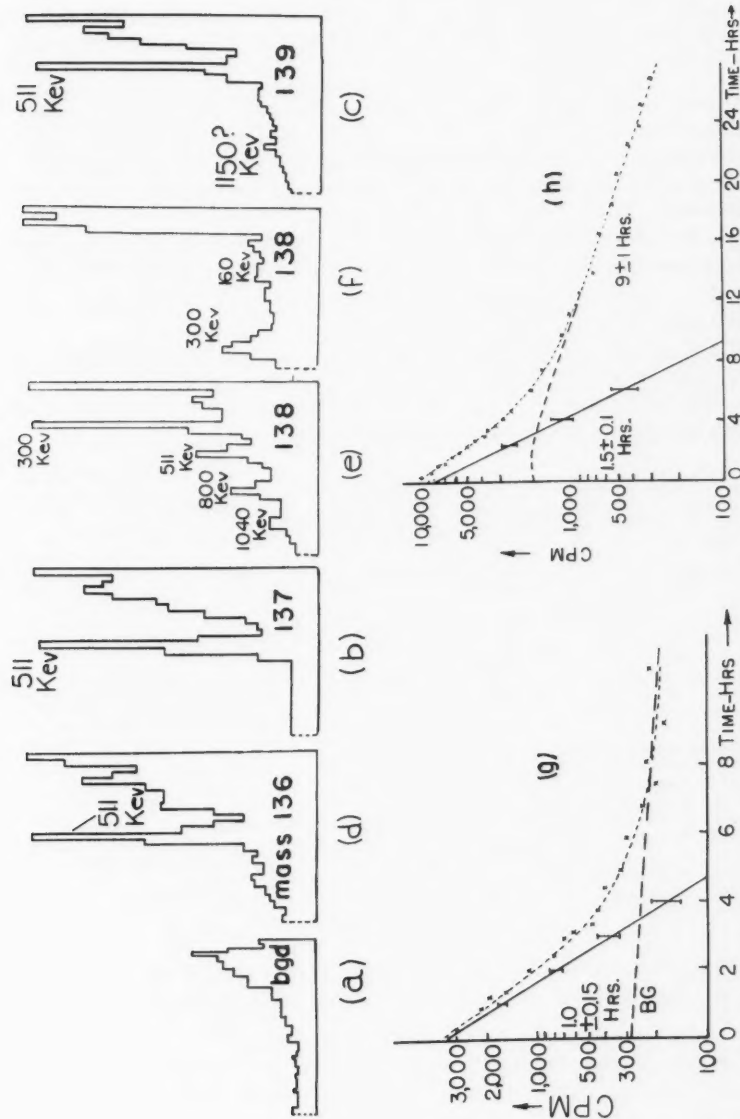


FIG. 1. Studies of mass-separated praseodymium isotopes. In the top row gamma spectra as recorded by the kicksorter. The full scale is 1000 counts and recording times are, respectively: (a) background, over energy range of (b) and (d), 635 sec; (b) 435 sec; (c) 60 sec; (f) low energy range, (g) 344 sec. Lower curve (h) decay of Pr-136 X-rays, (h) decay of Pr-137 X-rays.

Following a 55-Mev bombardment, separated activities were next allowed to decay for 12 hours and then a contact exposure was made for several days. This showed lines at masses 139, 137, 135, and 134. The absence of activity at 138 and 136 was due to the decay of Pr^{138} and Pr^{136} to stable cerium isotopes.

Pr^{137}

The decay of annihilation radiation from this isotope consistently gave the 1.5 ± 0.1 hour half-life. No γ -rays of this period were observed. An upper limit of about 10% of the annihilation intensity can be set for undetected γ -rays. Such upper limits quoted in this paper are for the uncorrected full energy peak intensities (Fig. 1 *a, b*).

However, the decay of the X-rays showed a half-life of 1.5 hours growing into 9.0 ± 1 hours (Fig. 1, *h*). Evidently the 1.5-hour transition is to the previously unknown Ce^{137} ground state which decays by electron capture with a 9-hour half-life.

After the 1.5-hour annihilation radiation had decayed to insignificance, a very weak 440-kev γ -ray became clear in Ce^{137} .

The branching ratios of K -capture to positron emission for this and the following praseodymium isotopes are presented in Table I.

TABLE I
LOG ($f t$) VALUES FOR POSITRON DECAY OF Pr^{139} , Pr^{138} , Pr^{137} , AND Pr^{136}

Isotope	Observed branching ratio $f = \lambda_k/\lambda_+$	E (Mev) observed	W_0 (calc. from E)	W_0 (calc. from f)	Log t_+	Log ($f t$)_+
Pr^{139}	11.3 ± 1.0	$1.0 \pm 0.1(a, b)$	3.0 ± 0.2	3.2 ± 0.1	5.3 ± 0.1	5.6 ± 0.2
Pr^{138}	4.5 ± 1.2	$1.4 \pm 0.1(a)$ $1.5 \pm 0.1(b)$	3.8 ± 0.3	3.0 ± 0.2	4.6 ± 0.1	5.4 ± 0.2
Pr^{137}	2.05 ± 0.3	$1.8 \pm 0.1(b)$	4.3 ± 0.2	4.4 ± 0.2	4.2 ± 0.2	5.3 ± 0.3
Pr^{136}	1.8 ± 0.4	$2.0 \pm 0.1(a)$	4.9 ± 0.2	4.8 ± 0.3	4.0 ± 0.2	5.5 ± 0.3

NOTE:

(a) Handley and Olson (1954).

(b) Dahlstrom (unreported).

Column 2: K -capture to positron emission branching ratios.

Column 3: positron maximum energies.

Column 4: nuclear energy differences (Mev) calculated from the positron end points.

Column 5: nuclear energy differences calculated from the branching ratios on the assumption of "allowed shape" transitions (Feenberg and Trigg 1950).

Column 6: logarithm of the positron partial half-life, $t_+ = (1+f)t$.

Column 7: logarithm of the positron comparative half-life. ' f'_+ ' is given as a function of W_0 by Feenberg and Trigg (1950).

Evidently 34.4-hour Ce^{137m} does not appear in the decay of Pr^{137} and is, of course, the reason Handley and Olson did not detect the latter.

Pr^{139}

There are no strong γ -rays from this isotope. Indeed, the only indication of rays with the known half-life of 4.5 hours was a possible 1150-kev peak consistently appearing with about 3% of the annihilation intensity (Fig. 1, *c*).

After the 4.5-hour parent had largely decayed, the 166-kev γ -rays from 140-day Ce^{139} appeared with low intensity.

Pr¹³⁸

Pr¹³⁸ displayed a large number of γ -rays in addition to the annihilation radiation and X-rays. With a half-life of 2.1 ± 0.05 hours, it decayed to a stable daughter, *Ce¹³⁸*. Intense γ -rays were observed at 300 ± 10 , 800 ± 10 , 1040 ± 10 kev, and 1590 ± 20 kev (Fig. 1, e and f). If γ -rays of still higher energy exist, their photoelectric peaks are less than 10% of that for 1590 kev.

Pr¹³⁶

This isotope of relatively short life gave a low yield in the mass spectrograph. The weak sources nevertheless gave a half-life of 1.0 ± 0.15 hours on several occasions (Fig. 1, g). This confirms a previous assignment by Handley and Olson (1954). However, no γ -rays were observed, and an upper limit of 10% of the annihilation intensity can be put on any that may be present (Fig. 1, d).

Additional Data from Chemically Separated Praseodymium

Cerium was bombarded with 50-Mev protons and combined praseodymium activities were separated chemically. The conversion electron spectrum was studied in a Släts-Siegbahn spectrometer of 2.1% resolution and 1.4% transmission.

A strong positron continuum and a composite Auger electron peak decayed in a complex manner.

K- and *L*-conversion lines for a single transition of 300 ± 5 kev were very prominent (Fig. 2, a). The half-life was 2.1 ± 0.05 hours and the $K/(L+M+)$ ratio was 2.2 ± 0.1 .

Weak *K*-conversion lines arising from 800 ± 7 and 160 ± 2 kev transition also

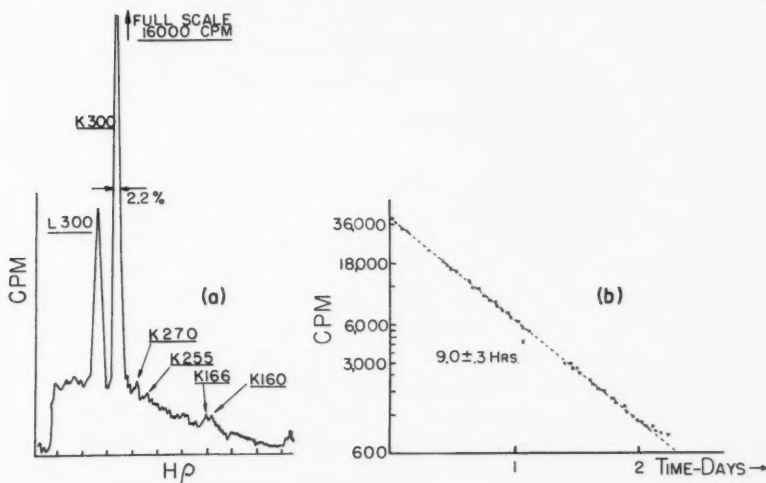


FIG. 2. (a) Conversion spectrum of combined praseodymium isotopes chemically separated from cerium target following bombardment by 50-Mev protons. (b) Decay of 440-kev gamma ray of *Ce¹³⁷* daughter of the praseodymium chemically separated from a cerium target subjected to 40-Mev proton bombardment.

were present with a 2.1-hour half-life. The relatively accurate value for 160 kev is made possible by a convenient comparison with the known 166-kev transition of Ce¹³⁹. K-conversions for both 800 and 160 kev are about 3–5% of the corresponding conversions at 300 kev.

A few weak peaks observed with long half-lives will come up in later discussions. They are K-conversions due to (1) 255 ± 5 kev (Ce^{137m}); (2) 280 ± 5 kev (Ce¹³⁶), and (3) a somewhat stronger conversion at 440 ± 5 kev (Ce¹³⁷).

STUDY OF Ce¹³⁷ FORMED BY PRASEODYMIUM DECAY

(a) Gamma-Ray Spectrum

A cerium target was bombarded at 40 Mev and the praseodymium so produced was immediately separated chemically. After waiting 6 hours for most of the 1.5-hour Pr¹³⁷ to decay, the daughter cerium was extracted. Fortunately, only Ce¹³⁷ and 140-day Ce¹³⁹ are thus obtained with appreciable activities. Of these, the latter emits only one γ -ray (166 kev). Thus the spectra of Ce¹³⁷ may be studied with a minimum of contaminating radiations.

The cerium daughter (after repeated chemical purification cycles to remove all traces of praseodymium) revealed a γ -ray at 440 kev and a very strong X-ray peak. The well-known 254-kev γ -ray, however, was not observed in the cerium daughter. If present, it was less than 1% of the 440-kev peak intensity. Moreover, no additional γ -rays or annihilation radiation were detected from the cerium. An upper limit of 0.25% of the 440-kev peak intensity is estimated for possible higher energy gamma rays.

The half-life of the 440-kev transition, measured on two occasions, was 9.0 ± 0.3 hours (Fig. 2, b). The X-radiation also decayed with a 9.0-hour half-life until it reached about 1% of its original activity. The mass separations had shown that the 9.0-hour activity was in mass 137 and the chemical separations showed that this activity was associated with the decay of cerium. The strong X-rays therefore indicate that Ce¹³⁷ decays by electron capture—mainly to the ground state of La¹³⁷, with only a weak branching to a 440-kev level.

This branching ratio will be considered later. Here it is important to note that the 9.0-hour X-radiation fades into a very weak contribution predominantly arising from 140-day Ce¹³⁹. This very small background correction permits an accurate measurement of the K X-ray intensity from Ce¹³⁷.

Incidentally, the *original cerium target* does emit the 34-hour, 254-kev γ from Ce^{137m}, which is formed directly in the target through a relatively weak ($p, p 3n$) reaction.

(b) Conversion Electron Spectrum of Ce¹³⁷

The praseodymium separated from a cerium target which had been bombarded at 50 Mev was allowed to decay into cerium which was then chemically separated to provide a source (mainly Ce¹³⁷) for a Slatis-Siegbahn spectrometer.

Auger electrons provided the only obvious peak. However, a careful manual scan was made over the momentum region corresponding to 440-kev total energy. At the appropriate position, a K-conversion peak was unmistakably observed with very low intensity.

(c) *Branching Ratio to 440-kev Level*

This branching ratio was estimated to be about 3% in the following manner:

While the disintegrations to the 440-kev level are obtained from the peak intensity and efficiency of counting, only the *K*-electron captures are directly given by the observed *K* X-rays. These actually receive a negligible contribution from the conversion of 440 kev, but they fail to indicate other types of electrons captured and this supplement must now be estimated.

Theoretical probabilities for electron capture from the *K* and *L* shells have been calculated by Brysk and Rose (1955). Fortunately the *K*-capture fraction of the total capture varies slowly with the disintegration energy over a range extending considerably above the *K*-capture threshold. Here the *L_I*-subshell contribution (which is responsible for most of the *L*-shell contribution) is nearly a constant fraction of the *K*-capture. From the absence of positrons, the nuclear energy difference is not large and since it is not critical we take ' $W_0 = 0$ ' in an "allowed transition".

Under the above conditions, the theoretical ratios are $L_I/K = 0.13$ and $L_{II}/K = 0.01$. The L_{III} contribution is negligible.

For the remaining shells, an estimate of 7% of the *K*-shell contribution was made, assuming an inverse cube variation with the principal quantum numbers.

In this way the ratio of total captures to *K* captures was estimated to be 1.21. Allowing for counting efficiencies and increasing the *K* X-rays by 21% to get the total captures, it was found that the ratio of the disintegrations to the 440-kev level to the total disintegrations was 0.03.

CERIUM^{137m}

(a) *Gamma-Ray Spectrum*

A lanthanum target bombarded at 30 Mev (i.e., below the threshold for Ce¹³⁵ production) yielded mainly La¹³⁹($p, 3n$)Ce¹³⁷ and Ce^{137m} with only a relatively small intensity from Ce¹³⁹ disintegrations. This fact simplified the study of gamma rays from Ce^{137m}.

The gamma-ray spectrometer disclosed very intense X-rays, strong γ -rays at 255 and 440 kev, and a much weaker group round 810 kev.

Measured over five half-lives, the 255-kev γ -ray had a half-life of 34.4 ± 0.3 hours and the 800-kev γ -ray had the same period. On the other hand, the X-rays and the 440-kev γ -ray showed a composite decay. After an initial half-life which was fitted to 9 hours, they also decayed with a 34.4-hour period. No activity which could be attributed to the decay of La¹³⁷ was detected.

No annihilation radiation was observed. The upper limit on unobserved high energy γ -rays can be set at 0.5% of the weak 800-kev transition. An unsuccessful search was also made for low energy rays down to a 10-kev limit of detection (see, however, Brosi and Ketelle (1956)).

After equilibrium was reached with the 34.4-hour half-life, the intensity ratios, averaged over several runs, for the

X-rays	255 γ	440 γ	810 γ
were	1.00	0.081	0.020

The accuracy for the relative intensities of the 255- and 440-kev γ -rays

should be equal to that of the counting efficiency values, or about 10%. For the weaker 810-kev γ -ray, it is better than 20%. The accuracy for X-ray intensities is discussed in Appendix III.

(b) *Conversion Electron Spectra*

Sources of Ce^{137m} produced by 30-Mev bombardments on lanthanum were also scanned by the lens spectrometer. Extremely strong conversion electron peaks due to the 255-kev transition were observed with a 34.4 ± 0.3 hour half-life (Fig. 3d). A typical conversion spectrum for the 255-kev transition is reproduced in Fig. 3a, and shows that $K/L = 2.9$, allowing 25% for the $M+$ contribution.

The comparatively weak electron peaks for the 440 ± 5 kev transition are also shown in Fig. 3b; the $K/L + M+$ ratio is 5 ± 0.5 .

Using a very strong source and counting manually over several days, the conversion spectrum for the groups of transitions round 810 kev was obtained (Fig. 3c). Overlapping of lines makes the assignment of K/L ratios difficult.

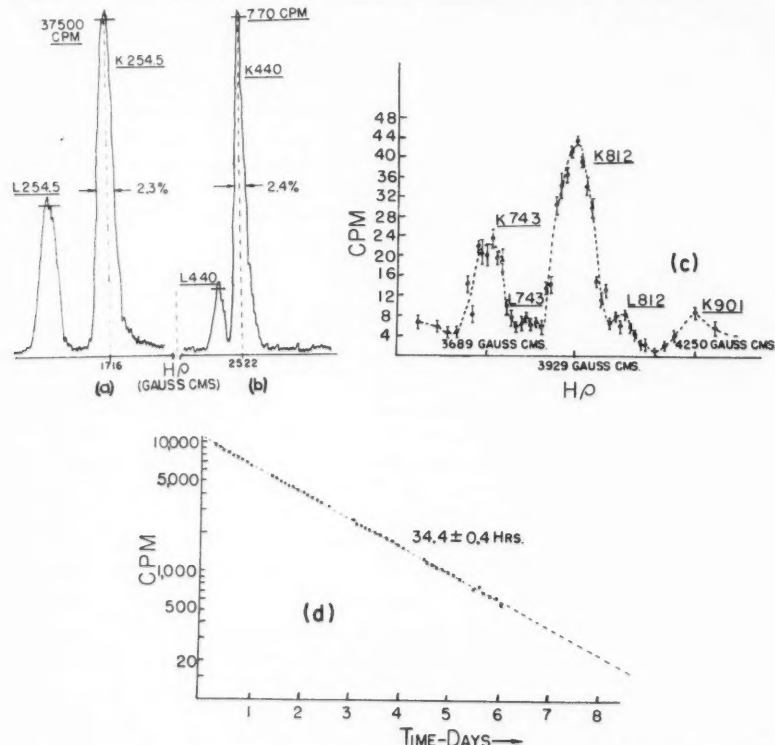


FIG. 3. Activities in the decay of Ce^{137m} formed in a lanthanum target under 30-Mev proton bombardment. (a) and (b) Conversion spectra from 255- and 440-kev transitions respectively. (c) Conversion spectra from close group of transitions near 800 kev. (d) Decay of 255-kev K -conversion line.

For the strongest lines, due to 812 ± 7 kev, the $K/L + M +$ ratio appeared to be 6.3 ± 1.2 .

The ratios of the K -conversion intensities for the transitions

	255	440	812 kev
were	1	5.35×10^{-4}	2×10^{-5} to within 10%.

Comparing the intensity of the K -conversion peak for 255 kev with the absolute γ -ray intensity, the K -conversion coefficient was derived, taking into account the known transmission of the lens spectrometer. This gave a K -conversion coefficient of 4.8 within 30%. For $Z = 58$ and $k = 0.5$, this result indicates that it is an $M4$ transition (Rose and Goertzel 1955).

Using a source which gave 10^6 c.p.m. in the 255-kev K -conversion peak, a manual scan disclosed no low energy conversion peaks (above 10 kev) except those due to Auger electrons. An unsuccessful search was also made for a possible transition from some of the 812-kev groups to the 440-kev level. The upper limit for such a transition is less than 1% of the 440-kev K -conversion intensity.

(c) Results with 180° Spectrograph

A direct method of finding the element in which the 255-kev transition takes place is to make accurate measurements of the conversion electron energies and compare their differences with the corresponding differences in electron binding energies for adjacent elements.

The spectrograph has a resolution of 0.2% and gave results accurate to about ± 0.2 kev (see Fig. 4).

TABLE II
RESULTS WITH 180° SPECTROGRAPH

	<i>K</i>	Line				
		<i>L</i> ₁	<i>L</i> _{II}	<i>L</i> _{III}	<i>M</i>	<i>N</i>
Energy (kev)	214.02	248.13	248.46	248.92	253.33	254.41
Differences		<i>K</i> - <i>L</i> ₁	<i>K</i> - <i>L</i> _{II}	<i>K</i> - <i>L</i> _{III}	<i>K</i> - <i>M</i>	<i>K</i> - <i>N</i>
Observed		34.11	34.44	34.90	39.31	40.39
Difference in Ce		33.87	34.26	34.70	39.2	40.2
Difference in La		32.66	33.02	33.43	37.8	38.7

From this comparison, it is clear that the 254.5-kev conversions take place in cerium.

Supplementary evidence for the $M4$ classification of the 255-kev transition was obtained through visual estimates of the intensity ratios for the L lines shown by the microphotometer trace (Fig. 4). The resulting estimates of L -conversion coefficient ratios now supplement the K/L measured by the lens spectrometer and the corresponding ratios for $M3$, $M4$, and $M5$ transitions respectively are added for comparison (Rose and Goertzel 1955) (see Table III).

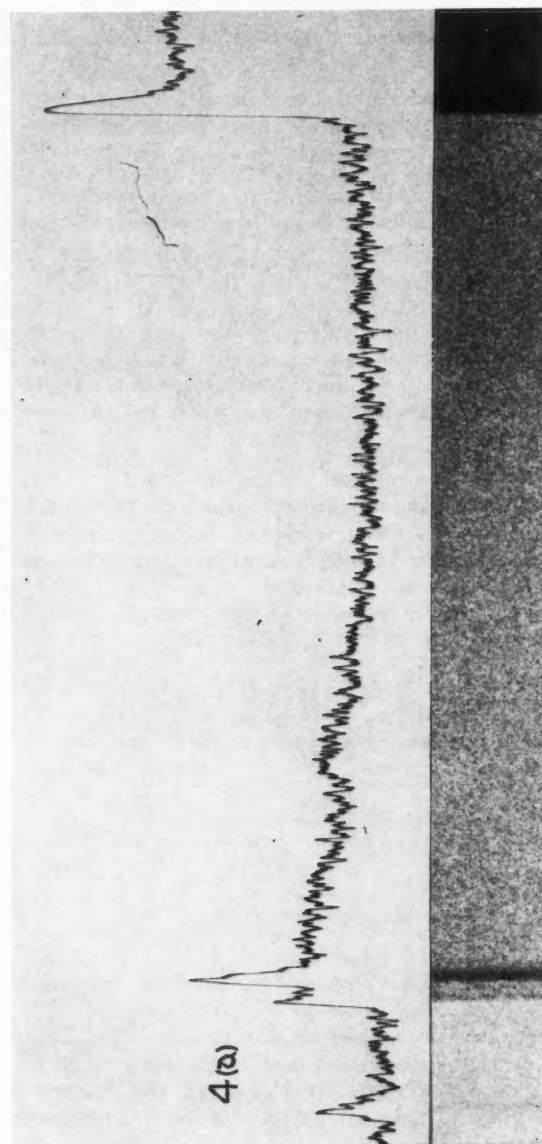


FIG. 4(a). Spectrogram and trace showing K - and L -conversion lines arising from the 255-kev transition from Ce^{137m}

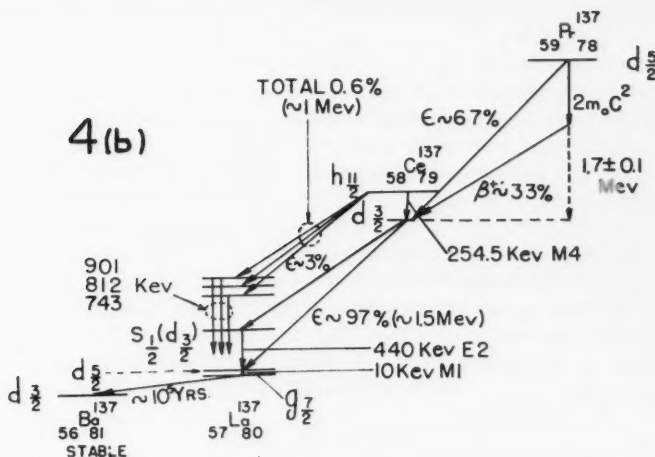
FIG. 4(b). Tentative scheme for successive decays from Pr^{137} and Ce^{137m} .

TABLE III

$K/\Sigma L$	2.9	4.4	3.0	1.8
$L_{\text{I}}/L_{\text{II}}$	3 to 6	5.7	4.3	3.5
$L_{\text{I}}/L_{\text{III}}$	1.5	4.1	1.75	1.0
$L_{\text{II}}/L_{\text{III}}$	0.25 to 0.5	0.7	0.41	0.3

Lower order multiplicities of either character are rejected by the long half-life. The higher electric multipoles are eliminated by the small L_{II} contribution. A comparison of the observed with the calculated ratios establishes rather firmly the $M4$ multipolarity of the 255-kev transition.

(d) Coincidences

The 440-kev γ -rays were coincident with X-rays; as expected, the 255 γ 's were not.

Analysis of Results of Ce^{137m} Decay

The decay of the K -conversion electron peaks for the group of transitions centered at about 810 kev showed the simple 34.4-hour half-life. Thus, while Ce^{137m} decays predominantly by the 254.5-kev $M4$ transition to Ce^{137} , a weak branching occurs to a closely spaced group of excited levels in La^{137} . For this group, the γ -ray spectrum was unresolved, and the K/L ratios were too confused to permit any assignments of multipolarity.

However, the branching to the group as a whole was calculated from the intensity of its unresolved γ -rays, compared to the total intensity of the 254.5-kev transition. The latter was obtained from the 254.5 γ -ray intensity and the total conversion coefficient. This gave a branching of 0.6% to the group as a whole.

The ratio of the K -conversion coefficients of the 440-kev and 254.5-kev transitions was obtained from the ratios of their respective γ -ray and K -conversion intensities. This gives $a_K = 0.012 \pm 0.002$ for the 440-kev transition, assuming the theoretical value for a 254.5-kev $M4$ transition is $a_K = 5.68$. The interpolated theoretical values for 440 kev are $a_K = 0.010$ for $E2$, and $a_K = 0.017$ for $M1$.

The K/L ratio, assuming a 25% $M+ \dots$ contribution to the L -conversion peak, gave $K/L = 6.3 \pm 0.6$ for the 440-kev transition. The theoretical values are $K/L = 6.0$ for $E2$, and $K/L = 8.1$ for $M1$, indicating the transition is at least predominantly of an $E2$ nature.

A partial list of new calculations of the conversion coefficients, taking into account the finite size of the nucleus (Sliv, privately obtained) have the a_K for the 254.5 kev slightly reduced from the values of Rose and Goertzel (1955). A value about 10% less is indicated, giving for the 440-kev transition an $a_K = 0.013 \pm 0.002$. The theoretical values of Sliv for the 440-kev transition are,

$$a_K(E2) = 0.012 \pm 0.002,$$

$$a_K(M1) = 0.022 \pm 0.007.$$

The K/L ratios will not be significantly changed. Thus the assignments made are unaltered by the Sliv calculations.

The electron capture branching intensity to the 440-kev level was also calculated from the 254.5- and 440-kev γ -ray intensities. The total Ce^{137m} disintegration rate was obtained, using a_T . From this, the Ce^{137} disintegration rate was calculated for the two states in secular equilibrium, and compared to the 440-kev γ -ray intensity, giving a 2% branching. This calculation is independent of counting X-ray intensities.

This branching was also calculated in terms of the ratio of the 440-kev γ -ray to the total K X-ray intensity, for Ce^{137m} and Ce^{137} in secular equilibrium. The Ce^{137m} disintegration was expressed in terms of cerium K X-rays, using a_K , a_T , and the fluorescent yield. The Ce^{137} disintegration was expressed in terms of lanthanum K X-rays, using the fluorescent yield and the K to total capture ratio.

Ignoring the small percentage difference in the counting efficiencies for cerium and lanthanum X-rays (a negligible effect on the answer, which is itself small), all the K X-rays can be added indiscriminately. From the ratio of the 440-kev intensity to the Ce^{137} disintegration rate expressed in terms of the K X-ray intensity, a branching of 3% was obtained.

In an earlier section, the value of 3% was also calculated for the decay of the 9-hour ground state alone. Since both calculations from X-ray intensities give the same result, this indicates the self-consistency of the interpretation of the decay. The value obtained independent of X-ray measurements was 2%. However, the discrepancy is not large considering the many factors involved. The total counting efficiencies for the K X-rays, if in error, are most likely to be too large. This would make the branching slightly less than 3%. On the other hand, reducing a_K for the 254.5-kev transition, as is indicated by the Sliv

results, would raise the 2% figure somewhat. The three calculations give essentially the same result, or about 3%.

By analyzing the decay of Ce^{137} to La^{137} , estimates of the nuclear energy differences involved were arrived at. No positrons were observed in the decay of Ce^{137} , and an upper limit of 1% of the K -capture intensity can conservatively be placed on them. This indicates the disintegration energy of Ce^{137} to the ground state of La^{137} cannot be more than about 1.5 Mev. Furthermore, a lower limit of about 440 kev can be set, since there is a branching to the 440-kev level.

For K -capture, the " f_k " factor in the comparative half-life can be found, knowing the nuclear energy difference W_0 , Z , and A (Feenberg and Trigg 1950). Calculating the partial half-life to the ground state, and " f_k " between the limits of energy given above, the value is $4.25 < \log f_k t < 5.5$.

For the transition from Ce^{137} to the 440-kev level, applying the appropriate energy limits and partial half-life, the value is

$$1 < \log f_k t < 5.6.$$

Both these results indicate allowed transitions of disintegration energy about the high end of the estimated range.

β -Decay energy systematics (Way and Wood 1954) support this result, predicting a $Q = 1.7$ Mev for Ce^{137} to La^{137} , ground state to ground state transition. Taking $Q = 1.5$ Mev gives about 1 Mev for the energy difference between Ce^{137m} and the 812-kev level. Using the partial half-life of the (0.6%) group as a whole, this gives a value

$$\log f_k t = 7.8.$$

Consider the levels at 743, 812, and 901 kev. Since the energy of the electron capture transition is high in all cases (about 1 Mev for the 812 kev), the " f_k " contribution to " $f_k t'$ " is considerably smaller than the " t' " part, and furthermore, doesn't vary much over the range of energy involved. The intensity of the three transitions are of the same order. Thus their partial half-lives vary certainly by less than an order of magnitude, and the logarithms will vary by less than unity. Thus a $\log f_k t \sim 8$ applies for all three, indicating that first forbidden, or first forbidden unique, transitions are probable.

DISCUSSION

(1) The Mass 137 Chain

The decay of 1.5-hour Pr^{137} through 9-hour Ce^{137} , and long lived La^{137} to stable Ba^{137} , produces no intense characteristic γ -rays. The intense 254.5-kev transition of Ce^{137m} , which had been erroneously considered from the ground state of Ce^{137} , is completely absent in this decay.

The information obtained on Ce^{137} agrees with that of Brosi and Ketelle (1955), who produced Ce^{137} by (n, γ) reactions on cerium enriched in Ce^{136} . They also obtained an 8.7 hour half-life, decaying by electron capture to La^{137} , with a 3% branching to a 445-kev level. They assigned the transition

from this level as either an $E2$ or an $M1$, which is in essential agreement with the present results.

The 180° conversion electron spectrograph definitely established that the 254.5-kev $M4$ transition is in cerium. Furthermore, since the 9.0-hour Ce^{137} grows into secular equilibrium with the 34.4-hour period, and since the mass assignment of the former was directly established, the mass assignment of the isomer Ce^{137m} is also definite.

Brosi and Ketelle (1955) also produced Ce^{137m} , by α -particle bombardment on BaF_2 . They obtained a 34.5-hour half-life for the isomeric state, and on the basis of its K -conversion coefficient and a critical absorption experiment on the K X-rays, also assigned it to a $M4$ isomer in Ce^{137} .

The low intensity group of 34.4-hour transitions with the main component at 812 kev indicates electron capture directly from the isomeric state to excited states in La^{137} . These levels do not cascade through the 440-kev level.

The spin of Pr^{141} has been measured as $5/2$. The single particle Shell Model (Mayer 1950) predicts a $g_{7/2}$ ground state for $Z = 57$ (La), and a $d_{5/2}$ for $Z = 59$ (Pr). Thus Pr^{137} is expected to have a $d_{5/2}$ ground state.

The ground state of Ce^{137} is predicted to be probably $d_{3/2}$, with the $s_{1/2}$ not lying much above it. A plot of the energy differences between the $3s_{1/2}$ and the $2d_{3/2}$ levels for odd A , odd N , isotopes as a function of N indicates a small energy difference for Ce^{137} , with $d_{3/2}$ probably the ground state (Goldhaber and Hill 1952).

For odd A nuclei with the number of the odd nucleon between 50 and 82, all states have even parity, except when the odd nucleon is in the $h_{11/2}$ excited state. Pr^{137} does not decay to the $h_{11/2}$ level, so the transition involves no parity change and the $\log ft$ value makes the allowed assignment unambiguous, since second forbidden would be inconsistent with the results. Thus the predicted $d_{5/2}$ to $d_{3/2}$ transition is supported by the experimental observations.

An $s_{1/2}$ ground state for Ce^{137} would be inconsistent with observations of the decay of Pr^{137} , unless it lay just a few kiloelectron volts below the $d_{3/2}$ state. However, the decay to La^{137} supports the $d_{3/2}$ ground state, as will be shown later. This is similar to Ce^{139} , which also has a $d_{3/2}$ ground state (Ketelle, Thomas, and Brosi 1956).

In Fig. 4(b) a decay scheme for Pr^{137} is proposed.

The $M4$ isomeric transition from Ce^{137m} is consistent with predictions based on neighboring odd A , odd N isotopes (Goldhaber and Hill 1952). A plot of the energy difference between the $h_{11/2}$ and $d_{3/2}$ levels, for $N = 79$, indicates about 310 kev as the expected value for Ce^{137m} .

No evidence for any decay of Pr^{137} through Ce^{137m} was found, which is consistent with the above assignments predicting a third forbidden transition from Pr^{137} to Ce^{137m} . This shows, further, that Pr^{137} could not have a $g_{7/2}$ ground state, since the transition to the isomeric state would then be favored over that to the ground state.

The independent particle model suggests a $g_{7/2}$ ground state for La^{137} , with the $d_{5/2}$ level lying just above, and with additional $d_{3/2}$ and $s_{1/2}$ excited states.

With an allowed transition from the ground state of Ce^{137} taking place, a $d_{5/2}$ ground state was indicated, unless the $g_{7/2}$ level lay only a few kiloelectron volts below the $d_{5/2}$. This supports $d_{3/2}$ as the ground state of Ce^{137} since $s_{1/2}$ would be inconsistent. Stable Ba^{137} , with a measured spin of 3/2, has a $d_{3/2}$ ground state.

The interpretation of La^{137} as having a $d_{5/2}$ ground state would be consistent with the observed decay of Ce^{137} , including allowed electron capture to the 440-kev level followed by an $E2$ transition. However, the decay of the ground state to Ba^{137} would then be allowed. To get a very long half-life would require an extremely low energy for the transition. The β -decay systematics (Way and Wood 1954) indicate a value of the order of 200 kev for this transition. As an alternative interpretation, a $g_{7/2}$ ground state for La^{137} would produce a second forbidden transition, and thus account for the long half-life (see below).

Brosi and Ketelle (1956) produced La^{137} by bombarding natural cerium with slow neutrons. They obtained barium K X-rays in the decay and estimated the half-life as $6 \pm 2 \times 10^4$ years. In addition they found a 10-kev $M1$ transition in La^{137} , in prompt coincidence with K X-rays and the 440-kev transition. The intensities indicated that practically all capture events go through the $M1$ transition. Their results completely supported the $g_{7/2}$ level as the ground state, the 10-kev $M1$ transition being from the $d_{5/2}$ level to the ground state.

The low-lying levels in La^{137} would appear to be single particle levels. The 440-kev transition is at least predominantly $E2$ in character, which could indicate a strong transition from the L -forbidden $s_{1/2}$ state. In support of this interpretation, the $s_{1/2}$ level would decay by an $M3$ transition to the $g_{7/2}$ ground state. The half-life of this transition would be long compared to the cascade through the $d_{5/2}$ level, which is consistent with observations. On the other hand, for an initial $d_{3/2}$ level, a predominantly $M1$ transition to the $d_{5/2}$ level would be expected, and appears less favored. In any event, the evidence is for a predominantly $E2$ transition.

The values of $\log ft$ indicate probable first forbidden, or first forbidden unique transitions from Ce^{137m} to the three high energy levels in La^{137} . Thus their parity should be opposite to that of the $h_{11/2}$ state, or the same as the $g_{7/2}$ ground state of La^{137} . Furthermore, high spins $\geq 9/2$ are favored since no cascade transitions through the 440-kev level occur. These levels do not appear to be easily interpretable. Purely from the viewpoint of the spins and parities favored, the results would be consistent with the presence of rotational levels of the $g_{7/2}$ or $d_{5/2}$ states. High rotational energies are expected near closed shells. However, the evidence is very meager for fruitful speculation. As produced by Ce^{137m} decay, these transitions are very weak for detailed study, and it is not certain to which low level in La^{137} the transitions occur.

(2) The Adjacent Pr Isotopes

The decay of 4.5-hour Pr^{139} produces no γ -rays, and its daughter activity exhibits the 166-kev γ -ray and 140-day half-life indicating decay to the Ce^{139} ground state. The ft value predicts an allowed transition. The ground state of

140-day Ce¹³⁹ has been established as a $d_{3/2}$ state (Ketelle, Thomas, and Brosi 1956). A 740-kev isomeric transition from a $h_{11/2}$ level in Ce¹³⁹ to the ground state was observed by these workers, with a half-life of 55 seconds. In the decay of Pr¹³⁹, a transition to this level would be energetically allowed, but no 740-kev radiation is observed, indicating that such a transition is highly forbidden. A $d_{5/2}$ ground state for Pr¹³⁹ is expected, as in the case of Pr¹³⁷, and is consistent with allowed decay to $d_{3/2}$ Ce¹³⁹. A transition to the $h_{11/2}$ state would be third forbidden. As in the Pr¹³⁷ case, the absence of parity changes makes the allowed assignment unambiguous. The $g_{7/2}$ level as a Pr¹³⁹ ground state is ruled out by the absence of decay to the isomeric state. Thus Pr¹³⁹ decays by an allowed $d_{5/2}$ to $d_{3/2}$ transition to the ground state of Ce¹³⁹.

Pr¹³⁸ decays to Ce¹³⁸, producing very intense γ -rays of 300 ± 5 , 800 ± 10 , and 1040 ± 10 kev. Less intense γ -rays of 1295 ± 15 and 1590 ± 20 also appear, and a weak transition of 160 kev. The ft value indicates an allowed decay. For an allowed transition and on a tentative assumption that the decay takes place predominantly to a single level in Ce¹³⁸, the observed K -capture to positron branching ratio gives a correct value for the nuclear energy difference, as obtained from the positron end-point energy. This agreement supports the assumption, and indicates the decay is mainly to a single excited level, or to closely spaced levels.

If the ground state of Pr¹³⁸ has its odd proton in the $d_{5/2}$ level and its odd neutron in the $d_{3/2}$ level, as in the neighboring odd A nuclei, this would give $J = 1$, and even parity for the ground state, by Nordheim's Strong Rule. But this favors an intense allowed transition to the $(0, +)$ ground state of stable Ce¹³⁸. The presence of intense high energy γ -rays plus the K -capture to positron branching ratio opposes this assumption. It seems probable that the ground state of Pr¹³⁸ has a high spin value and decays by an allowed transition to a high spin excited state, or states, in Ce¹³⁸. The beta-decay systematics of Way and Wood (1954) indicate a value of about $Q = 3.7$ Mev for Pr¹³⁸ to the ground state of Ce¹³⁸. This would favor the transitions predominantly to the vicinity of the 1.3-Mev level in Ce¹³⁸, which would be consistent with observations.

The 300-kev transition seems definitely to be of $E3$ character, which would indicate an isomeric state with half-life of the order of seconds. For the energy and Z involved, the K/L ratios vary widely with multipolarity, making the assignment seem unambiguous. The new calculations of the conversion coefficients by Sliv increase the K -conversion coefficient for the 300-kev transition by only about 10% above the Rose value, and the K/L ratio is not expected to change significantly. Thus the $E3$ assignment still stands.

Investigations of the decay of La¹³⁸ to Ce¹³⁸ (Turchinetz and Pringle 1956; Glover and Watt 1957) show an 810-kev $(2, +)$ level in Ce¹³⁸. The ground state of La¹³⁸ ($5, \pm$) has too low an energy to decay to the 1040 or higher energy levels of Ce¹³⁸ so that the results of these workers throw no light on the high energy levels. However, this indicates that the intense 300-kev transition,

and probably the weak 160-kev transition, are not fed from the 800-kev (2, +) level. Furthermore, it shows that if these transitions were from low-lying excited states rather than from cascade transitions between high energy levels, the decay of La¹³⁸ to these levels was highly forbidden on a spin basis, since the observed decay to the 800-kev level has a log *ft* = 19 (Glover and Watt 1957).

On a purely energy basis, the 300-kev transition could be a cascade from the 1590- to the 1295-kev level. The 1590- and 1295-levels could have cascade transitions through the 800-kev (2, +) level as well as directly to the ground state; since the resulting 790- and 495-kev transitions could be concealed in this investigation by the 800-kev level decay itself, and by the 511-kev annihilation radiation. However, the intense 1040-kev level appears to have a spin and parity such that it does not cascade to the 800-kev level, since no radiation of 240 kev was found. A further possibility would be a 300-kev (3, -) level fed by cascade from higher energy levels. For example, the 1295-kev transition could be a cascade from the 1590 level through the 300-kev level. The assumption of the 800-kev (2, +) level as the first excited state would be consistent with the systematics of energies of (2, +) first excited states of even nuclei, which indicate that about this energy is expected for Ce¹³⁸ (Scharff-Goldhaber 1953).

In summary, the evidence on the excited states of Ce¹³⁸ is too sketchy for proper organization. However, the existence for this even nucleus of an *E3* isomeric state seems fairly definite.

Pr¹³⁶

The value of "ft" for the decay of 1.0 ± 0.15 -hour Pr¹³⁶ indicates an allowed transition. As in the previous cases, only if the transition is allowed does the branching ratio give the correct value for the nuclear energy difference.

If Pr¹³⁶ has its odd proton and neutron in the same levels as in the neighboring odd *A* nuclei, Nordheim's Strong Rule predicts a ground state of *J* = 1, even parity. This would give allowed transitions to the (0, +) ground state of Ce¹³⁶, as well as to a (2, +) excited state.

The beta-decay energy predictions for even *A* nuclei of Way and Wood (1954) indicate a possible *Q* = 4 Mev for Pr¹³⁶ to the ground state of Ce¹³⁶. This would support decay to a level round 1100 in Ce¹³⁶. The systematics of the energies of 1st excited (2, +) levels of even even nuclei suggest about 900 kev in the case of Ce¹³⁶ (Scharff-Goldhaber 1953).

Unlike Pr¹³⁸, the Pr¹³⁶ spectra revealed no γ -rays or conversion electrons. However, the mass separated Pr¹³⁶ activity was weak, and the upper limits on the intensity of any unobserved γ -rays cannot rule out the possibility of high energy γ -rays of low intensity. Similarly high energy transitions of low intensity could produce conversion electron peaks too small to be observed in these experiments. However, the presence of low energy transitions can be ruled out, except for very low intensities.

Thus, in apparent contrast to Pr¹³⁸, the present evidence supports a low spin ground state for Pr¹³⁶, which decays predominantly to the ground state of Ce¹³⁶.

APPENDIX I

TARGETS, CHEMICAL SEPARATION, AND SOURCE PREPARATION

(a) Targets

For the production of praseodymium isotopes, targets of natural cerium were used in both oxide* and metallic forms. About 20 mg of the oxide was packed into an aluminum tube 3 mm in diameter \times 6 mm long made from 0.015 mm foil. This target was cooled through an intermediate dural clamp. Nevertheless, the cyclotron beam had to be reduced to 0.5 μ a to avoid the relatively insoluble oxide which forms at high temperatures. Alternatively, a bare piece of flattened metal from CCl_4 storage (to reduce oxidation) was mounted directly in one of the dural clamps. Following broadside bombardment at about 1 μ a, the front 1/16 in. was cut off and chemically separated.

For the production of Ce^{137m} , targets of natural lanthanum oxide were used. This material was handled in the same manner as the cerium oxide, but the bombardments were carried out at 1 μ a.

(b) The Chemical Separations

The chemical separations were based on the fact that cerium can be oxidized to a +4 valence state while lanthanum and praseodymium remain in the normal +3 valence.

(I) Cerium from Lanthanum Targets

The lanthanum metal or oxide was dissolved in concentrated nitric acid and after cooling in an ice bath, potassium bromate was added to oxidize the cerium to its +4 valence. After the addition of zirconium carrier, a saturated solution of potassium iodate was used to precipitate the cerium with the zirconium. After several purification cycles of dissolution and reprecipitation to remove the lanthanum, the cerium was reduced to the +3 valence state with hydrogen peroxide and the zirconium was removed as an iodate precipitate. The cerium was carried from the solution with ferric hydroxide. After washing and drying, this precipitate was dissolved in a few drops of 6*N* HCl and the iron was extracted with ethyl ether leaving the radioactive cerium in a small volume of acid solution.

(II) Praseodymium from Cerium Targets

The early praseodymium separations were carried out using a method in which the valence +4 cerium was precipitated as a phosphate (Dahlström, Foster, and Thompson 1958). However, after the development of the iodate separation for lanthanum targets, this was also adopted for praseodymium since the conditions seemed less critical for the iodate than for the phosphate precipitation.

The cerium oxide was dissolved by being heated in concentrated nitric acid and hydrogen peroxide. After dissolution the hydrogen peroxide was removed

*Cerium oxide was formed by heating ammonium hexanitrate cerate (G. F. Smith Chem. Co., Reference Purity) to about 250° C. The lanthanum oxide was the Spectroscopic Grade of Johnson and Matthey. Cerium and lanthanum samples of metal, each containing less than 10^{-4} parts of any other rare earth, were obtained from Ames Laboratory through the kindness of the Director, Dr. F. H. Spedding.

by repeated evaporation with nitric acid. Since the cerium metal was insoluble in nitric acid it was dissolved in a minimum volume of hydrochloric acid. Repeated evaporation with concentrated nitric acid removed the chlorine.

The cerium in ice-cold concentrated nitric acid was oxidized with potassium bromate and precipitated as the iodate by the addition of a saturated solution of potassium iodate. Zirconium carrier was added to the supernatant solution to remove any cerium which was not precipitated the first time. The praseodymium was removed from the iodate solution as a hydroxide, using iron carrier. The iron was removed from a small hydrochloric acid solution containing the praseodymium activity, which was then ready for the preparation of sources.

However, for mass spectrograph use, the praseodymium must be applied as a nitrate to the filament, and speed was essential, even at the cost of some loss of efficiency. When the iodate solution was rendered basic with ammonium hydroxide, the praseodymium was carried down by the ammonium iodate crystals themselves, from which it was separated by judicious washing. Complete removal of salts was ensured by dissolving in a drop of concentrated nitric acid and reprecipitating with ammonium hydroxide.

SOURCE PREPARATION

I. Mass Spectrograph

The filament electrode was placed horizontally beneath a heat lamp. When the filament was rather warm, a drop of acid solution containing the activity was carefully applied to the central region by a micropipette. This dried quickly and the source was then installed in the spectrograph.

II. Gamma Ray Spectrometers

A similar drop of active acid solution was applied to the surface of a thin teflon sheet or scotch tape. The drop was dried and then a protecting layer of scotch tape was placed over the source.

III. Slatis-Siegbahn β -Ray Spectrometer

These sources were commonly mounted on film 20 $\mu\text{g}/\text{cm}^2$ made from VYNS Resin obtained from the Chemistry Department. The films were very lightly gold-plated to ensure electrical grounding. The spot size was defined by a drop of insulin, later removed by washing. The active drop applied to this spot was dried with great care. On occasions, when speed was essential, the active drop was dried on a thin piece of niobium foil.

IV. 180° β -Spectrometer

A 30° trough 1/8 in. deep was cut across a 1/2 in. wide piece of teflon. Then a fast rotating cutter made a smooth sharp angled cut a few thousands of an inch deeper in the bottom of this trough. A 0.002 in. diameter tantalum wire, mounted in the source holder, was placed in this finer trough. The drop containing the activity is pipetted into the center of the trough. Owing to the non-wetting of the teflon, surface tension holds the drop at the center. After drying with a heat lamp about one-third of the activity remains on the wire surface and is confined to a short region.

APPENDIX II

THE MASS SEPARATIONS

The mass spectrograph was the same as that described in the previous paper except for alterations as described below.

Transmission

The horizontal focusing plate system was replaced by a radial lens which provided some direct control of the beam spread in the vertical plane. Machined teflon spacers ensured exact and reproducible alignment of lens components. To produce a line width at the collector equal to one-half the linear mass dispersion for praseodymium, viz. 0.020 in., required a beam-defining slit 0.015 in. wide. The transmission efficiency for the whole system was then about 15%. Owing, however, to the low electric fields at the hot filament surface and the consequent limitation on the emission of singly-charged ions of praseodymium oxide, the over-all efficiency was 1.5×10^{-3} .

Collection

Initially, the separated isotopes were collected on a plane copper or dural foil. By means of a contact print on X-ray film, the active isotopes were identified, cut out, and monitored.

This procedure gave positive identifications of mass numbers; but imperfect separations as learned from the γ -ray spectrometer. The main source of such imperfections was not the resolution of the instrument but either mechanical smearing of deposits during manipulations of the X-ray film or errors in cutting the foil in "total darkness", guided only by pin pricks. With little or no loss of activity, these troubles were avoided by a system described in the next paragraph.

In the central portion of the collector foil, the individual ribbon collectors were pre-cut along their sides with the known spacing of the linear mass dispersion, $d = 0.040$ in.; but through their uncut ends, these remained an integral part of the collector foil. This foil was insulated from its grounded front supporting frame by a 0.030-in. teflon washer. Thus the collection area was connected, as before, to the amplifier circuit which indicated the ion current it received. However, spot-welded to the grounded frame immediately in front was a grid of opaque vertical ribbons of width $0.4d$ and spacing, d . Each member of this grid was obviously centered in front of a corresponding slit in the collector foil. Thus by control of the accelerator voltage, the mass samples could be brought through the $0.6d$ openings in the grid to the center of pre-cut ribbon collectors. For convenience, this voltage was so selected that the stable Pr^{141} (which alone gave a detectable current) passed through the first opening. Continuous monitoring of the accelerator voltage kept the collector yield at a maximum. Thus the mass number for each collector strip was predetermined. Thereafter the pure samples of known masses were readily separated.

APPENDIX III

THE ABSOLUTE γ -RAY DISINTEGRATION RATES

To obtain the absolute disintegration rate for a particular γ -ray, the observed counting rate in the full energy peak was divided by an efficiency factor. Using sources of known strength, these efficiency factors for energies greater than 100 kev had been calculated as a function of distance from the crystal cover, (Bell and Skarsgard 1956). For energies below 100 kev, the applied efficiency factors were the computed total efficiencies of McGowan (1954) also using a 1.0 in. \times 1.5 in. diameter counter. At low energies these total efficiencies are approximately equal to the photoelectric efficiencies. However, the photoelectric effect produces both the full energy peak and the iodine escape peak, which is 28 kev lower in energy. For X-rays of about 33 kev this escape peak is too low in energy to be detected and this unknown part of the total intensity is lost.

To obtain an estimate of the correction required for the escape peak, a source of lanthanum X-rays (Ce^{139}) was sandwiched between two identical 1.5 in. \times 1 in. NaI (Tl) detector units placed end to end. The combined outputs were 15% greater than the sum of the two counter rates when separated, with the source in contact with each in turn. This indicated that 15% of the full energy peak intensity was escaping into the opposite crystal. This did not represent the entire escape peak, however, since some losses occur owing to geometry and absorption in the aluminum covers.

A similar experiment was performed with 57-kev tantalum X-rays where both the escape peak and the peak due to 28-kev iodine X-rays from the opposite detector were observed. This showed that 60% of the escaping iodine X-rays were detected in the opposite counter. Assuming that the efficiencies were about the same in both cases, 25% of the lanthanum X-rays were not represented in the full energy peak when the source was directly against the crystal cover.

With a single counter, the escape peak for tantalum X-rays was 22% of the full energy peak with the source set directly on the detector, and 16.5% at 3 cm. Assuming the efficiency corrections were about the same in both cases, this would indicate that about 19% of the lanthanum X-rays were not represented in the full energy peak with the source at 3 cm (a distance for which the efficiency factors are tabulated for the detector).

A further complication arose from the fact that while cerium and praseodymium K X-ray components were all above the iodine K -edge, all lanthanum components were not. The lanthanum $K\alpha_2$ component was below the iodine K -edge in energy, and thus it contributed nothing to the escape peak. The ratios of the intensities of the $K\alpha_1 : K\alpha_2 : K\beta$ are respectively about 2:1:1 (Richtmyer and Kennard 1947). Thus only 75% of the lanthanum X-rays contributed to the escape peak and the efficiencies at 3 cm were lowered by 25% for cerium and praseodymium and by 19% for lanthanum X-rays. The

limit of accuracy of the efficiency factors for γ -rays of energy greater than 100 kev was about 10%. For the X-rays, considering both the escape peak corrections and the fact that the calculated total counting efficiencies used might be somewhat large, the limit of error might be as high as 25%.

In addition to the above factors, the observed K X-ray intensity must be divided by the fluorescent yield to give the total intensity of K -shell events. While this factor is not due to the counting process itself, it is included at this point for completeness. For the X-rays of cerium and lanthanum the fluorescent yield is about 0.88 (Bergstrom 1955).

Studentships from the National Research Council were awarded to one of us (G.T.D.) for the period of the investigation.

REFERENCES

- BELL, R. E. and SKARGARD, H. M. 1956. Can. J. Phys. **34**, 745.
BERGSTROM, I. 1955. In Beta and gamma-ray spectroscopy. Edited by K. Siegbahn (North-Holland Pub. Co., Amsterdam), p. 630.
BROSI, A. R. and KETELLE, B. H. 1955. Phys. Rev. **100**, 169; 1956. **103**, 917.
BRYSK, H. and ROSE, M. E. 1955. Oak Ridge National Laboratory O.R.N.L.-1830.
CHUBBUCK, J. B. and PERLMAN, I. 1948. Phys. Rev. **74**, 982.
DAHLSTROM, C. E., FOSTER, J. S., and THOMPSON, A. L. 1958. Can. J. Phys. **36**, 1483.
FEENBERG, E. and TRIGG, G. 1950. Revs. Modern Phys. **22**, 399.
GLOVER, R. N. and WATT, D. E. 1957. Phil. Mag. **13**, 49.
GOEDHABER, M. and HILL, R. D. 1952. Revs. Modern Phys. **24**, 179.
HANDLEY, T. H. and OLSON, E. L. 1954. Phys. Rev. **96**, 1003.
HAYDEN, R. J. 1947. U. S. Atomic Energy Commission Document MDDC-1546.
HOLLANDER, J. M., PERLMAN, I., and SEABORG, G. T. 1953. Revs. Modern Phys. **25**, 469.
KELLER, H. R. and CORK, J. M. 1951. Phys. Rev. **84**, 1079.
KETELLE, B. H., THOMAS, H., and BROSI, A. R. 1956. Phys. Rev. **103**, 190.
MAYER, M. G. 1950. Phys. Rev. **78**, 16.
MCGOWAN, F. N. 1954. Phys. Rev. **93**, 163.
RICHTMYER, F. K. and KENNARD, E. H. 1947. Introduction to modern physics, 4th ed. (McGraw-Hill Book Co., Inc., New York).
ROSE, M. E. and GOERTZEL, G. H. (Siegbahn 1955, Appendix IV and later data).
SCHARFF-GOLDHABER, G. 1953. Phys. Rev. **90**, 587.
SIEGBAHN, K. (Editor) 1955. Beta and gamma-ray spectroscopy (North-Holland Pub. Co., Amsterdam).
TURCHINETZ, W. and PRINGLE, R. W. 1956. Phys. Rev. **103**, 1000.
WAY, K. and WOOD, M. 1954. Phys. Rev. **94**, 119.

THE STABILITY OF COUETTE FLOW IN AN AXIAL MAGNETIC FIELD¹

E. R. NIBLETT

ABSTRACT

Chandrasekhar's theory of the stability of viscous flow of an electrically conducting fluid between coaxial rotating cylinders with perfectly conducting walls is extended to include the case of non-conducting walls, and it is found that their effect is to reduce the critical Taylor numbers and increase the wavelength of the instability patterns by considerable amounts. An experiment designed to measure the values of magnetic field and rotation speed at the onset of instability in mercury between perspex cylinders is described. The radioactive isotopes Hg¹⁹⁷ and Hg²⁰³ were used to trace the flow. The results support the theoretical prediction that the boundary conditions can have a large effect on the motion.

INTRODUCTION

The problem of the stability of viscous flow between coaxial rotating cylinders (Couette flow) has been investigated by Taylor (1923), Lewis (1928), Meksyn (1946, *a, b, c*), and others. Taylor's work in this connection was the first successful correlation between theory and experiment in problems of hydrodynamic stability. Within the framework of certain approximations, he was able to define the conditions under which instability would occur, and also to predict the motion which would develop after its onset. Taylor's criterion for the onset of instability depends on the value of the dimensionless parameter

$$(1) \quad T = -\frac{4\Omega_0 A d^4}{\nu^2}$$

where

$$\Omega_0 = \frac{1}{2} \Omega_1 \left\{ (1+m) - \frac{3d}{4R_0} (1-m) \right\}, \quad A = \Omega_1 \frac{1-mR_2^2/R_1^2}{1-R_2^2/R_1^2},$$

ν is the kinematic viscosity, d the radial separation of the cylinders, Ω_1 the speed of the inner cylinder, m the ratio of the speeds of the two cylinders (Ω_2/Ω_1), R_1 and R_2 the radii of the inner and outer cylinders respectively, and $R_0 = \frac{1}{2}(R_1+R_2)$. T is called the Taylor number, and its critical value when the cylinders rotate in the same direction is 1708.

Chandrasekhar (1953) has studied the effect of an axial magnetic field on the stability of Couette flow when the fluid considered is an electrical conductor. The critical Taylor numbers were found to increase quite rapidly as the magnetic field increases, indicating that the effect of the field is to inhibit the onset of instability. The vortex compartments which appear at the transi-

¹Manuscript received June 27, 1958.

Contribution from the Division of Geomagnetism, Department of Mines and Technical Surveys, Dominion Observatory, Ottawa.

tion were found to be elongated in the direction of the field. The inhibiting effect of the field was expressed in terms of the Hartmann number

$$(2) \quad Q = \mu^2 H^2 d^2 \sigma / \rho \nu,$$

where μ is the permeability of the fluid, σ the conductivity, ρ the density, and H the intensity of the magnetic field.

The practical application of Chandrasekhar's theory is limited by his choice of boundary conditions which depend on the cylinder walls being perfectly conducting. In this paper the characteristic value problem is solved for the case of non-conducting walls, and some experiments are described in which mercury was used between cylinders made from perspex.

THEORY

(a) The Equations of Motion and Marginal Stability

The governing equations are the basic equations of magnetohydrodynamics for a homogeneous incompressible fluid. These are:

$$(3) \quad \frac{\partial \mathbf{v}}{\partial t} + (\mathbf{v} \cdot \text{grad})\mathbf{v} - \frac{\mu}{4\pi\rho} (\mathbf{H} \cdot \text{grad})\mathbf{H} = \nu \nabla^2 \mathbf{v} - \frac{1}{\rho} \text{grad} \left(p + \frac{\mu H^2}{8\pi} \right),$$

$$(4) \quad \frac{\partial \mathbf{H}}{\partial t} + (\mathbf{v} \cdot \text{grad})\mathbf{H} - (\mathbf{H} \cdot \text{grad})\mathbf{v} = \nu_m \nabla^2 \mathbf{H},$$

$$(5) \quad \text{div } \mathbf{v} = 0,$$

$$(6) \quad \text{div } \mathbf{H} = 0,$$

where \mathbf{v} is the fluid velocity, p is the pressure, and ν_m is the "magnetic viscosity" $1/4\pi\mu\sigma$. Electromagnetic quantities have been expressed in e.m.u.

The problem in hand differs from that solved by Chandrasekhar (1953) only in respect to the boundary conditions, and the formulation will not be repeated in detail. The perturbations of velocity and magnetic field intensity superimposed on the steady-state solutions of the foregoing equations are assumed to be of the form

$$(7) \quad \begin{aligned} v_r &= e^{\omega t} u(r) \cos \lambda z & h_r &= e^{\omega t} \phi(r) \sin \lambda z \\ v_\theta &= e^{\omega t} v(r) \cos \lambda z & h_\theta &= e^{\omega t} \psi(r) \sin \lambda z \\ v_z &= e^{\omega t} w(r) \sin \lambda z & h_z &= e^{\omega t} \chi(r) \cos \lambda z \end{aligned}$$

where $u, v, w, \phi, \psi, \chi$ are functions of r only. Here the variables are expressed in terms of the cylindrical polar co-ordinates (r, θ, z) and disturbances are assumed to be symmetrical about the z -axis and therefore independent of θ . For the case when the cylinders rotate in the same direction and their separation, d , is much less than the mean of their radii, R_0 , the equation of marginal stability derived by Chandrasekhar is

$$(8) \quad [(D^2 - a^2)^2 + Qa^2]^2 \psi = -Ta^2(D^2 - a^2)\psi.$$

This equation is valid provided $Q \ll \nu_m/\nu$. Radial distances from R_0 , and the wave number λ , have been expressed in dimensionless form by setting $(r - R_0)/d = \xi$ and $\lambda = a/d$. The symbol D stands for $d/d\xi$.

(b) *The Boundary Conditions*

Eight boundary conditions must be prescribed, four at each of the two cylindrical walls between which the fluid is contained. The assumption that there is no slipping of the fluid at the walls establishes the six conditions

$$(9) \quad [(D^2 - a^2)^2 + Qa^2]\psi = 0, \quad (D^2 - a^2)\psi = 0,$$

$$\text{and} \quad D[(D^2 - a^2)^2 + Qa^2]\psi = 0 \quad \text{at } \xi = \pm \frac{1}{2}.$$

The remaining pair of conditions must involve the magnetic field vector. When the cylinder walls are non-conducting no current can cross the boundaries, so that the radial component of current density must satisfy

$$j_r = (\text{curl } \mathbf{H})_r = 0 \quad \text{at } \xi = \pm \frac{1}{2},$$

i.e.

$$\frac{\partial h_0}{\partial z} = e^{\omega t}\psi \lambda \cos \lambda z = 0 \quad \text{at } \xi = \pm \frac{1}{2}.$$

We must, therefore, require that

$$(10) \quad \psi = 0 \quad \text{at } \xi = \pm \frac{1}{2}.$$

Equation (8), along with the boundary conditions (9) and (10), forms an eigenvalue problem for the parameters Q and T .

(c) *The Solution*

Chandrasekhar has frequently used the calculus of variations in order to circumvent the tremendous labor of solving high order linear equations with constant coefficients by conventional methods. To implement the variational procedure it is necessary to derive an integral expression for one of the parameters (in this case T) which yields a minimum value when the equation governing marginal stability is satisfied. For the cylinder problem with perfectly conducting walls Chandrasekhar (1953) proved that the expression

$$(11) \quad T = \frac{\int_{-1}^{+1} \{(D^2 - a^2)P\}^2 + Qa^2 P^2 d\xi}{a^2 \int_{-1}^{+1} P(D^2 - a^2)\psi d\xi}$$

can meet this requirement. Here

$$P = [(D^2 - a^2)^2 + Qa^2]\psi.$$

It can be verified that the same expression is valid for the case of non-conducting walls, when the boundary conditions are equivalent to

$$(12) \quad P = DP = (D^2 - a^2)\psi = \psi = 0 \quad \text{at } \xi = \pm \frac{1}{2}.$$

The problem thus differs from that of Chandrasekhar only in that the boundary conditions $\psi = 0$ (instead of $D\psi = 0$) will lead to different constants of integration.

Following Chandrasekhar (1953) we express DP and P in terms of a variational parameter \mathcal{A} , so that

$$(13) \quad DP = \frac{1}{2} \sin \pi \xi - \xi + \mathcal{A} \sin 2\pi \xi$$

and

$$(14) \quad P = \frac{1}{8} - \frac{1}{2}\xi^2 - \frac{1}{2\pi} \cos \pi \xi - \frac{\mathcal{A}}{2\pi} (1 + \cos 2\pi \xi),$$

both of which vanish at $\xi = \pm \frac{1}{2}$ in conformity with the boundary conditions. Then ψ must satisfy

$$(15) \quad [(D^2 - a^2)^2 + Qa^2]\psi = \frac{1}{8} - \frac{1}{2}\xi^2 - \frac{1}{2\pi} \cos \pi \xi - \frac{\mathcal{A}}{2\pi} (1 + \cos 2\pi \xi),$$

a solution of which is

$$(16) \quad \psi = \frac{1}{8}\gamma_0 - \frac{1}{2}\gamma_0(\xi^2 + 4a^2\gamma_0) - \frac{\gamma_1}{2\pi} \cos \pi \xi - \frac{\mathcal{A}}{2\pi} (\gamma_0 + \gamma_2 \cos 2\pi \xi) + B \cosh \beta_1 \xi + C \cosh \beta_2 \xi,$$

where

$$\gamma_n = [(n^2\pi^2 + a^2)^2 + Qa^2]^{-1}$$

$$\alpha_1 = \left\{ \frac{1}{2} \sqrt{a^4 + Qa^2 + \frac{1}{2}a^2} \right\}^{\frac{1}{2}}$$

$$\alpha_2 = \left\{ \frac{1}{2} \sqrt{a^4 + Qa^2 - \frac{1}{2}a^2} \right\}^{\frac{1}{2}}$$

$$\beta_1 = \alpha_1 + i\alpha_2 \quad \beta_2 = \alpha_1 - i\alpha_2$$

and B and C are constants of integration. The boundary conditions $\psi = 0$ at $\xi = \pm \frac{1}{2}$ lead to the relation

$$(17) \quad B \cosh \frac{\beta_1}{2} + C \cosh \frac{\beta_2}{2} = 2a^2\gamma_0^2 - \frac{\mathcal{A}}{2\pi} (\gamma_2 - \gamma_0),$$

while the conditions $(D^2 - a^2)\psi = 0$ at $\xi = \pm \frac{1}{2}$ lead to

$$(18) \quad B \cosh \frac{\beta_1}{2} - C \cosh \frac{\beta_2}{2} = \frac{-i}{a\sqrt{Q}} [\gamma_0 q + \frac{\mathcal{A}}{2\pi} (\gamma_2 c_2 - \gamma_0 c_0)].$$

Here $c_n = n^2\pi^2 + a^2$ and $q = (Q - a^2)/(Q + a^2)$.

From (17) and (18) we have

$$(19) \quad B = \left\{ a^2\gamma_0^2 - \frac{\mathcal{A}}{4\pi} (\gamma_2 - \gamma_0) - \frac{i}{2a\sqrt{Q}} [\gamma_0 q + \frac{\mathcal{A}}{2\pi} (\gamma_2 c_2 - \gamma_0 c_0)] \right\} \operatorname{sech} \frac{\beta_1}{2},$$

$$(20) \quad C = \left\{ a^2\gamma_0^2 - \frac{\mathcal{A}}{4\pi} (\gamma_2 - \gamma_0) + \frac{i}{2a\sqrt{Q}} [\gamma_0 q + \frac{\mathcal{A}}{2\pi} (\gamma_2 c_2 - \gamma_0 c_0)] \right\} \operatorname{sech} \frac{\beta_2}{2}.$$

Both numerator and denominator of the integral expression (11) can be written in terms of the variational parameter \mathcal{A} using (14), (16), (19), and (20).

The numerator of (11) is identical with that derived by Chandrasekhar which is

$$(21) \quad \int_{-\frac{1}{2}}^{+\frac{1}{2}} \{(D^2 - a^2)P\}^2 + Qa^2 P^2 d\xi = f + g\mathcal{A} + h\mathcal{A}^2$$

where

$$f = -\frac{1}{8}(a^2 + 8) \left\{ 1 + a^2 \left(\frac{2}{\pi^2} - \frac{1}{24} \right) \right\} + \frac{a^4}{320} + \frac{(\pi^2 + a^2)(\pi^4 + 3\pi^2 a^2 - 16a^4)}{8\pi^4} + Qa^2 \left(\frac{1}{120} + \frac{1}{8\pi^2} - \frac{2}{\pi^4} \right),$$

$$g = \frac{1}{\pi} \left[a^4 \left(\frac{1}{\pi^2} - \frac{1}{12} \right) + \frac{1}{12\pi^2} (4\pi^2 + a^2)^2 + \frac{Qa^2}{12} \left(\frac{13}{\pi^2} - 1 \right) \right],$$

and

$$h = \frac{1}{4\pi^2} \left[a^4 + \frac{1}{2}(4\pi^2 + a^2)^2 + \frac{3}{2} Qa^2 \right].$$

After integrating and arranging the terms, we find for the denominator

$$(22) \quad \int_{-\frac{1}{2}}^{+\frac{1}{2}} P(D^2 - a^2) \psi d\xi = l + m\mathcal{A} + n\mathcal{A}^2$$

where

$$l = \gamma_0 c_0 \left(\frac{1}{120} - \frac{1}{\pi^4} \right) + \gamma_0 q \left(\frac{1}{12} - \frac{1}{\pi^2} \right) + \gamma_1 c_1 \left(\frac{\pi^2 - 8}{8\pi^4} \right) + 2\gamma_0 \left\{ \frac{EG - FH}{J(E^2 + F^2)} \right\} - \pi^2 \gamma_0 \left\{ \frac{qK - 2a^3 \sqrt{Q}\gamma_0 L}{K^2 + L^2} \right\},$$

$$m = \frac{1}{2\pi} \left[\left(\frac{3}{4\pi^2} - \frac{1}{6} \right) \gamma_0 c_0 + \frac{4}{3\pi^2} \gamma_1 c_1 + \frac{1}{12\pi^2} \gamma_2 c_2 - \gamma_0 q + 2 \left\{ \frac{EM + FN}{J(E^2 + F^2)} \right\} - \pi^2 \left\{ \frac{(\gamma_2 c_2 - \gamma_0 c_0)K - a\sqrt{Q}(\gamma_2 - \gamma_0)L}{K^2 + L^2} \right\} + 8\pi^2 \gamma_0 \left\{ \frac{PG - RH}{J(P^2 + R^2)} \right\} \right],$$

$$n = \frac{1}{4\pi^2} \left[\gamma_0 c_0 + \frac{1}{2} \gamma_2 c_2 + 8\pi^2 \left\{ \frac{PM + RN}{J(P^2 + R^2)} \right\} \right],$$

$$E = \alpha_1(\alpha_1^2 - 3\alpha_2^2)$$

$$F = \alpha_2(\alpha_2^2 - 3\alpha_1^2)$$

$$G = q \sinh \alpha_1 - 2a^3 \sqrt{Q}\gamma_0 \sin \alpha_2$$

$$H = q \sin \alpha_2 + 2a^3 \sqrt{Q}\gamma_0 \sinh \alpha_1$$

$$J = \cosh \alpha_1 + \cos \alpha_2$$

$$K = (\alpha_1^2 - \alpha_2^2)^2 + \pi^2(\alpha_1^2 - \alpha_2^2) - 4\alpha_1^2 \alpha_2^2$$

$$L = 2\alpha_1 \alpha_2 (2\alpha_1^2 - 2\alpha_2^2 + \pi^2)$$

$$M = (\gamma_2 c_2 - \gamma_0 c_0) \sinh \alpha_1 + a\sqrt{Q}(\gamma_2 - \gamma_0) \sin \alpha_2$$

$$N = a\sqrt{Q}(\gamma_2 - \gamma_0) \sinh \alpha_1 - (\gamma_2 c_2 - \gamma_0 c_0) \sin \alpha_2$$

$$P = \alpha_1(\alpha_1^2 - 3\alpha_2^2 + 4\pi^2)$$

$$R = \alpha_2(\alpha_2^2 - 3\alpha_1^2 - 4\pi^2).$$

Thus (11) becomes

$$(23) \quad T = \frac{f+g\mathcal{A}+h\mathcal{A}^2}{a^2(l+m\mathcal{A}+n\mathcal{A}^2)}.$$

The value of \mathcal{A} for which T is a minimum is the root of the equation

$$(24) \quad \frac{dT}{d\mathcal{A}} = (gl-mf)+2(hl-fn)\mathcal{A}+(hm-gn)\mathcal{A}^2 = 0.$$

Critical Taylor numbers have been evaluated for seven values of Q ranging from zero to 6400. To do this T was calculated from (24) for each of a suitable series of values of a^2 . The minimum value of T , i.e. T_c , was found by plotting T as a function of a .

TABLE I

Critical Taylor numbers, and wave numbers of the modes which appear at the onset of instability for the case when the two cylinders rotate in the same sense and $d \ll R_0$

Q	a	T_c	T_c/T_0
0	$3.135 \pm .015^*$	1.708×10^3	1.000
9	$3.025 \pm .01$	2.311×10^3	1.353
36	$2.565 \pm .01$	4.489×10^3	2.628
100	$1.69 \pm .01$	1.082×10^4	6.335
400	$0.775 \pm .01$	4.273×10^4	25.02
1600	$0.39 \pm .01$	1.70×10^5	99.53
6400	$0.19 \pm .01$	6.85×10^5	398.4

*The limits indicate the accuracy to which the wave numbers could be determined graphically.

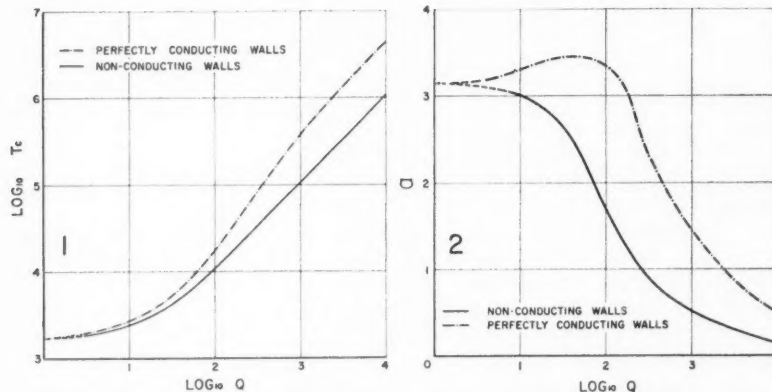


FIG. 1. Rotational instability curves. The critical Taylor numbers T_c as functions of Q for the cases of perfectly conducting and non-conducting cylinder walls.

Figure 2: A log-log plot showing the wave number a as a function of Q. The y-axis is labeled LOG a and ranges from 0 to 4. The x-axis is labeled LOG Q and ranges from 0 to 4. Two curves are shown: a solid line for non-conducting walls and a dashed line for perfectly conducting walls. Both curves start at approximately (0.5, 3.1) and decrease monotonically, with the non-conducting wall curve being consistently lower than the perfectly conducting wall curve.

The dimensionless wave number "a" is equivalent to $2\pi d/\text{wavelength}$. The value of a which corresponds to a critical Taylor number defines the wavelength of the mode which develops at the onset of instability. The values of the critical Taylor numbers and wave numbers are given in Table I and plotted as functions of Q in Figs. 1 and 2 respectively. Chandrasekhar's curves for perfectly conducting walls are shown for comparison. Since the two cases represent extreme conditions as far as the boundaries are concerned, it is reasonable to suppose that they provide upper and lower bounds to the general solution in which the boundaries have finite electrical conductivity. It must be remembered that these analyses are valid only when the separation of the cylinders is small compared to their mean radius, and when both rotate in the same direction.

As would be expected, the present analysis gives the same result ($T_c = 1708$) in the field-free case as was obtained by Chandrasekhar (1953) and Taylor (1923). It is seen in Figs. 1 and 2 that the effect of non-conducting walls is to reduce the critical Taylor number by a factor of nearly five when $Q = 10,000$, and to increase the wavelengths of the instability patterns by considerable amounts. A surprising feature of Chandrasekhar's analysis is that the wave number first increases with Q , the expected decrease not taking place till $Q > 50$. When the walls are non-conducting, however, the wave number decreases steadily as Q increases from zero.

EXPERIMENT

(a) The Magnetic Field

When the experiments were attempted, the solution of the previous section for non-conducting walls had not been worked out. However, it was evident from Chandrasekhar's theory that field intensities up to about 5000 oersted would be required to demonstrate the inhibition of instability in mercury between two cylinders of moderate dimensions. A large rectangular water-cooled solenoid was wound from heavy copper conductor to produce fields of this size. The finished coil consisted of five layers of windings, each layer having 23 turns. It was approximately 49 cm in length with an inside diameter of 15 cm and an outside diameter of $35\frac{1}{2}$ cm.

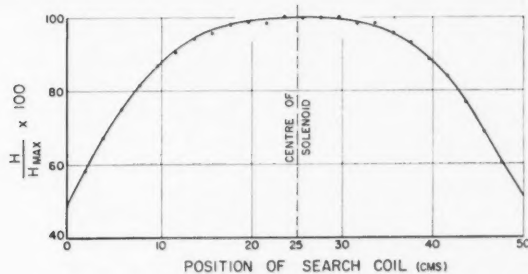


FIG. 3. Variation of magnetic field along the axis of the solenoid.

The solenoid was designed to operate from a d-c. motor-driven generator capable of delivering 2100 amperes at approximately 12 volts. The power output was continuously variable from zero up to the maximum of about 25,000 watts. The curve plotted in Fig. 3 shows the measured field variation along the axis of the coil. The field was reduced by only 4% at a distance of 10 cm on either side of the center, but fell off rapidly at greater distances.

(b) *The Cylinder Apparatus*

The inner and outer cylinders are shown separately and assembled in Fig. 4. Only the inner one was able to rotate. They were made from perspex to the following dimensions:

inner cylinder	
radius of central portion	1.740 cm,
radius of end portions	2.012 cm,
over-all length	40.6 cm,
length of central portion	22.0 cm,
outer cylinder	
internal radius	2.554 cm,
over-all length	43.2 cm,
annular space between the cylinders	
width of central portion	0.814 cm,
width of end portions	0.452 cm,
volume	376 cc.

The inner cylinder was made larger at its ends in an effort to counteract the effect of the reduced magnetic field at points remote from the center of the solenoid. While the effect of the reduced field was to enhance the onset of instability, that of the reduced gap was to delay it. Thus the cylinders were designed to prevent, as far as possible, the premature development of turbulence near the ends which might upset the laminar flow in the remainder of the fluid.

The cylinders were mounted on a dural base plate so that the assembly could be rigidly supported inside the solenoid. The heavy brass flywheel (Fig. 4) attached to the lower spindle of the inner cylinder served to stabilize the drive, and also to give the cylinder sufficient downward thrust to overcome the buoyancy force when the apparatus was filled with mercury. A small phonic motor bolted to the floor was connected to the flywheel shaft through a reduction gear and a flexible rubber coupling. The speed of the inner cylinder could be varied continuously from 5 to 50 r.p.m. by varying the frequency of the audio input signal to the motor.

(c) *The Radioactive Tracer*

Since all liquid metals are opaque, their motions are not easily traced by means of dyes or suspended particles. In this experiment the use of the radioactive isotopes Hg¹⁹⁷ and Hg²⁰⁸ in conjunction with a suitably placed geiger tube was attempted. Hg¹⁹⁷ has a half-life of 65 hours and emits gamma

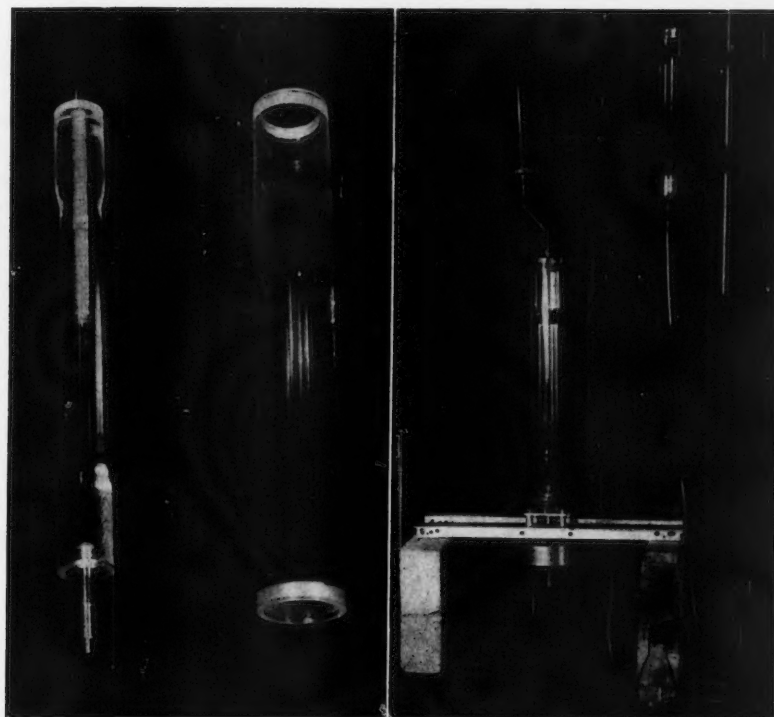


FIG. 4. The perspex cylinder apparatus.

radiation of 0.077 and 0.191 Mev, while Hg^{203} has a half-life of 48 days and emits a 0.279-Mev gamma ray. A small amount of these isotopes carefully introduced at the middle of the inner cylinder would be expected to remain adjacent to that cylinder as long as the motion was laminar. At the onset of instability, the development of a radial component of fluid velocity would cause some of the radioactive material to be carried across the annular space to the wall of the outer cylinder. Provided the radiation is efficiently absorbed by the intervening layer of mercury while the motion is laminar, the onset of instability would be accompanied by a large increase in the counting rate of a geiger tube mounted near the outer wall.

No data were located on the absorption coefficient of mercury for gamma rays in the required energy range (0.2 to 0.3 Mev). Radiation of this energy should obey approximately the absorption law

$$a = a_0 e^{-\frac{\mu}{\rho} d},$$

where a_0 is the initial radiation intensity, a is the intensity after absorption,

μ/ρ is the mass absorption coefficient in cm^2 per g, d is the thickness of the absorbing medium in g per cm^2 , and ρ is its density. The value of d required to reduce the intensity by a factor of two is

$$d_{\frac{1}{2}} = \frac{0.693}{\mu/\rho} \text{ g/cm}^2.$$

Rough experimental determinations of the absorption were made using Hg^{203} as the source, and ordinary mercury between the cylinders as the absorbing medium. The source was placed in a sealed specimen bottle which was lowered down the hole on the axis of the inner cylinder (Fig. 4). The activity was measured by means of a ring-shaped geiger tube which could be mounted about the outer cylinder. Counting rates were registered on a scaler when the absorbing layer was present and again when it was absent. The results of three such experiments, after allowance had been made for the background counting rate, are given below.

Experiment	a , counts/minute	a_0 , counts/minute	μ/ρ , cm^2/g	$d_{\frac{1}{2}}$, cm
1	84	10055	0.43	0.12
2	141	11059	0.39	0.13
3	97	12147	0.44	0.12

Since the layer of mercury between the cylinders was 0.8 cm thick, it was reasonable to suppose that the shielding would be sufficient to enable one to distinguish between laminar and unstable motion by the radioactive tracer method. Furthermore, in a fresh isotope mixture most of the activity arose from Hg^{197} , which emits a softer gamma ray than does Hg^{203} . The absorption by the perspex parts of the cylinder apparatus was tested and found to be negligible.

(d) The Experimental Procedure

The radioactive mercury, obtained from the Atomic Energy Research Establishment at Harwell, usually consisted of 2.4 millicuries of Hg^{203} and 120 millicuries of Hg^{197} mixed with the natural element. The mixture was dispensed with a micropipette capable of transferring measured volumes of $\frac{1}{4}$ to $\frac{1}{2}$ cc to an accuracy of about 1%.

The radioactive mercury was introduced through a glass capillary tube mounted in a hole drilled along the axis of the inner cylinder (Fig. 4). A small radial outlet was drilled from the outside of the cylinder to the bottom of the capillary housing. The capillary tube projected about 10 inches above the top of the cylinder, the bore at the upper end being enlarged to form a small funnel. A subsidiary wide-bore glass tube containing a tap was cemented in the upper cap of the cylinders (Fig. 4).

Mercury from an external reservoir was run into the apparatus very slowly to ensure that all the air would be forced through the outlets at the top. The mercury was allowed to rise till it filled the cylinders and the capillary tube

to the level of the bottom of the small funnel. The tap in the subsidiary tube was left open so that mercury rose in it to a slightly higher level. A measured volume of the isotope mixture was then transferred to the funnel so that it lay on top of the column of mercury. The original level was then restored so that the upper part of the capillary column consisted of the radioactive mixture. Then sufficient natural mercury was added to the funnel so that when the level was restored a second time the radioactive material was at the bottom of the capillary and ready to be injected through the radial duct into the fluid between the cylinders.

Power was supplied to the solenoid, and the field adjusted till its value near the middle of the cylinders was considered to be well above the critical value required to preserve laminar motion. After this had been done, the inner cylinder was set rotating at a speed which was held constant throughout the experiment. The geiger tube was positioned opposite the radial duct, and the counting rate was noted at this stage. The mercury levels were reduced at such a rate that flow in the glass columns was barely discernible. The isotopes were thus forced at low speed into the main body of mercury while the inner cylinder was rotating. Great care had to be taken to prevent the mixture from travelling across the annular space to the outer wall at the beginning. The field was then reduced to zero in steps of about 350 oersted, an interval of 30 seconds being permitted to elapse at each step during which the counting rate was noted on a rate meter. This procedure was called the "live run". Immediately after this series of observations the field was restored to its initial value and the process repeated for a "blank run" in which no further radioactive mercury was added. The purpose of the second run was to ensure that the variations in counting rate, at a time when the isotopes were more or less randomly mixed with the main body of mercury, were appreciably smaller than those which occurred during the live run. If this were not so, as sometimes happened, no significance could be attached to the live run, and the results were discarded.

Contaminated mercury which was drained from the apparatus was usually fit for use again after a week or two owing to the rapid decay of Hg^{197} . Moreover, after the isotopes had been thoroughly mixed with the rest of the fluid the background count was considerably reduced because of the high absorption coefficient of mercury.

(e) Experimental Results

Experiments in which a significant rise in the counting rate was observed during the live run were completed for five different speeds of the inner cylinder. The observations and relevant data in one of these experiments ($\Omega_1 = 11.9$ r.p.m.) are given in Table II, and the rate-meter deflections are plotted against magnetic field strength in Fig. 5. The data from all five experiments are too numerous to record. Different runs which were done at the same rotation speed are labelled A, B, etc. As the rate-meter readings indicate, the background count in most of the experiments was quite high. Many of the runs, especially the earlier ones, were unsuccessful and the high cost of mercury prohibited the use of uncontaminated fluid in every run. The background

TABLE II

OBSERVATIONS IN THE FIRST CYLINDER EXPERIMENT

$$\Omega_1 = 11.9 \text{ r.p.m.} = 1.246 \text{ radians/sec}$$

$$\text{Temperature} = 19^\circ \text{C}$$

$$T = 6.37 \times 10^8$$

$$Q = 4.439 \times 10^{-4} H_e^2$$

Field intensity, oersted	Rate-meter readings on live run, μa	Rate-meter readings on blank run, μa
Run A		
3640	15	19
3295	15	18
2770	20	19
2420	25	19
2080	30	19
1725	30	20
1380	25	21
1035	20	19
690	20	19
345	20	19
Run B		
3990	15	18
3640	14	18
3295	28	18
2770	31	18
2420	34	18
2080	30	18
1725	25	17
1380	20	16
1035	18	18
690	18	19
Run C		
3810	50	70
3470	50	73
3470	50	69
3370	70	70
2940	70	71
2600	75	71
2245	80	71
1900	85	68
1550	90	69
1210	80	69
960	75	70
520	75	71

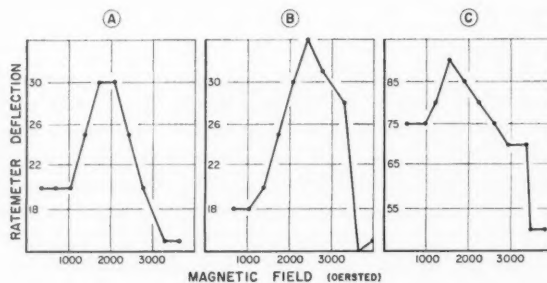


FIG. 5. Observations in the first experiment. $\Omega_1 = 11.9 \text{ r.p.m.}$ Rate-meter deflections plotted against magnetic field intensity.

count was measured with a scaler over several 1-minute intervals before an experiment was begun to make sure that it was constant. The time constant in the rate-meter tank circuit was about $2\frac{1}{2}$ seconds, so that the ammeter needle was not subject to rapid fluctuations. Whenever the rate meter indicated a significant change in counting rate at a given stage, the reading recorded was that which corresponded to the end of the 30-second period.

It was assumed that the critical magnetic field, H_c , was higher than the value at which an increase in the counting rate was first observed, but lower than that at the previous stage. The values of T_c , H_c , and Q estimated from the five experiments are given in Table III. The experimental results are plotted in Figs. 6 and 7 where they may be compared with the theoretical curves.

TABLE III
EXPERIMENTAL VALUES OF T_c , H_c , AND Q

Ω_1 , r.p.m.	T_c	H_c , oersted			Adopted H_{c1} , oersted	Q
		A	B	C		
11.9	6.37×10^6	3030	3470	3420	3420	5.19×10^3
17.9	1.44×10^6	2945	2695	2695	2780	3.43
22.7	2.30×10^6	3295	3210		3210	4.56
26.7	3.21×10^6	3640	3640	3640	3640	5.88
29.7	3.94×10^6	3985	3985		3985	7.03

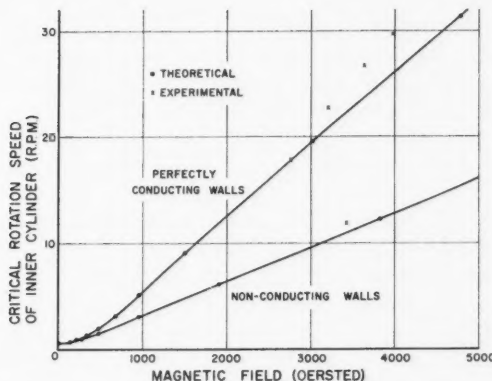


FIG. 6. Critical speeds of the inner cylinder plotted against magnetic field intensity.

(f) Discussion

While the experiments were in progress it was not realized that non-conducting walls could have such a large effect as is indicated by the theory of the preceding section. The theoretical curve for non-conducting walls plotted in Fig. 6 shows that the motion should have been unstable at the outset of all the experiments except that for which the speed of the inner

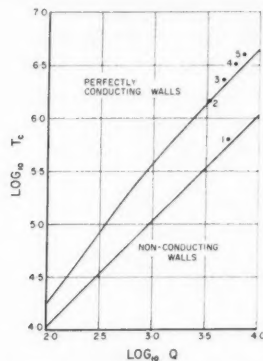


FIG. 7. Theoretical instability curves and experimental results.

1. $\Omega_1 = 11.9$ r.p.m. 2. $\Omega_1 = 17.9$ r.p.m.
 3. $\Omega_1 = 22.7$ r.p.m. 4. $\Omega_1 = 26.7$ r.p.m.
 5. $\Omega_1 = 29.7$ r.p.m.

cylinder was 11.9 r.p.m. The following table gives the initial field intensities in the experiments, and the approximate critical values based on the theories for perfectly conducting walls and non-conducting walls.

Experiment	Rotation speed, r.p.m.	Initial field, oersted			H_c , oersted	
		A	B	C	Conducting walls	Non-conducting walls
1	11.9	3640	3990	3810	1900	3710
2	17.9	3810	3740	3740	2775	5600
3	22.7	4160	4160		3500	7100
4	26.7	4850	4850	4850	4100	8500
5	29.7	4850	4850		4550	9500

At the onset of instability it was expected that cellular patterns would develop in a manner similar to that observed by Taylor (1923), i.e. the motion would be up and down near the wall of the inner cylinder, radially outwards at the cell boundaries, and down and up along the wall of the outer cylinder. At the outer wall the upward and downward streams would meet at the middle of a cell where a radially inward motion would develop to complete the pattern. The "wavelength" of a cell is the distance between two radially outward streams. Whereas this distance was found by Taylor to be very nearly equal to twice the separation of the cylinders in the field-free case, theory indicates that the cells are, in general, elongated when the motion is influenced by an axial magnetic field. The wavelengths of the cell patterns are plotted against critical rotation speed for the cases of perfectly conducting walls and non-conducting walls in Fig. 8. The curves apply only to cylinders having the same radial dimensions as those used in this series of experiments. The two curves meet when the critical speed is 0.615 r.p.m., corresponding to the field-free

case. It is seen that the wavelengths increase far more rapidly when the walls are non-conducting.

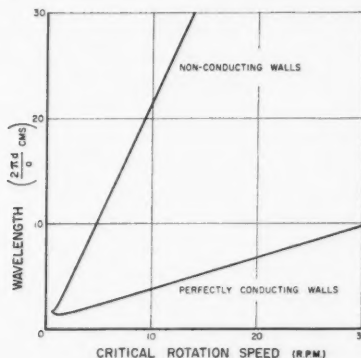


FIG. 8. Predicted wavelengths of the cell patterns at the onset of instability.

The fact that unstable motion was not detected at the outset of the last four experiments can be explained by the long wavelengths associated with the instability patterns. At rotation speeds of 17.9, 22.7, 26.7, and 29.7 r.p.m., the predicted wavelengths are 6, $7\frac{1}{2}$, 9, and 10 cm from Chandrasekhar's theory, and approximately 40, 49, 58, and 65 cm when the walls are non-conducting. Thus in these experiments the upward and downward flow along the inner cylinder would carry the isotopes into the region of the reduced gap, and right to the ends of the cylinders. Evidently the speed of flow at the start of the runs was too slow to permit the isotopes to travel this far in the 30 seconds during which the field was held constant. Whether or not the convection could develop properly is uncertain, because, except in the second experiment ($\Omega_1 = 17.9$ r.p.m.), there was not sufficient space to contain a single complete cell pattern. In the second the pattern may have formed, but the motion was certainly disturbed by end effects. The results indicate that some of the isotopes eventually reached the vicinity of the geiger tube by a round-about path, the average travel time in the four experiments being about two minutes.

The travel times (in seconds) observed in the last four experiments are outlined below:

Run	2nd expt.	3rd expt.	4th expt.	5th expt.
A	90-120	90-120	90-120	90-120
B	120-150	120-150	90-120	90-120
C	120-150		120-150	

While the observations do not allow very accurate determination of the times, it is clear that in all the runs attempted the interval between injection of the isotope and the increase in counting rate is close to two minutes. Since the

speed of transport should not have varied greatly from one experiment to the next, and since the path length was the same in each (about 40 cm), a constant travel-time is to be expected.

Thus the rise in counting rate observed in the last four experiments is attributed to a long travel-time of the isotopes, and not to the onset of instability at the corresponding value of the magnetic field. The fact that the results lay on a fairly smooth curve (Fig. 6), and did not depart by more than 15% from the critical fields estimated from Chandrasekhar's theory is now considered to be fortuitous. Different results would almost certainly have been obtained if different time intervals had been used between the stages, or if different initial fields had been applied.

The first experiment at 11.9 r.p.m. gave a result which was incompatible with the other four, and which lay close to the curve predicted for non-conducting walls (Figs. 6 and 7). At this speed the predicted wavelengths are 4.3 cm for perfectly conducting walls, and 25.7 cm for non-conducting walls. Thus a single cell pattern would, in theory, extend about 2 cm beyond each end of the central portion of the inner cylinder. It is a reasonable supposition that the elongated cell pattern did form during these runs, because in run A, when the motion should have been unstable from the start by a small margin, the increase in counting rate was not observed till 60–90 seconds after the injection of the isotopes. In both runs B and C, the motion should have been stable at the initial stage and unstable at the second. In B the increase in counting rate came 30–60 seconds after the beginning of the second stage, while in C it came 60–90 seconds afterward. In view of the reduced wavelength, the isotopes were transported at roughly the same velocity (0.3 cm/sec) as they were in the other experiments.

The first experiment supports the theory of the foregoing section. The adopted experimental value of the critical axial field was 3420 oersted whereas theory predicts $H_c = 3710$ oersted. Allowing for a time lag of about one minute between the onset of instability and the increase in counting rate, it can be inferred that H_c lay between 3900 and 3640 oersted in run B, and between 3810 and 3470 oersted in run C. The agreement is as good as can be expected from the technique employed, but the evidence is not conclusive. The data obtained in the first experiment do not, unfortunately, establish beyond all doubt that the motion was laminar at the start of runs B and C. However, at a rotation speed of 11.9 r.p.m. the critical field in the case of perfectly conducting walls is 1900 oersted. The experiment does, therefore, clearly indicate that when the cylinders are made from non-conducting material the onset of instability is much less inhibited by a magnetic field.

In Taylor's experiments, when the wavelengths were close to 2 cm, the time taken for the colored liquid to trace out a complete cell pattern was 2–3 seconds. Thus it was originally considered that a constant, or nearly constant, counting rate over the initial 30 seconds of a run would be conclusive evidence of stable motion. However, the sevenfold increase in wavelength of the instability patterns predicted by the theory for non-conducting walls makes this assumption invalid. In the first experiment, the initial field exceeded the

theoretical value of H_c by 280 oersted in run B, and by 100 oersted in run C. The margin was very small, and the observations should have started at higher fields and extended over time intervals of about $1\frac{1}{2}$ minutes to establish that the motion was initially stable.

When the discrepancies between theory and experiment were realized, it was no longer possible to run another series of experiments. The apparatus described herein would probably be satisfactory at rotation speeds of 10 r.p.m. or less if longer time intervals were allowed between reductions in the field. The use of longer cylinders and larger magnetic fields is indicated at higher speeds. Experiments would then be difficult because of the greatly increased requirement for d-c. power.

ACKNOWLEDGMENTS

The experimental work was done under the auspices of the Department of Geodesy and Geophysics at the University of Cambridge. I am greatly indebted to Dr. C. S. Beals and Mr. R. G. Madill of the Dominion Observatory (Department of Mines and Technical Surveys), who made it possible for me to attend the University, and to Mr. B. C. Browne, Dr. S. K. Runcorn, Sir Edward Bullard, and Sir Geoffrey Taylor of Cambridge for their valuable advice on many occasions. The problem was suggested by Dr. Runcorn.

The cylinders were built by Mr. L. Flavill of the Department of Geodesy and Geophysics, who also provided expert guidance on problems of mechanical design. Mr. K. Plachecki and Mr. Austin gave practical assistance on numerous occasions. Mr. Lamb of the Cavendish Laboratory constructed the geiger tube which was used in the experiments. Captain Hilkin of the Engineering Department (Cambridge) kindly provided me with space and power facilities in the Engineering Laboratory. Dr. J. A. Shercliff and Mr. W. Middleton were most helpful in giving advice on the construction of the magnet and in placing equipment at my disposal.

I should like to thank Mrs. Donald Eastwood, who did most of the laborious numerical work in the solution of the stability problem. Dr. C. S. Beals has kindly read the manuscript and suggested many improvements. I am grateful to Dr. K. Whitham and Dr. J. A. Rottenberg of the Observatory staff for several helpful discussions on the theory.

REFERENCES

- CHANDRASEKHAR, S. 1953. Proc. Roy. Soc. A, **216**, 293.
LEWIS, J. W. 1928. Proc. Roy. Soc. A, **117**, 388.
MEKSYN, D. 1946a. Proc. Roy. Soc. A, **187**, 115.
——— 1946b. Proc. Roy. Soc. A, **187**, 480.
——— 1946c. Proc. Roy. Soc. A, **187**, 492.
TAYLOR, G. I. 1923. Phil. Trans. A, **223**, 289.

ROTATIONAL ANALYSIS OF THE γ SYSTEM OF THE PO MOLECULE¹

K. SURYANARAYANA RAO²

ABSTRACT

The bands of the γ system of the PO molecule have been photographed under high dispersion (0.35 \AA/mm). A rotational analysis of the 0-0, 0-1, and 1-0 bands is given, which differs from the one previously given by Sen Gupta. In addition, four more bands, namely, the 1-2, 2-1, 2-3, and 2-4 bands, have been analyzed. The bands are attributed to the electronic transition, $A^2\Sigma-X^2\Pi_{\text{reg}}$, the lower state being the ground state of the molecule. The new rotational constants for the ground state are the following:

$$B_e = 0.7331 \text{ cm}^{-1}; \quad a_e = 0.0055 \text{ cm}^{-1}; \quad r_e = 1.473_0 \text{ \AA}; \quad A \sim 224 \text{ cm}^{-1}.$$

The spin doubling in the upper state is small. Perturbations in the $v = 0$ level of the upper state, which were not reported previously, are observed and discussed. They supply a welcome confirmation of the correctness of the analysis here presented.

INTRODUCTION

Two band systems of the PO molecule are known, the β system extending from 3200 to 3600 \AA and the γ system extending from 2800 to 2300 \AA . These bands have been described by Petrikahn (1928), Curry, Herzberg, and Herzberg (1933), Ghosh and Ball (1931), and Dressler (1955) and a rotational analysis of the γ system has been given by Sen Gupta (1935). Recent work by Singh (1957) on the β system has indirectly cast considerable doubt on this rotational analysis, and the present work was undertaken to check directly the analysis of the γ system. The 0-0, 0-1, 1-0, 1-2, 2-1, 2-3, and 2-4 bands have been photographed at high dispersion and analyzed. Aided by perturbations not previously found by Sen Gupta, the new analysis shows quite definitely that Gupta's analysis is incorrect. The constants of the upper and lower states have been determined from the new spectra.

EXPERIMENTAL

The spectrum was excited by a high frequency discharge in a tube through which helium containing a trace of oxygen and phosphorus vapor was pumped. A 100-watt, 2450-Mc/sec oscillator was used to produce the discharge and the spectra were photographed in the third order of a 10-meter concave grating spectrograph. Iron lines obtained from an iron hollow cathode discharge tube were used as wave-length standards. The error in the relative wave-numbers of the lines is estimated to be, in general, less than 0.03 cm^{-1} .

Under the conditions described, the 0-0 band of PO is extremely strong

¹Manuscript received August 13, 1958.
Contribution from the Division of Pure Physics, National Research Council, Ottawa, Canada.

Issued as N.R.C. No. 4929.

²National Research Council Postdoctorate Fellow; on leave from Karnatak University, Dharwar, India.

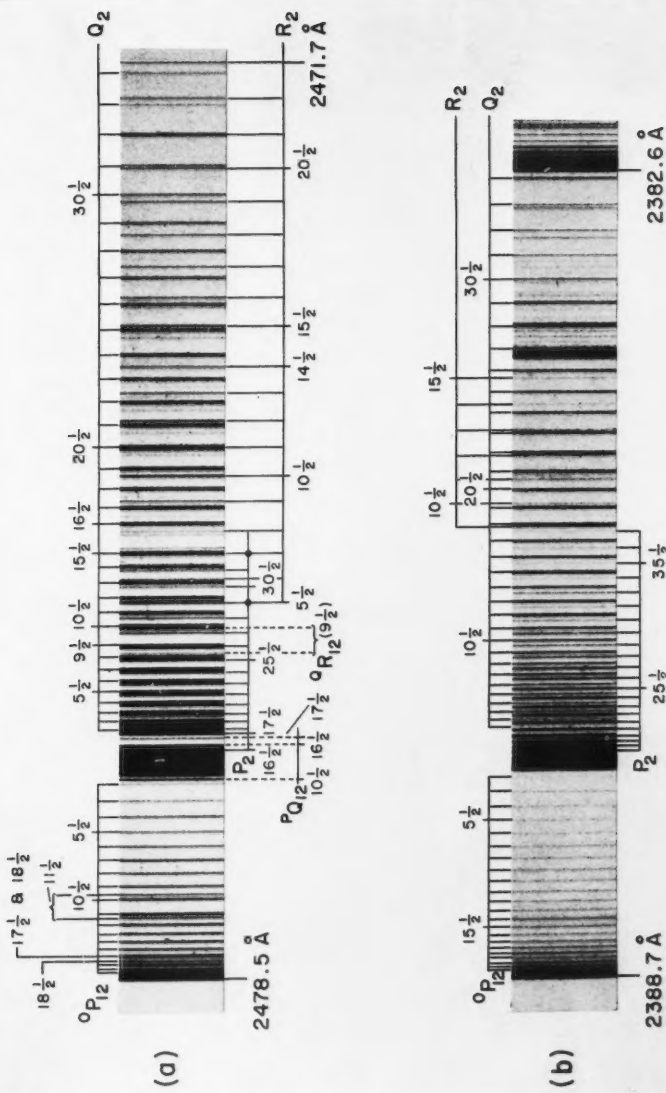
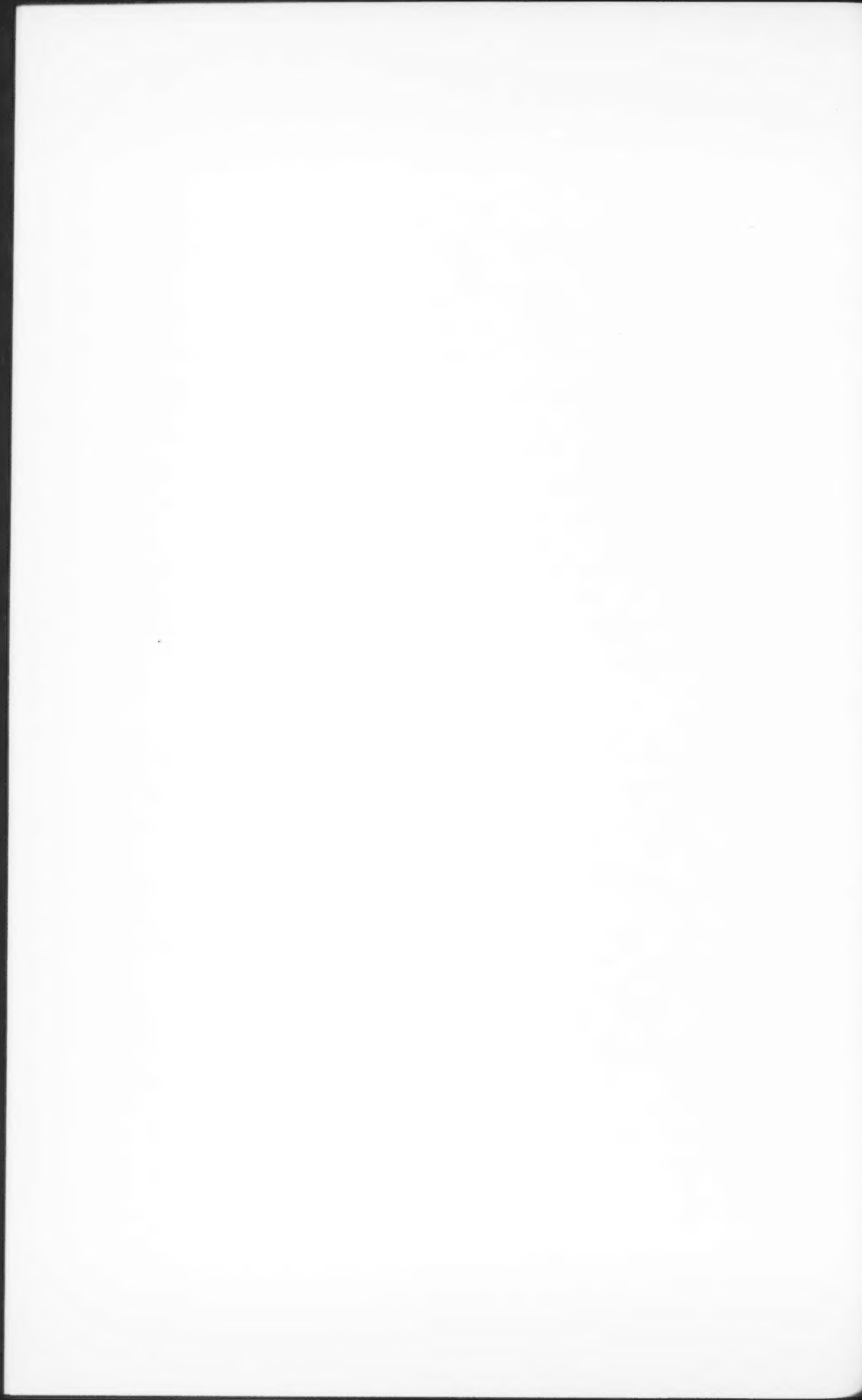


FIG. 1. Bands of the γ system of PO. (a) $0-0$ $^2\Sigma - ^2\Pi_{g/2}$ subband; (b) $2-1$ $^2\Sigma - ^2\Pi_{g/2}$ subband.



and could be photographed with very short exposures. One of the subbands ($^2\Sigma-^2\Pi_{3/2}$) of the 0-0 band and the corresponding subband of the 2-1 band are shown in Fig. 1. Bands involving higher vibrational quanta are weaker and overlap each other. Also, with long exposures, bands of P_2 , O_2^+ , and PN appear and become troublesome. As a result of this overlapping only a relatively small number of the bands could be analyzed and even in these bands (except 0-0) many lines are overlapped.

ANALYSIS AND DETERMINATION OF CONSTANTS

Each band consists of two subbands, with each subband showing two heads. Eight branches could be picked out in each band. Their J -numbering has been determined in the usual way. These features suggest that the electronic transition of the bands is $^2\Sigma-^2\Pi$. The nature of the electronic transition of these bands will be discussed in detail later. The number of expected branches for this transition is 12, six of them being the main branches P_1 , P_2 , Q_1 , Q_2 , R_1 , and R_2 and the other six being satellite ones, namely, ${}^oP_{12}$, ${}^sR_{21}$, ${}^pQ_{12}$, ${}^qR_{12}$, ${}^qP_{21}$, and ${}^RQ_{21}$. The analysis shows that the spin-doubling in the upper state $^2\Sigma$ is extremely small and in view of this, four of the expected satellite branches, ${}^pQ_{12}$, ${}^qR_{12}$, ${}^qP_{21}$, and ${}^RQ_{21}$ are superposed on the main branches. The wave-numbers of the identified lines of the seven bands are given in Table I.

TABLE I
WAVE NUMBERS (IN CM⁻¹) OF THE LINES IN THE γ BANDS ($A\ ^2\Sigma-X\ ^2\Pi_{reg}$) OF PO

J	$P_{12}(J)$	$P_2(J)$	$Q_2(J)$	$R_2(J)$	$P_1(J)$	$Q_1(J)$	$R_1(J)$	$R_{21}(J)$
0-0 band								
1½	40373.52					40596.08	40599.28	40603.50
2½	40370.04	73.08	40377.55		40592.55	95.62	600.34	06.55
3½	68.00	72.64	78.86		90.56	95.26	01.44	09.14
4½	66.03	72.27	80.03		88.66	94.86	02.66	11.92
5½	64.20	71.96	81.30	40392.12	86.86	94.50	03.96	14.71
6½	62.42	71.62	82.62	95.00	85.15	94.50	05.38	17.78
7½	60.74	71.62	84.04	98.02	83.57	94.50	06.84	20.77
8½	59.13	71.62	85.54	400.83	82.04	94.50	08.31	23.54
9½	57.60	71.62	86.91	04.52	80.59	94.50	{ 09.14	27.51
							{ 11.92	
10½	56.02	71.62	89.16	07.67	79.11	{ 93.71	12.63	30.71
						{ 96.56		
11½	{ 56.60	71.96	90.83	11.00	{ 79.85	95.62	14.30	34.11
	{ 53.71				{ 76.93			
12½	54.23	72.27	92.47	14.31	77.59	96.01	16.23	37.63
13½	40352.94	40372.64	40394.58	40417.74	40576.46	40596.49	40518.29	40641.18
14½	51.82	73.52	96.52	20.96	75.50	97.08	20.47	44.54
15½	50.84	73.75	98.25	25.94	74.65	97.83	22.66	49.66
16½	49.94	74.09	401.81	29.41	73.90	98.53	{ 25.19	53.30
							{ 25.85	
17½	49.08	76.23	03.78	33.20	73.17	{ 99.65	27.93	57.27
						{ 600.34		
18½	{ 49.08	76.23	06.12	37.14	{ 73.17	600.84	30.47	61.38
	{ 48.51				{ 72.58			
19½	48.04	76.67	08.59	41.18	72.58	01.96	33.12	65.61
20½	47.52	77.55	11.17	45.30	72.05	03.17	35.91	69.93
21½	47.08	78.58	13.86	49.33		04.50	38.82	74.18
22½	46.74	79.70	16.63	53.88		05.95	41.79	78.88
23½	46.45	80.93	19.52	58.28		07.50	44.90	83.57
24½	46.45	82.25	22.43	62.78		09.14	48.09	88.28

TABLE I (*continued*)WAVE NUMBERS (IN CM⁻¹) OF THE LINES IN THE γ BANDS ($A^2\Sigma-X^2\Pi_{\text{reg}}$) OF PO

<i>J</i>	$P_{12}(J)$	$P_2(J)$	$Q_2(J)$	$R_2(J)$	$P_1(J)$	$Q_1(J)$	$R_1(J)$	$R_{21}(J)$
25½	46.45	83.65	25.49	67.37		10.88	51.42	93.13
26½	46.45	85.17	28.61	72.07		12.68	54.82	98.22
27½	46.45	86.73	31.86	76.87		14.71	58.34	
28½		88.44	—			16.77	61.91	
29½		90.22	38.58			18.90	65.61	
30½		92.12	42.06			21.15	69.42	
31½		94.00	45.65			23.69	73.29	
32½		40396.08	40449.33			40626.00	40677.28	
33½			53.09			28.61	81.40	
34½			56.99			31.28	85.53	
35½			60.91			34.04	89.91	
36½			64.94				94.29	
37½							98.75	
38½							—	
39½								708.09
0-1 band								
2½	39149.72							
3½	47.77							
4½	45.85							
5½	44.07		39161.14		39366.90	39374.73	39382.72	39392.04
6½	42.36		62.55		65.38	74.73	85.54	97.91
7½	40.77		64.05		63.83	74.73	87.09	401.04
8½	39.25		65.63	39181.36	62.21	74.73	88.78	04.01
9½	37.80		67.15	84.78	61.08	74.73	{ 89.40	07.88
							92.04	
10½	39136.35		39169.47	39187.96	39359.72	{ 39374.29	39392.84	39411.30
						76.84		
11½	{ 36.89		71.29	91.43	{ 57.44	76.46	94.90	14.89
	34.18(bd)				60.17			
12½	34.84		73.27	94.95	58.46	76.84	96.89	18.39
13½	33.90		75.33	98.52	57.44	77.47	99.05	22.19
14½	32.72		77.42	201.90	56.44	78.26	401.60	—
15½	31.92	39154.85	79.35	07.06	55.93	79.14	03.71	31.01
16½	31.18	55.19	83.08	10.70	55.38	80.05	{ 06.31	34.77
							07.29	
17½	30.49	57.64	85.23	14.69	54.74	{ 81.40	09.62	38.68
						82.00		
18½	{ 30.89	58.31	87.78	18.84	{ 54.74	82.72	12.33	43.23
	30.02				55.38			
19½	30.02	—	90.47	23.19	54.74	84.07	14.89	47.67
20½	30.02	60.66	93.28	27.44		85.54	17.76	52.34
21½	29.28	62.03	96.20			87.09	21.07	
22½	29.28	63.50	99.21			88.78	24.15	
23½	29.28	65.08	202.33			90.53	27.96	
24½	29.28	66.77	05.55			92.47	31.15	
25½	30.02	68.54	08.91			94.48	34.77	
26½	30.02	70.42	12.32			96.65		
27½	30.49	72.41	15.89			98.88		
28½		39174.53	39219.50				39401.30	
29½		76.68						
30½		78.96						
1-0 band								
2½	41747.11						41977.31	
3½	45.09						78.60	
4½	43.07						79.73	
5½	41.22						80.97	
6½	39.53						82.33	
7½	37.44						83.76	
8½	36.03	41748.96					85.29	
9½	34.85	48.66					86.92	

TABLE I (continued)

WAVE NUMBERS (IN CM⁻¹) OF THE LINES IN THE γ BANDS ($A^2\Sigma-X^2\Pi_{\text{reg}}$) OF PO

<i>J</i>	$P_{12}(J)$	$P_2(J)$	$Q_2(J)$	$R_2(J)$	$P_1(J)$	$Q_1(J)$	$R_1(J)$	$R_{21}(J)$
10½	32.95	48.42	65.37	83.88	56.23			88.63
11½	31.56	48.42	67.04	87.11	54.91			90.42
12½	30.20	48.66	68.79	90.59	53.49	41972.11		92.28
13½	28.96	48.96	70.64	93.77	52.64	72.54		94.25
14½	27.79	49.36	72.54	97.28	51.52	73.05		96.30
15½	26.70	49.82	74.53	800.76	50.65	73.66		98.45
16½	41725.67	41750.34	41776.59	41804.39	41949.76	41974.36	42000.70	
17½	24.71	50.93	78.72	07.99	49.03	75.11		02.99
18½	23.86	51.61	80.93	11.85	48.32	75.98		05.41
19½	23.09	52.38	83.24	15.61	47.74	76.93		
20½	22.36	53.23	85.63	19.57	47.07	77.95		
21½	21.70	54.16	88.07	23.61		79.08		
22½		55.15	90.59	27.53		80.30		
23½		56.21	93.21	31.35		81.60		
24½		57.21	95.92	36.02		82.95		
25½		58.22	98.69	40.27		84.44		
26½		59.89	801.53	44.67		86.03		
27½		61.32	04.39	49.08		87.67		
28½		62.72	07.34			89.36		
29½						91.04		
30½						92.67		
31½						94.60		
32½						96.67		
1-2 band								
1½						39549.24		
2½						50.30		
3½			39328.55			51.41		
4½				29.79		52.74		
5½				31.09		54.09		
6½	39312.44			32.52		55.62		
7½	10.88			34.05		57.25		
8½	09.44			35.68		58.93		
9½	08.10	39321.95		37.40	39531.48	39545.28	60.76	
10½	06.82	22.25		39.23	30.30	45.70	62.71	
11½	05.67	22.64		41.15	29.39	46.17	64.80	
12½	04.63	23.12		43.19	28.35	46.78	66.89	
13½	03.65	23.71		45.30	—	47.50	69.16	
14½	02.78	24.39		47.54	26.80	48.32	71.56	
15½	02.04	25.18		49.88	26.22	49.24	74.01	
16½	01.38	26.06		52.28	25.71	50.30	76.62	
17½	00.86	27.06		54.74	25.32	51.41	79.33	
18½	00.39	28.13		57.44	24.96	52.74	82.13	
19½	39300.00	29329.33	39360.17		39554.09	39585.04		
20½		30.61	62.99			55.62	88.05	
21½		32.01	65.94			57.25	91.20	
22½		33.50	68.93			58.93	94.44	
23½		35.08	72.11			60.76	97.79	
24½		36.76				62.71	601.24	
25½		38.60				64.80	04.86	
26½		40.45				66.89	08.50	
27½		42.44				68.99	12.30	
28½						71.29		
29½						73.78		
2-1 band								
1½			41896.80					
2½	41890.12		97.77					
3½	88.04		98.80					
4½	86.12		99.93				42121.67	
5½	84.26		901.12				22.82	
6½	82.47		02.40		42105.48		24.08 42132.00	
							25.43	34.68

TABLE I (*continued*)
WAVE NUMBERS (IN CM⁻¹) OF THE LINES IN THE γ BANDS ($A^2\Sigma-X^2\Pi_{\text{reg}}$) OF PO

<i>J</i>	$P_{12}(J)$	$P_2(J)$	$Q_2(J)$	$R_2(J)$	$P_1(J)$	$Q_1(J)$	$R_1(J)$	$R_{21}(J)$
7 $\frac{1}{2}$	41880.76		41903.75		42103.86		42126.88	42137.61
8 $\frac{1}{2}$	79.12		05.18		02.18		28.38	43.70
9 $\frac{1}{2}$	77.57		06.70	41923.61	00.85		29.99	46.79
10 $\frac{1}{2}$	76.10		08.29	26.65	09.49	42114.65	31.67	50.02
11 $\frac{1}{2}$	74.68		09.95	29.88	98.23	14.96	33.48	53.30
12 $\frac{1}{2}$	73.38	41891.73	11.71	33.20	97.04	15.33	35.35	56.67
13 $\frac{1}{2}$	72.15	92.03	13.54	36.53	95.89	15.79	37.31	60.24
14 $\frac{1}{2}$	71.00	92.43	15.45	39.96	94.93	16.29	39.37	63.79
15 $\frac{1}{2}$	69.93	92.91	17.46	43.48	94.00	16.89	41.49	67.49
16 $\frac{1}{2}$	68.91	93.41	19.49		93.15	17.56	43.72	71.18
17 $\frac{1}{2}$	67.96	94.05	21.64		92.64	18.36	46.05	
18 $\frac{1}{2}$	67.18	94.75	23.85			19.23	48.46	
19 $\frac{1}{2}$	66.42	95.57	26.15			—	50.94	
20 $\frac{1}{2}$	65.83	96.36	28.53			21.24	53.51	
21 $\frac{1}{2}$	65.12	97.31	30.99			22.37	56.23	
22 $\frac{1}{2}$	64.62	98.31	33.54			23.59	58.94	
23 $\frac{1}{2}$	64.18	99.40	35.74			24.91	61.79	
24 $\frac{1}{2}$	63.81	900.58	38.83			26.32	64.73	
25 $\frac{1}{2}$	63.48	01.81	41.61			27.80	67.74	
26 $\frac{1}{2}$	63.27	03.14	44.46			29.36	70.84	
27 $\frac{1}{2}$		41904.56	41947.38			42131.04	42174.06	
28 $\frac{1}{2}$		06.04	50.41			32.80	77.34	
29 $\frac{1}{2}$		07.60	53.49			34.68	80.71	
30 $\frac{1}{2}$		09.22	56.64			36.57	84.17	
31 $\frac{1}{2}$		10.96	59.90			38.61		
32 $\frac{1}{2}$		12.76	63.22			40.67		
33 $\frac{1}{2}$		14.64	66.62			42.91		
34 $\frac{1}{2}$		16.61	70.15			45.18		
35 $\frac{1}{2}$		18.65				47.54		
36 $\frac{1}{2}$		20.74				50.02		
37 $\frac{1}{2}$		22.94				52.53		
38 $\frac{1}{2}$		25.14				55.08		
2-3 band								
5 $\frac{1}{2}$	39483.46		39500.28					
6 $\frac{1}{2}$	81.82		01.78		39705.15		39725.07	
7 $\frac{1}{2}$	80.30		03.29		03.70		26.66	
8 $\frac{1}{2}$	78.86		04.91		02.26		28.38	
9 $\frac{1}{2}$	77.51		06.63	39523.59	00.96	39714.75	30.20	
10 $\frac{1}{2}$	39476.26	39491.60	39508.47	39526.80	39699.87	39715.15	39732.13	
11 $\frac{1}{2}$	75.13	92.01	10.39	30.30	98.81	15.65	34.18	
12 $\frac{1}{2}$	74.09	92.50	12.41	33.89	97.95	16.27	36.31	
13 $\frac{1}{2}$	73.15	93.07	14.52	37.54	97.11	16.98	38.57	
14 $\frac{1}{2}$	72.30	93.76	16.76	41.32	96.42	17.81	40.94	
15 $\frac{1}{2}$	71.60	94.57	19.09		95.83	18.74	43.38	
16 $\frac{1}{2}$	70.94	95.46	21.51		95.50	19.82	45.99	
17 $\frac{1}{2}$	70.37	96.47	24.04		95.30	20.95	48.68	
18 $\frac{1}{2}$	69.96	97.56	26.66			22.21	51.67	
19 $\frac{1}{2}$	69.58	98.73	29.39			23.54	54.48	
20 $\frac{1}{2}$	69.58	500.08	32.23			25.07	57.43	
21 $\frac{1}{2}$	69.32	01.48	35.16			26.66	60.53	
22 $\frac{1}{2}$		02.98	38.19			28.38	63.82	
23 $\frac{1}{2}$		04.59	41.32			30.20	67.14	
24 $\frac{1}{2}$		06.30				32.13	70.62	
25 $\frac{1}{2}$		08.12				34.18	74.16	
26 $\frac{1}{2}$		10.02				36.31	77.85	
27 $\frac{1}{2}$		12.04				38.57	81.68	
28 $\frac{1}{2}$		14.12				40.94	85.56	
29 $\frac{1}{2}$		16.36				43.38	89.56	
30 $\frac{1}{2}$		39518.67				39745.99	39793.69	
31 $\frac{1}{2}$		—				48.68	97.94	
32 $\frac{1}{2}$		23.59				51.57	802.28	

TABLE I (*concluded*)WAVE NUMBERS (IN CM⁻¹) OF THE LINES IN THE γ BANDS ($A^2\Sigma-X^2\Pi_{reg}$) OF PO

<i>J</i>	$P_{12}(J)$	$P_2(J)$	$Q_2(J)$	$R_2(J)$	$P_1(J)$	$Q_1(J)$	$R_1(J)$	$R_{21}(J)$
33½						54.58		
34½						57.43		
35½						60.53		
2-4 band								
3½		38317.10				38540.25		
4½		18.36				41.57		
5½		—				43.00		
6½	38301.32		21.22		38524.73		44.57	
7½	299.84		22.81		23.27		46.24	38560.01
8½	98.48	38310.65	24.53		21.97	38534.15	48.05	—
9½	97.24	11.02	26.36		20.86	34.56	49.97	66.77
10½	96.11	11.42	28.30		19.97	35.05	52.00	70.19
11½	95.10	11.95	30.36		19.07	35.69	54.19	73.98
12½	94.19	12.59	32.49		18.19	36.43	56.43	77.79
13½	93.40	13.34	34.77		17.52	37.31	58.84	81.72
14½	92.73	14.19	37.16		—	38.27	—	85.43
15½	38392.17	38315.16	38339.65		38516.53	38539.42	38563.99	38589.98
16½	91.71	16.23	42.28		16.04	40.62	66.77	94.35
17½	91.32	17.44	45.00			41.97	69.49	98.68
18½	91.16	18.73	47.81			43.46	72.66	603.17
19½	91.16	—	50.76			45.20	75.79	
20½	91.16	21.68	53.85			46.77	79.04	
21½		23.31	56.99			48.58	82.41	
22½		25.06	60.28			50.55	85.87	
23½		26.94	63.68			52.61	89.51	
24½		28.89				54.81	93.25	
25½		30.99				57.13	97.09	
26½		33.21				59.60	601.07	
27½		35.50				—	05.15	
28½		37.94				64.83	09.38	
29½		40.50				67.63		
30½		43.16				70.54		
31½						73.63		
32½						76.78		
33½						80.05		
34½						38583.46		
35½						87.01		
36½						90.64		
37½						94.35		
38½						98.18		

The following are the wave-numbers of the satellite branch lines in the 0-0 band separated from the main branch ones

<i>J</i>	$P_{Q12}(J)$	<i>J</i>	$Q_{R12}(J)$	<i>J</i>	$Q_{P21}(J)$	<i>J</i>	$Q_{R21}(J)$
10½	40375.57 }	8½	40385.26	14½	40596.95	8½	40608.49
	73.52 }						
16½	74.68	9½	85.97 }	15½	97.61	9½	09.93
			88.87 }			10½	12.34
17½	75.56 }	10½	89.36				
	76.23 }						
		11½	90.83				
		12½	92.67				
		13½	94.78				
		14½	96.80				
		15½	98.84				
		16½	401.18				

The rotational constant, B_0 of the $v = 0$ level of the lower state has been determined from combination differences by plotting the mean value of $\Delta_2 F_1(J)$ and $\Delta_2 F_2(J)$ divided by $(J + \frac{1}{2})$ against $(J + \frac{1}{2})^2$. The B values of the other vibrational levels in the lower and the upper states have been determined from B''_v and from the values $\Delta B (= B' - B'')$ of the bands obtained from their Q branches according to the equation given below for the determination of the band origins. Thus, using the values of B''_v determined as indicated above, the B'_0 and B'_1 values have been determined from $(B'_0 - B''_0)$ of the 0-0 band and $(B'_1 - B''_0)$ of the 1-0 band respectively. Using the B'_0 thus determined, the B''_1 has been obtained from $(B'_0 - B''_1)$ of the 0-1 band. Similarly all the other B values have been obtained. This method has been used as it makes it possible to get a higher relative accuracy of the B values and as also some of the bands are not developed well enough to give a sufficient number of combination differences for a direct determination of the B values.

The origins of the bands have been obtained by using the relation $Q_1(J) + Q_2(J) = 2\nu_0 + 2B''_v + 2(B'_v - B''_v)(J + \frac{1}{2})^2$. Plotting $Q_1(J) + Q_2(J)$ against $(J + \frac{1}{2})^2$ yields a straight line whose intercept with the ordinate axis gives $2\nu_0 + 2B''_v$.

The spin-doubling in the lower state, ${}^2\Pi$, has been evaluated from the relation

$$F''_2(J) - F''_1(J) = B''_v[4(J + \frac{1}{2})^2 + Y(Y-4)]^{\frac{1}{2}} \dots$$

where $Y = A/B_v$. Experimental values of $F''_2(J) - F''_1(J)$ can be found from $P_1(J) - {}^0P_{12}(J)$ and ${}^8R_{21}(J) - R_2(J)$. By plotting $\{[F''_2(J) - F''_1(J)]/B''_v\}^2$ against $(J + \frac{1}{2})^2$, a straight line is obtained whose intercept on the ordinate axis gives $Y(Y-4)$.

As the transition is ${}^2\Sigma - {}^2\Pi$, the Λ -type doubling of the lower state, ${}^2\Pi$, produces no doubling of the rotational lines but only a combination defect, that is, the difference between $\{R(J) - Q(J)\}$ and $\{Q(J+1) - P(J+1)\}$. The magnitude of the combination defect in each band is comparatively large in one of the subbands while it is very small in the other. Since in a ${}^2\Pi$ state the Λ -type doubling is larger in the ${}^2\Pi_{1/2}$ than in the ${}^2\Pi_{3/2}$ component for low J values, the subband in which the combination defect is larger has to be associated with the ${}^2\Sigma - {}^2\Pi_{1/2}$, and the other, with the ${}^2\Sigma - {}^2\Pi_{3/2}$. In a ${}^2\Pi_{1/2}$ state the Λ -type doubling is, according to Mulliken and Christy (1931),

$$\Delta\nu_{dc} = \pm p(J+1/2)$$

where the $+$ is to be taken when A is negative and the $-$ is to be taken when A is positive. From the observed branches,

$$\Delta\nu_{dc} = \frac{1}{2}[\{R_1(J) - Q_1(J)\} - \{Q_1(J+1) - P_1(J+1)\}]$$

Since the Λ -type doubling varies very little with the vibrational quantum number, the experimental values of $\Delta\nu_{dc}$ of all the bands have been plotted on the same graph, against $(J + \frac{1}{2})$. The slope of this straight line gives the value of p .

The spin-doubling in the upper state, ${}^2\Sigma$, could not be determined as the resolution is not adequate.

All the molecular constants determined as indicated above are given in Tables II, III, and IV.

TABLE II

Molecular constant (cm^{-1})	Lower state ($X\ ^2\Pi_{\text{reg}}$)	Upper state ($A\ ^2\Sigma$)
B_0	0.7303	0.7775
B_1	0.7248	0.7719
B_2	0.7192	0.7666
B_3	0.7140	—
B_4	0.7084	—
A_0	224.03	—
A_1	224.22	—
A_2	224.33	—
A_3	224.48	—
A_4	224.53	—
	0.0073 (${}^2\Pi_{\frac{1}{2}}$)	—

TABLE III

		Band origins ν_0 (in cm^{-1})				
v'	v''	0	1	2	3	4
0	0	40485.54	39265.35			
1	1	41862.71		39435.35		
2	2		42005.73		39604.73	38423.93

TABLE IV

State	T_e (cm^{-1})	ω_e	$\omega_e x_e$	B_e	a_e	r_e (\AA)
$A\ ^2\Sigma$	40406.77	1391.16	6.99	0.7801	0.0054	1.431 ₂
$X\ ^2\Pi_{\text{reg}}$	0	1233.42	6.57	0.7331	0.0055	1.473 ₀

DISCUSSION

The fact that there is a measurable combination defect proves that the transition is either ${}^2\Pi \rightarrow {}^2\Sigma$ or ${}^2\Sigma \rightarrow {}^2\Pi$. But analysis shows that the doublet-splitting in the lower state is large (224 cm^{-1}) and that it is negligibly small in the upper state. Thus we must conclude, in agreement with previous investigations, that the bands arise from a ${}^2\Sigma-{}^2\Pi$ transition. Since the ${}^2\Sigma-{}^2\Pi$ subband lies to the shorter wave-length side of the ${}^2\Sigma-{}^2\Pi_{3/2}$, the lower state ${}^2\Pi$ is regular. Thus the bands are due to $A\ ^2\Sigma-X\ ^2\Pi_{\text{reg}}$ transition, where the lower state ${}^2\Pi_{\text{reg}}$ is the ground state of the molecule.

In NO the two lowest excited states are the $A\ ^2\Sigma^+$ state at 43966 cm^{-1} and the $B\ ^2\Pi$ state at 45918 cm^{-1} and transitions from these to the ground state give rise to the γ - and β -band systems respectively. In PO the two known excited states are at 30846 cm^{-1} and 40808 cm^{-1} . The recent work by Singh has shown that the upper state of the β bands is a ${}^2\Sigma$ state. The present work has confirmed the fact that the upper state of the γ system is also a ${}^2\Sigma$ state. Furthermore a comparison of the combination defects in the two band systems

shows that both Σ states have the same symmetry and presumably are both Σ^+ states. The two known excited states of PO therefore do not correspond to the $A\ ^2\Sigma$ and $B\ ^2\Pi$ states of NO but it is possible that they do correspond to the $A\ ^2\Sigma$ and $D\ ^2\Sigma$ states of NO.

The F_2 levels of the $v = 0$ vibrational level of the upper state $A\ ^2\Sigma$ of the γ bands are perturbed at $J = 9\frac{1}{2}$ and $15\frac{1}{2}$. The F_1 levels are perturbed at $J = 10\frac{1}{2}$ and $17\frac{1}{2}$. These perturbations consist in an abrupt increase in the separation of successive members of the branches and in the appearance of extra lines. They can be clearly seen in the spectrogram reproduced in Fig. 1 (a) of the $^2\Sigma-^2\Pi_{3/2}$ subband of the 0-0 band by comparing with Fig. 1 (b), which is a reproduction of the unperturbed $^2\Sigma-^2\Pi_{3/2}$ subband of the 2-1 band. Where the perturbations occur, the satellite lines are separated from the lines of the main branches. Similar perturbations are observed in the 0-1 band. In Fig. 2(a) and 2(b) are plotted the differences between the observed and the calculated term-values for the two component levels $F_1(J)$ and $F_2(J)$, of the

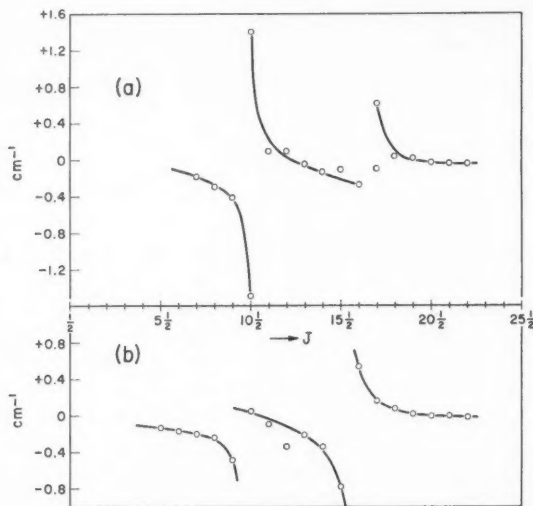


FIG. 2. Perturbations in the $v = 0$ level of the $A\ ^2\Sigma$ state of PO. (a) F_1 levels; (b) F_2 levels.

$v = 0$ level in the $^2\Sigma$ state. It has not been possible from the observed perturbations to determine the nature of the perturbing state. But it may be remarked that, on calculation, it has been found that in the $v = 9$ level of the upper state of the β bands almost at the positions of perturbations, there are rotational levels close in energy to the corresponding levels in the $v = 0$ level of the upper state $A\ ^2\Sigma$ of γ bands. This suggests that the observed perturbations might be due to the upper state of the β system. If this were a $^2\Pi$ state it might be possible to account for all the perturbations observed, two in the F_1 and two in the F_2 levels. But Singh's analysis of the β bands

shows that their upper state is a $^2\Sigma$ state and not a $^2\Pi$ state. In a mutual perturbation of two $^2\Sigma$ states, it is not possible, because of the selection rules, that each component level can be perturbed at more than one J value, as has been found here. It is possible, however, that some of the perturbations are due to the upper state of the β system and the others to another state.

The ground state, $^2\Pi$ of the molecule is separated from the perturbed state by about 41,000 cm $^{-1}$. It is unlikely that the ground state causes the perturbations since the dissociation energy of the molecule in the ground state is about 44,000 cm $^{-1}$. Further, it is found that the shift in energy caused by the perturbations goes back to zero at higher J values. Thus it does not seem very likely that the observed perturbations can be heterogeneous in character. The possibility of a quartet state ($^4\Sigma$) as the perturbing state cannot be ruled out, since such an intercombination perturbation would give rise to perturbations similar to those observed.

The rotational constants derived for the ground state $X\ ^2\Pi_{\text{reg}}$ in the present analysis agree fairly well with the preliminary values obtained by Singh from his analysis of the β system of bands but not with those given by Sen Gupta. Further, the perturbations observed in the $v = 0$ level of the upper state give an unambiguous numbering of the lines. Moreover, many wave-numbers of the individual lines given by Sen Gupta do not agree with those in the present investigation. Therefore it appears that the analysis given by Sen Gupta is incorrect.

ACKNOWLEDGMENTS

The author is deeply indebted to Dr. A. E. Douglas for his kind, ready, and valuable help during the course of this investigation. The author also wishes to express his grateful thanks to Dr. G. Herzberg for his helpful discussions and kind interest in this work.

REFERENCES

- CURRY, J., HERZBERG, L., and HERZBERG, G. 1933. Z. Physik, **86**, 348.
DRESSLER, K. 1955. Helv. Phys. Acta, **28**, 563.
GHOSH, P. N. and BALL, G. N. 1931. Z. Physik, **71**, 362.
MULLIKEN, R. S. and CHRISTY, A. 1931. Phys. Rev. **38**, 87.
PETRIKALN, A. 1928. Z. Physik, **51**, 395.
SEN GUPTA, A. K. 1935. Proc. Phys. Soc. (London) **47**, 247.
SINGH, N. L. 1957. (Private communication.)

PROPERTIES OF CADMIUM SULPHIDE PHOTOCONDUCTIVE CELLS¹

R. L. WILLIAMS

ABSTRACT

Measurement of the noise spectra of cadmium sulphide photoconductive cells from 10 to 10 Mc/sec has failed to reveal a transition from the $1/f$ to the $1/f^2$ noise frequency dependence. This clearly demonstrates a complete lack of dependence of the $1/f$ noise spectrum on the photoconductive time constant, which is approximately 30 milliseconds.

No noise correlation has been observed, indicating a minority carrier lifetime of less than 10^{-7} seconds.

The extreme difference between the minority carrier lifetime and the photoconductive time constant is explained by assuming that most of the recombination takes place at the surface of the film, but that the rate of recombination is controlled by diffusion. Slow diffusion of the minority carriers is a consequence of their very short lifetimes.

The noise power and time constants of CdS have been observed to depend on the value of the series resistance used with the cell. The two effects are believed to be related and to arise from the presence of intercrystalline barriers.

INTRODUCTION

Noise Spectra

Two types of excess noise spectra have been observed for semiconductors. These are generation-recombination and $1/f$ noise. Generation-recombination, or g-r., noise has a spectral form identical with the frequency response of the cell, and is predicted on the basis of the random generation and recombination of electrons and holes in semiconductors. This type of noise will always be present even in ideal semiconducting materials (Petritz 1956).

Noise of the $1/f$ form has been observed for most semiconducting cells and in many cases it completely dominates the g-r. form. It appears that the $1/f$ noise is related to the surface properties of semiconductors (Kingston 1956; Morrison 1956). However, Hill and Van Vliet (1958) have shown that recombination controlled by surface states does not necessarily result in dominance of $1/f$ noise. Van Vliet and Van der Ziel (1958) have also shown that any process that depends on diffusion will not give rise to $1/f$ noise. Possible sources of $1/f$ noise are discussed by McWhorter (1956).

Since cadmium sulphide cells are polycrystalline, $1/f$ noise could result from the passage of a current through barriers or junctions in a controlled manner. Gianola (1956) observed a $1/f$ spectrum when a current was passed through a crystal diode. This follows the type of argument suggested by Petritz (1957).

Hyde (1956) reported a transition from a f^{-1} to a f^{-2} spectrum, and it occurred near a frequency equal to the reciprocal of 2π times the photo-

¹Manuscript received May 14, 1958.

Contribution from Canadian Armament, Research and Development Establishment, Valcartier, Que.

conductive time constant, τ_p . The noise measurements were not accurate enough to ensure that the transition from a f^{-1} to a f^{-2} spectrum was real. A lack of any dependence of the $1/f$ noise spectrum on τ_p has been demonstrated in the present work. In fact, no f^{-1} to f^{-2} transition was observed in the frequency region 10 cycles/sec to 10 Mc/sec. The photoconductive time constant of the CdS studied is approximately 30 milliseconds.

In the course of the investigations, it was noticed that changes in the magnitude of the load resistor affected the noise current in an unexpected manner as well as the photoconductive response time. This effect has been investigated in detail.

By means of correlation experiments, Montgomery (1952) appeared to establish that τ_p could be related to the $1/f$ noise. The noise voltage observed at one point along a germanium filament was transferred in part to a second point near by with a time delay predicted from the known minority carrier drift mobility. A similar type of measurement has been performed with CdS cells in the course of the present investigation. No correlation was observed with these cells.

The resistance of the CdS cells investigated was usually too great to permit accurate measurements over the whole frequency range from 10 cycles/sec to 10 Mc/sec when the cell was in darkness. Practically all the noise measurements were therefore made with the cell resistance reduced by radiation from a small tungsten lamp. A series of noise and time constant measurements were performed at elevated temperatures to see if the thermal and radiation effects are different in the cells being tested. Van Vliet *et al.* (1956) has shown that with single crystal cadmium sulphide the wavelength of the radiation falling on single crystals affects the time constant and the noise, but only to a small degree.

Cadmium Sulphide Cells

The cadmium sulphide cells used were manufactured by the Canadian Marconi Co. The electrical contacts were of indium and proved to give good ohmic behavior. A review of the characteristics of similar cells is given by Bube (1956) and Kroger *et al.* (1954). The cell characteristics as given by the manufacturer are: electron mobility, approximately $300 \text{ cm}^2/\text{v}\cdot\text{sec}$, and time constant from 10 to 100 milliseconds.

The cells are multisectioned cells, as shown in Fig. 1(a). For the present experiments, the individual sections of a cell were separated by scraping off the indium contact between successive cell sections. Electrical contact was made to the indium by placing a fine wire against it and then covering the wire with silver paint. The cell and contacts had a linear current-voltage characteristic of at least the experimental accuracy of 3 or 4%. No photovoltaic effects could be observed with these cells, even for light signals which changed the average resistance by a factor of 10. Figure 1(b) illustrates the form used for noise measurements, while Fig. 1(c) shows the arrangement used when correlation effects were studied.

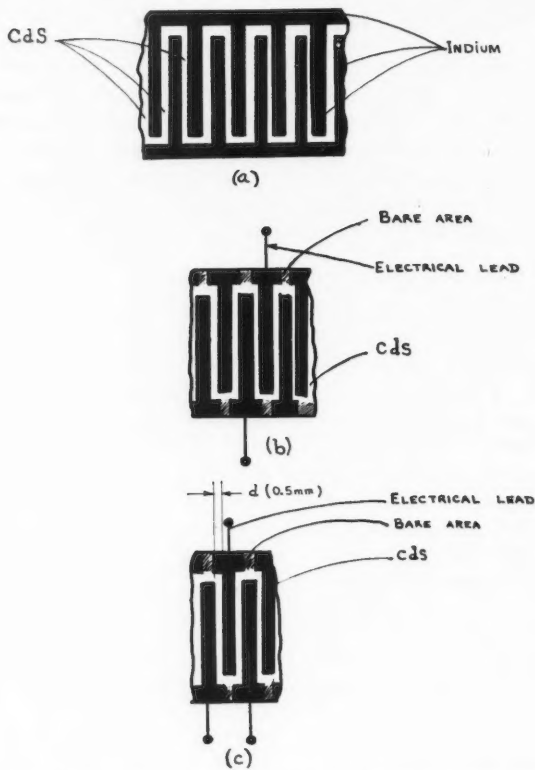


FIG. 1. CdS cells showing their structure and method of making contact.

NOISE SPECTRA

Technique

The noise spectra of CdS cells have been measured from 10 cycles/sec to 10 Mc/sec. The equipment used consisted of 3 units. In the region from 10 cycles/sec to 15 kc/sec a General Radio wave analyzer was employed. The signal was tapped from the stage preceding the meter and passed to a Ballantine r.m.s. voltmeter. The average value of at least 30 seconds of the recorded d-c. mean square output of the meter was used for each reading. The zero current noise level, the Johnson noise, was recorded for calibration of the apparatus and to enable zero current noise corrections to be made. As the square of the noise voltage was being recorded, only a simple subtraction of the zero current noise from the recorded value was necessary.

The high frequency region was covered by two specially constructed wave analyzers whose frequency ranges, 1 kc/sec to 200 kc/sec and 60 kc/sec to 10 Mc/sec, were chosen to overlap appreciably. The sensitivity of these

laboratory analyzers was at least as good as that of commercial models. In all cases the noise was measured with a constant band width.

With these three analyzers, there was sufficient frequency overlap for the relative noise spectrum from 10 cycles/sec to 10 Mc/sec to be drawn by adjusting the ordinates of the curves obtained with the different instruments, so that the curves coincided in the frequency overlap regions. This eliminated the necessity for calibration of the instruments.

In the high frequency region the noise voltages all were small, and care had to be taken to reduce amplifier noise. Using a cascode circuit and 6 AK 5's as input tubes, an equivalent noise resistance of approximately 1500 ohms was realized. The minimum cell circuit resistance used was 1000 ohms so that amplifier noise was not a serious handicap in the measurements.

The cells were prepared as shown in Fig. 1(b) and only one section was investigated at a time.

Results

Detailed frequency spectra of three cells were taken along with limited noise measurements on four others. The magnitude of the noise voltage was comparable in all cases and the noise spectra were all very similar. Cell B-68-6 was investigated most thoroughly and will be discussed as representative of all the cells.

Figure 2 is a graph of the spectra obtained at room temperature with various currents I_e . The series resistance R_s was 1000 ohms and the illumination falling on the cell was such as to reduce the cell resistance R_e from approximately 5 megohms to 8000 ohms. The other symbols used on the graphs are V_e , the cell voltage; f , the frequency of operation; and V^2 , the mean square noise voltage observed.

Figures 3 and 4 show the same type of measurement. In Fig. 3 the series resistance was increased to 100 kilohms ($k\Omega$), and in Fig. 4 the cell resistance was raised from 8 $k\Omega$ to 100 $k\Omega$, the series resistance now being 1 megohm.

Figures 3 and 4 do not cover the full frequency range, since the high value of R_e made it impossible to take accurate measurements at the highest frequencies.

The curves of Fig. 2 are nearly $f^{-1.5}$ in the megacycle region, but are closer to $f^{-1.0}$ at the kilocycle region.

A transition from a f^{-1} to f^{-2} frequency spectrum would indicate a short time limit of the surface trapping times (Van der Ziel 1950). In Fig. 2 no transition to f^{-2} occurs. Using the fact that the noise spectra do not change to a f^{-2} frequency dependence to at least 10 Mc/sec, and assuming that $\omega\tau = 1$ at such a transition, some surface trapping times must be less than 1.7×10^{-8} seconds.

Analysis

To analyze the spectra, data were taken from curves of the type shown in Figs. 2-4 in the 1 to 50 kc/sec region, where noise approximating to the $1/f$ spectrum was found in all curves. A form $i^2 = AI^\beta/f^\alpha$ was assumed for the noise current i . The voltage observed was related to i by the equation

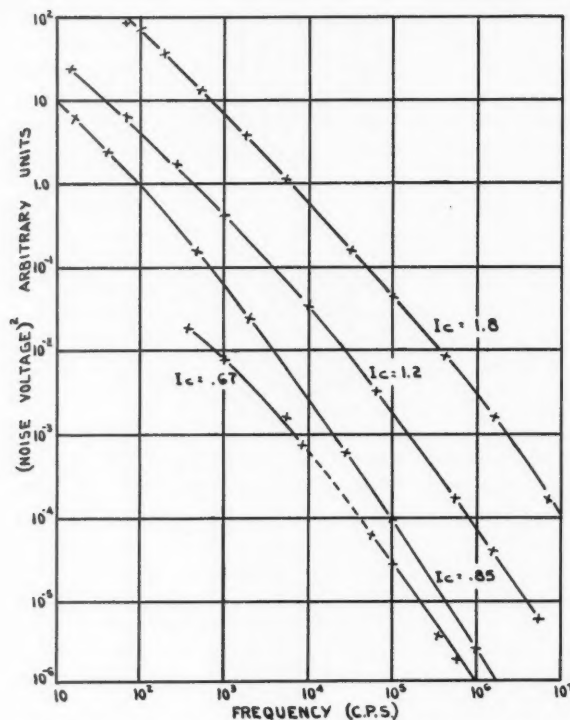


FIG. 2. Noise spectra of CdS photocell B-68-6 section 8. $R_e = 8 \text{ k}\Omega$, $R_s = 1 \text{ k}\Omega$ wire wound. Cell current as indicated on graph is expressed in milliamperes.

$V = i(R_e R_s / (R_e + R_s))$. Values of α , β , and A were calculated and are listed in Table I for cells B-68-6 and B-68-8.

TABLE I
ANALYSIS OF NOISE DATA ASSUMING A FORM $V^2 = A [R_s R_e / (R_e + R_s)]^{1/2} I^\beta / f^\alpha$

R_e $\text{k}\Omega$	R_s $\text{k}\Omega$	α	β	I_e ma	f kc/sec	A ($\times 10^{10}$)	τ msec
B-68-6 section 8							
8	10	1.1	2.3	.78	20	1.7	10
8	100	1.1	2.7	.85	20	7.8	30
100	100	0.9	2.1	.075	20	1.6	60
100	1000	1.0	2.0	.021	20	0.38	90
B-68-8 section 3							
10	10	0.89	1.9	.75	10	1.3	25
100	100	1.2	1.7	.11	20	6.4	70
1000	1000	1.0	1.7	.072	20	1.3	—
1000	1000	1.1	2.1	.22	20	8.1	—

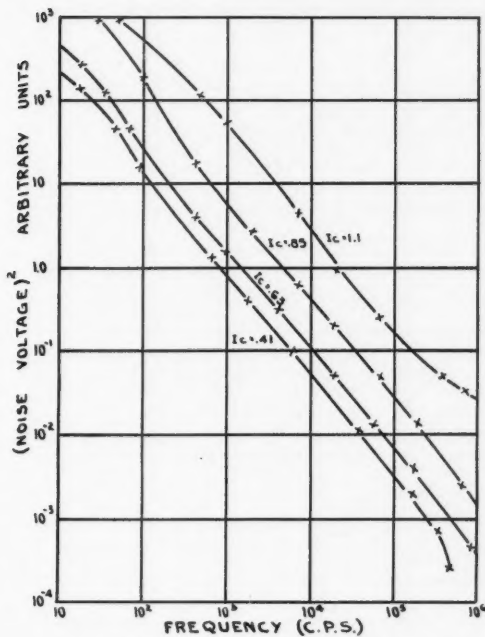


FIG. 3. Noise spectra of CdS photocell B-68-6 section 8. $R_e = 100 \text{ k}\Omega$, $R_s = 1 \text{ megohm}$ wire wound. Cell current as indicated on graph is expressed in milliamperes.

Figure 5 is a curve of A for fixed values of f and I_e but for variable R_e and R_s . The curves in fact are of i^2 but under the conditions of measurements $i^2 \propto A$. It was expected that A would be independent of R_s but this proved not to be the case.

For a fixed cell resistance, if $R_s > R_e$, A is almost independent of R_s , but for small values of R_e and $R_s < R_e$, A becomes a function of R_s . The variation of A with R_s is most marked for values of R_s less than $10 \text{ k}\Omega$. For the converse case of $R_s = \text{constant}$, A is always a strong function of R_e and has a minimum value which shifts to higher values of R_e if R_s is increased.

When small values of series resistance were used, readings were often difficult to take as many "peaks" were observed. These "peaks" were large transients which sometimes made readings impossible. If the whole band-pass of the preamplifiers were observed on an oscilloscope, sudden changes in the mean noise level would be observed with a slow drift back to the mean level. In one very bad case with $R_e = 10 \text{ k}\Omega$ and $R_s = 1 \text{k}\Omega$ readings were impossible and fluctuations could be seen on a voltmeter used to observe the voltage across the cell. This suggests $\Delta R/R$ changes of the order of 1%. This is very large by comparison to the $\Delta R/R$ changes associated with normal noise when $\Delta R/R$ is of the order of 10^{-8} (Brophy 1957).

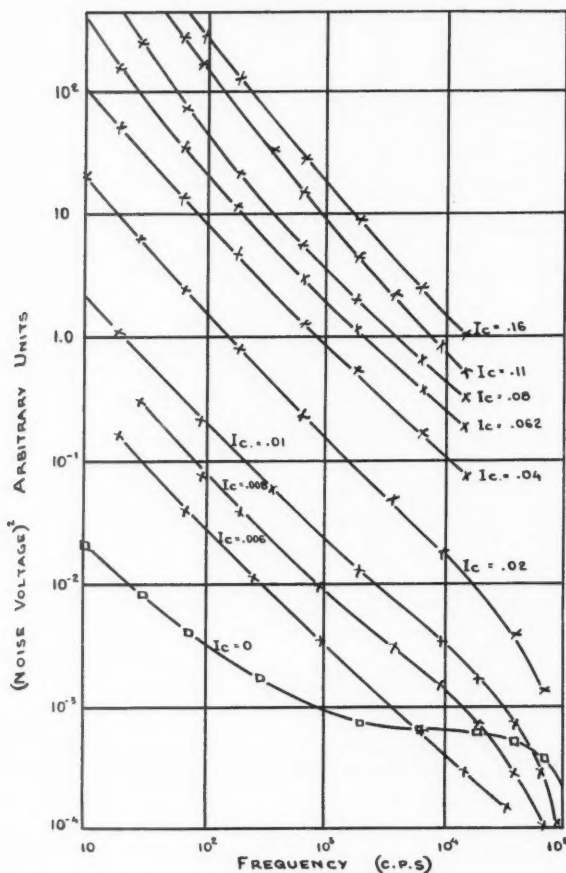
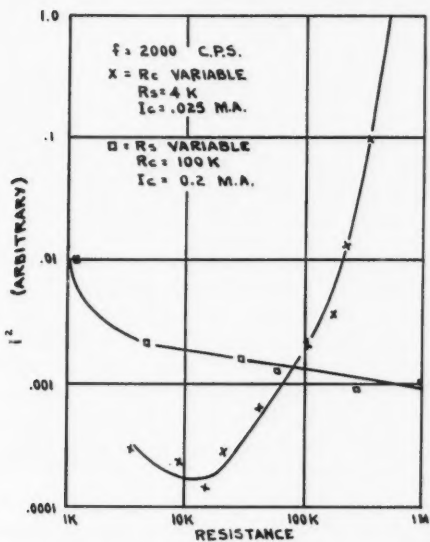


FIG. 4. Noise spectra of CdS photocell B-68-6 section 8. $R_e = 8 \text{ k}\Omega$, $R_s = 100 \text{ k}\Omega$ wire wound. Cell current as indicated on the graph is expressed in milliamperes.

TIME CONSTANT EFFECTS

The photoconductive response times of the cells were determined using as a light source a neon bulb triggered by a manually operated mercury switch. The response time of the neon was known to be less than a microsecond, and that of the circuit used to measure time constants was approximately 30 microseconds. The measurements were taken visually from an oscilloscope with estimated errors of about 20%.

Table II lists the measured response times of four different cells with various values of R_e and R_s . For each cell resistance, the series resistance was varied from 1 to 1000 $\text{k}\Omega$. The response time depends on the series resistance

FIG. 5. Variation of A ($\propto I^2$) with R_c (\times) and R_s (\square). Cell B-68-5 section 3.

and, within the accuracy of the measurement, it always increases as R_s decreases, approaching an approximately constant value for small R_s . The variation of response time with R_s is much more marked for low values of cell resistance.

TABLE II
DEPENDENCE OF THE RESPONSE TIME OF CADMIUM SULPHIDE CELLS ON THE SERIES RESISTANCE

R_c	R_s	B-68-6-8, τ , sec	B-68-5-3, τ , sec	B-68-4-3, τ , sec	B-68-8-3, τ , sec
10 k Ω	1 k Ω	.011	.013	.020	.012
10 k Ω	10 k Ω	.010	.010	.012	.017
10 k Ω	100 k Ω	.003	.004	.008	.0035
10 k Ω	1 M Ω	.0035	.0048	.006	.003
100 k Ω	1 k Ω	.052	.068	.100	.068
100 k Ω	10 k Ω	.060	.070	.095	.060
100 k Ω	100 k Ω	.018	.032	.060	.040
100 k Ω	1 M Ω	.009	.019	.032	.011
1 M Ω	1 k Ω	.240	.280	.440	.230
1 M Ω	10 k Ω	.240	.300	.400	.280
1 M Ω	100 k Ω	.150	.150	.320	.240
1 M Ω	1 M Ω	.050	.145	.240	.100

It is to be noted that the conditions under which both the time constant and A vary with the value of R_s is one of high current.

CORRELATION

Experimental Technique

The method used to measure correlation effects followed essentially that of Montgomery (1952). The electrical circuitry associated with the cell is indicated in Fig. 6. Two separate amplifiers were connected so that the mean square value of the noise voltage could be determined for contacts (1) and (2), and their sum and difference (addition 180° out of phase). A Ballantine meter was used to convert the signal to a d-c. voltage proportional to the mean square of the noise voltage. The mean square output was recorded as mentioned earlier.

Results

Four cells were tested in all, and in no case was there evidence of correlation in excess of two per cent. This limit is set by the accuracy of the apparatus.

For low values of the correlation coefficient p , the relationship developed by Montgomery reduces to $p = \tau_m/2 \tau_d$. In this expression τ_m is the average minority carrier lifetime and τ_d the time for an electron to travel the distance between the probes, d , Fig. 1(c).

Before estimating τ_m , using the above equation, the physical arrangements of the electrodes will be considered. Figure 7 indicates a cross section of the cell.

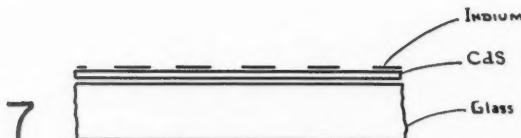
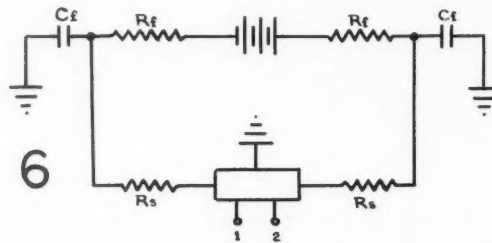


FIG. 6. Constant-voltage method of operating a cell for correlation studies. R_f and C_f are used for filtering the battery supply.

FIG. 7. Cross section of CdS cell.

The feature of the cell to be considered is that the electrodes are metallic and short out the field in the film below this region. Montgomery suggested a reduced value of d because of the reduced field in the region of the contact. In the case under consideration we neglect completely the region under the

electrode. Since the contacts were ohmic and no photovoltaic effects could be observed with the cells, the contacts were not believed to be noisy. If this is the case and if the electrodes are completely shorting, then electrons coming to one of the electrodes cause an equal number of electrons to leave the other side of the electrode.

Assuming an electron mobility of $300 \text{ cm}^2/\text{v-sec}$ and using the experimental conditions $d = 0.5 \text{ mm}$ and $E = 100 \text{ v/cm}$, since p was observed to be less than 0.03, τ_m must be less than 10^{-7} seconds.

As a detail model for the production of $1/f$ noise is lacking, the significance of τ_m must be considered. With germanium there is little or no trapping of carriers so that the drift mobility is essentially the Hall mobility. If $1/f$ noise results from surface trapping of carriers any disturbance resulting from trapping, or emission, at the surface can be propagated down the filament with a velocity equal to the mobility times the electric field. With CdS trapping of minority carriers in the crystal prevents the drift of a charge density disturbance arising from surface traps. The value of τ_m obtained, 10^{-7} seconds or less, can be taken as evidence of a very small minority carrier lifetime. The long photoconductive time constant then represents the majority carrier lifetime, the time between creation of an electron hole pair and their eventual recombination, the minority carrier having been trapped very quickly. Woods (1957) has demonstrated that photoconductivity in lead sulphide results from majority carrier conduction.

EQUIVALENCE OF THERMAL AND OPTICAL EXCITATION

Double time constant effects and quenching are often observed for a particular wavelength of light. Van Vliet *et al.* (1956) have in fact shown that light of wavelength less than 5900 \AA produces effects in CdS single crystals different from those produced by light of wavelength greater than 5900 \AA . Thermal excitation was therefore used to establish that the light source was not responsible for some of the effects observed.

Experimental Technique

The cells were mounted on a brass block whose temperature could be controlled. The cell mount was suspended in a vacuum chamber whose outer wall was in contact with a constant temperature bath, normally at 0° C . The cell was heated to various temperatures up to 170° C , and the noise spectrum and time constant were determined. The temperature used varied between 0° and 170° C . After these measurements had been completed the cell was cooled and air admitted to the system to maintain the cell at 0° C , the temperature of the bath. A filament lamp was used to illuminate the cell, the radiation being admitted through a sapphire window on the end of a copper-nickel tube extending outside the bath. The illumination was varied until the cell resistance reached one of the values used in the high temperature measurements: then the noise spectrum was measured again. As the cell resistance was brought to the same value in both cases, the same voltages and current were immediately available for both noise spectra measurements. Any changes

in the amplitude of the noise voltage then indicated changes in the noise power under the two operating conditions. Calibration of the amplifier was not necessary as the zero current noise level was used as a reference for comparing the sets of data. Under conditions of high illumination, the zero current noise was found to be the same as that obtained from a wirewound resistor, equal in resistance to the cell.

Results

Figure 8 is representative of the data which were obtained. In general, the actual magnitude of the noise was not very different from the value obtained by optical excitation. However, for a given resistance value, the noise voltages were usually slightly higher if the resistance was determined by heating the cell, rather than by illuminating it. The form of the noise spectra was not apparently changed by the optical excitation.

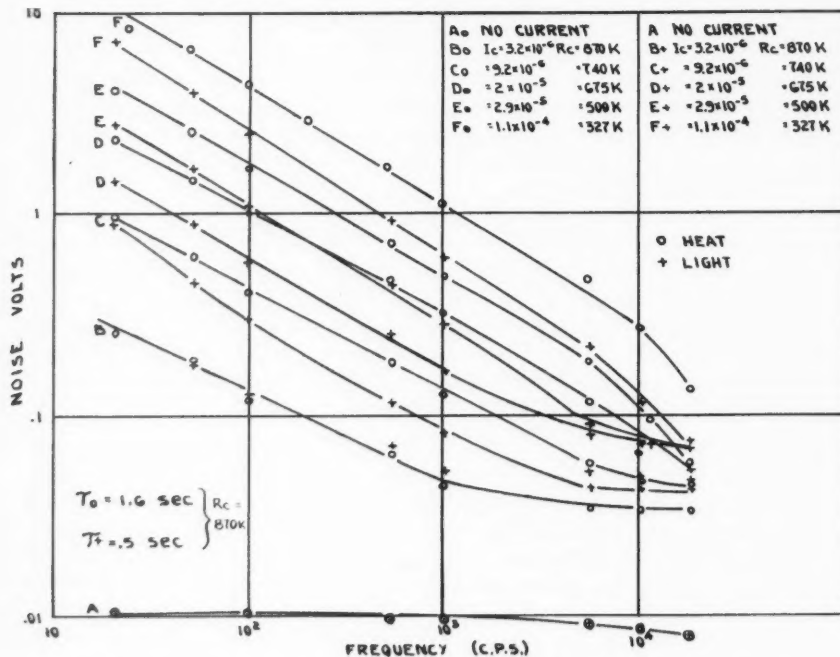


FIG. 8. Noise spectra taken with the resistance reduced thermally (O) and by illumination (+). Cell B-68-4 section 3.

The photoconductive time constant for thermal excitation is about one-third of the value obtained under optical excitation conditions.

The significance of these experiments is that the peculiarities of the noise spectra cannot be attributed to the excitation mechanism.

INTERPRETATION

1/f Noise

In the discussion which follows it will be assumed that $1/f$ noise results from surface effects. The points that have been demonstrated are that the $1/f$ noise and the photoconductive time constant can not be related and that minority carrier lifetime is less than 10^{-7} seconds. In addition, other information can be inferred from the time constant of 30 milliseconds. If surface recombination was active, for a film of the order of 10^{-4} cm thick, using the equation $1/\tau = (1/\tau_B) + (2s/d)$, for bulk recombination to dominate $\tau_B < d/2s$, or s must be less than $1/50$ cm/sec. The surface recombination velocity can be much larger if diffusion controls the rate of recombination. It will be shown subsequently that the lack of correlation, i.e. minority carrier lifetimes less than 10^{-7} seconds, is consistent with this picture. Assuming that trapping of carriers at the surface is responsible for $1/f$ noise, it is clear that the minority carriers must be able to get to the surface so that trapping can take place.

The diffusion of carriers to the surface depends on the ability of both carriers to diffuse. The diffusion constant for both the electrons and holes is (Rittner 1956):

$$(2) \quad D = \frac{(n+p)D_e D_h}{n D_e + p D_h},$$

where n and p are the electron and hole concentrations, and D_e and D_h the diffusion coefficients for electrons and holes. For n -type CdS in which holes spend a large part of their time trapped $D \neq D_h$. Defining n_1 as the difference between the average density of electrons n_0 and the instantaneous value n , the one dimensional continuity equation is:

$$(3) \quad \frac{\partial n_1}{\partial t} = -\frac{n_1}{\tau_B} + D_h \frac{\partial^2 n_1}{\partial x^2}.$$

Shockley (1950) has solved this equation while considering the effects of the surface of a filament on the recombination of holes. One of the results of his analysis was that if carriers diffuse to the surface of a piece of material and recombine there, the decay with time of density disturbance will be exponential. For a rectangular bar of cross-sectional area d^2 , with a surface recombination velocity s , and in which the diffusion coefficient is D_h , when $sd \gg 2D_h$ the exponential time constant is

$$(4) \quad \frac{1}{\tau_D} = \frac{1}{\tau_B} + \frac{2\pi^2 D_h}{d^2}.$$

In the discussion to follow it will be assumed that the bulk lifetime τ_B is sufficiently large that $1/\tau_B$ can be neglected. It is to be noted that either s large or D_h small satisfies the condition governing the validity of the above equation. The model proposed for sensitized CdS photoconductive films is as follows. In the sensitization process, states which normally provide recombination paths for electrons and holes become charged electrically in such a way that the capture cross section for holes increases, while that for electrons

decreases. When the CdS film is sensitized the hole lifetime is very short and the electron lifetime long. The lifetime of electrons, in fact, becomes so long that recombination takes place primarily by surface states. The very fast surface states, trapping some of the carriers, give rise to the 1/f noise.

In the sensitization process, as well as the bulk recombination lifetime becoming long, the diffusion coefficient becomes small. This arises in the following way. If the hole lifetime is short a free hole will not diffuse an appreciable distance before being trapped. Actually, the holes spend a very high percentage of their times in traps, during which time they are immobile. The effective diffusion coefficient with traps, D_t , is then reduced from the trap free value, D_h , by the ratio of the time spent free, τ_v , to the time until recombination takes place, τ_D , or

$$(5) \quad D_t = \frac{\tau_v}{\tau_D} D_h.$$

For the minority carriers τ_D is the sum of the time spent in traps and the time spent in the valence band, τ_v .

Because τ_v/τ_D is small, D_t is small and the time constant

$$(6) \quad \tau_D = d^2/2\pi^2 D_t$$

is long.

Assuming a value of 10^{-4} cm for d and using $\tau_D = 3 \times 10^{-2}$ seconds, equation 6 predicts a value of 10^{-6} cm²/sec for D_t . This implies that for the condition $sd \gg 2D_h$, or, say $sd > 200 D_h$, s must be greater than 2 cm/sec. This is likely to be the case, since for germanium, the smallest value that can readily be obtained is 200 cm²/sec (Shockley 1950, p. 324).

The value of 10^{-6} for D_t is very small. Using this value for D_t and τ_D equal to the photoconductive time constant, equation (5) predicts a value of 10^{-9} seconds for τ_v . This value of τ_v is less than the lower limit set by the correlation experiment of 10^{-7} , but Rose (1957) has pointed out that from photovoltaic effects the value of τ_v must be less than 10^{-9} seconds. The small value of D_t is thus not unreasonable.

The very short hole lifetime and long electron lifetime in CdS can be explained. When chlorine is added to CdS in the sensitization process, electrons from these levels attach themselves to impurity sites with energy levels near the valence band. A large number of these states become negatively charged. With this charge the capture cross section for holes is increased and that for electrons decreased. The charging of the sites results in not only very short hole lifetimes but also long electron lifetimes.

Such a situation has been shown to exist for manganese doped germanium (Tyler and Woodbury 1956).

The role of diffusion in the manner discussed above has been used by the author (Williams 1958) to explain the production of 1/f noise when PbS cells are irradiated with short wavelength radiation.

Breakdown Effects

The variation of the time constant and current noise with the value of the

series resistance is attributed to the presence of intercrystalline barriers. It is to be noted that for small R_s , when $R_s < R_e$, the A discussed above was a function of R_s . The time constants are also affected by the series resistance. The following process is suggested to explain these effects. It is proposed that there are barriers present in the film and that sufficient field is applied to break some of these down. When $R_s > R_e$, the breakdown of barriers corresponds to a reduction of R_e and as a consequence reduces the electric field. The constant current condition, $R_s > R_e$, would thus tend to quench any such runaway process by reducing the field. Under constant voltage conditions, $R_s < R_e$, breakdown would not be quenched so readily.

The form of the spectra obtained in Fig. 2 is not precisely $1/f$. The deviation from $1/f$ is ascribed to the peculiarities of the breakdown. This is suggested since, at high series resistances (Fig. 4), the spectrum is very nearly $1/f$ and, under these conditions, none of the "peaks" mentioned earlier were observed.

The variation of time constant with R_s is in accord with the model suggested above. The time constants of the short-circuit cells are longer than those of the open-circuit cells. This can be explained by saying that the high external impedance quenches the runaway processes giving short response times. When the external impedance is low the breakdown runs itself out and the time constant is longer.

It is to be emphasized that the effects mentioned above were in general small but reproducible. The role of intercrystalline barriers has been considered in detail by Mahlman *et al.* (1956). The present work indicates that the barriers probably do exist but play only a secondary part in photoconductive films. The paper by Woods (1957) indicates that such is the case for PbS.

The experimental results reported suggest that trapping of the minority carrier controls, to a large degree, the characteristics of CdS cells. In addition, the series resistance effects are taken as evidence of small internal barriers. The illumination used to vary the cell resistance was not responsible for any of the effects observed.

ACKNOWLEDGMENTS

The author wishes to acknowledge many helpful discussions with Dr. G. Giroux, Mr. J. Hampson, and Dr. G. T. Pullan of this establishment.

REFERENCES

- BROPHY, J. J. 1957. Phys. Rev. **106**, 675.
- BUBE, R. H. 1956. Proc. I.R.E. **43**, 1836.
- GIANOLA, U. F. 1956. J. Appl. Phys. **27**, 51.
- HILL, J. E. and VAN VLIET, K. M. 1958. J. Appl. Phys. **29**, 177.
- HYDE, F. J. 1956. Proc. Phys. Soc. B, **69**, 242.
- KINGSTON, R. H. 1956. J. Appl. Phys. **27**, 101.
- KROGER, F. A., VINK, H. J., and J. VAN DEN BOOMGOARD. 1954. Z. physik. Chem. (Leipzig), **203**, 1.
- MAHLMAN, G. W., NOTTINGHAM, W. B., and SLATER, J. C. 1956. Photoconductivity conference (John Wiley & Sons, Inc., New York), p. 489.
- McWHORTER, A. L. 1956. In *Semiconductor surface physics*, edited by R. H. Kingston (Univ. of Penn. Press, Philadelphia), p. 207.
- MONTGOMERY, H. C. 1952. Bell System Tech. J. **31**, 950.
- MORRISON, S. R. 1956. Phys. Rev. **102**, 1298 (see also Kingston, R. H. and McWhorter, A. L. 1956. Phys. Rev. **103**, 534).

- PETRITZ, R. L. 1956. Phys. Rev. **104**, 1508.
PETRITZ, R. L. 1957. In *Semiconductor surface physics*, edited by R. H. Kingston (Univ. of Penn. Press, Philadelphia), p. 226.
RITTNER, E. S. 1956. Photoconductivity conference (John Wiley & Sons, Inc., New York), p. 219.
ROSE, A. 1957. Progress in semiconductors, Vol. 2, edited by A. F. Gibson (Heywood & Company, Ltd., London), p. 109.
SHOCKLEY, W. 1950. Electrons and holes in semiconductors (D. Van Nostrand Company, Inc., New York), p. 323.
TYLER, W. W. and WOODBURY, H. H. Phys. Rev. **102**, 647.
VAN DER ZIEL, A. 1950. Physica, **16**, 359.
VAN VLIET, K. M., BLOK, J., RIS, C., and STEKETEE, J. 1956. Physica, **22**, 723.
VAN VLIET, K. M. and VAN DER ZIEL, A. 1958. Physica, **24**, 415.
WILLIAMS, R. L. 1958. Paper given at the New York meeting of the Electrochemical Society. J. Electrochem. Soc. In press.
WOODS, J. F. 1957. Phys. Rev. **106**, 235.

SPACE CHARGE RELATIONS FOR THE LOW-FREQUENCY SILENT ELECTRIC DISCHARGE IN HYDROGEN¹

D. P. JATAR

ABSTRACT

The current-potential characteristics in hydrogen under the low-frequency silent electric discharge using an all-glass ozonizer are examined from the standpoint of the Child-Langmuir space charge relation and the modified Townsend-Werner equation. It is concluded that the three distinct regions in the characteristics correspond to the space-charge-free, the space-charge-limited, and the steady corona regimes.

INTRODUCTION

Studies (Jatar 1951, 1956-57) of the influence of ionic space charge on the Joshi effect have shown that even in chlorine the conductivity and the Joshi effect are determined chiefly by the space charge of positive ions rather than that of negative ions, the latter of which may not be at all necessary for the Joshi effect. This was confirmed by the observation (Jatar, in press) of a large Joshi effect over a wide range of pressure and potential in the so-called 'electron-free' hydrogen, which has a very low electron affinity. During these latter studies, the current appeared to rise as a parabolic function of the applied potential (Jatar 1956a), and the results could be explained by assuming a space-charge-limited regime over a certain range of potential. Other workers (Ahmed and Gill 1950; Deb and Ghosh 1948; Haries and Engel 1951) have also assumed the existence of positive ion space charge to explain the production of high frequency pulses under the silent electric discharge and the Joshi effect. Recent studies (Jatar 1956b, Jatar and Sharma 1956) have, however, shown that for potentials near the threshold potential, V_m , space charges are not active. It was therefore of interest to investigate the time at which the space-charge-free regime changed over to a space-charge-limited regime as the potential increased.

EXPERIMENTAL

The general experimental arrangement was essentially similar to that employed earlier (Jatar 1957) and is shown in Fig. 1. The hydrogen used was prepared by electrolysis of barium hydroxide solution and collected finally over P_2O_5 . An all-glass ozonizer of the Siemen's type was used as the discharge tube and was excited by an h.t. transformer using 50 cycles a.c. The current flowing through the discharge tube was measured by a galvanometer in the plate circuit of the detector (RCA 30), connected to the l.t. line across a transformer. The waveform of the discharge current was investigated by feeding the potential drop across a series resistance in the l.t. line to the vertical input of the cathode-ray oscilloscope.

¹Manuscript received February 18, 1958.

Contribution from the Department of Physics, University of Saugar, Saugar, M.P., India.

At a given pressure, as the potential applied to the tube was increased gradually from zero, the galvanometer registered practically zero current till a critical potential was reached at which there was a sudden rise in the current

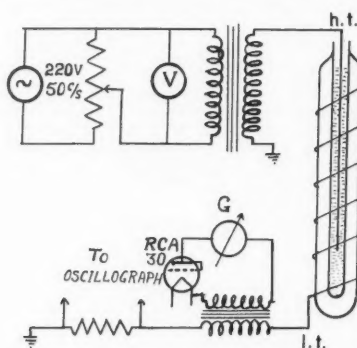


FIG. 1. The electrical circuit diagram.

flowing through the discharge tube. This was accompanied by the initiation of a glow characteristic of the gas in the system and also the appearance of high frequency pulses on the sinusoidal current waveform. This critical potential is called the threshold potential, V_m . Beyond this, the potential, V , applied to the tube was increased in regular steps and the current was measured both in dark, i_D , and under irradiation of a 200-watt bulb, i_L .

RESULTS

Figure 2 shows the variation of i_D and i_L with V for a few typical pressures of hydrogen. While these are discussed in detail elsewhere (Jatar 1957) it is seen that the current-potential characteristics exhibit three distinct regions: (a) the initial region of rapid rise near V_m up to V_A (b) the intermediate sag region corresponding to a slow rise in the conductivity up to V_B , followed by (c) a final fast rise in conductivity. It was pointed out (Jatar 1957) that the three distinct regions in the current-potential characteristics correspond to the space-charge-free, the space-charge-limited, and the steady corona regimes.

The suggestion of a space-charge-limited current above V_A is investigated from the standpoint of the $3/2$ power law, viz.

$$(1) \quad i = \frac{1}{9\pi} \sqrt{\frac{2e}{m}} \cdot \frac{V^{3/2}}{d^2} = \text{constant} \times V^{3/2}$$

if the electrode distance d is kept constant. Here e and m refer to the charge and mass of the charged particle. This equation was first deduced by Child (1911) for ions in arcs and independently by Langmuir (1913) for electron currents in vacuum. While this is obtained on the supposition that there is no

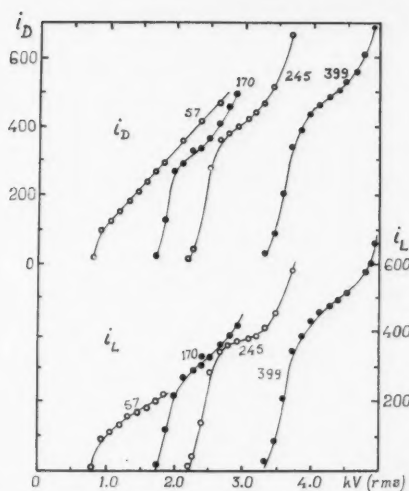


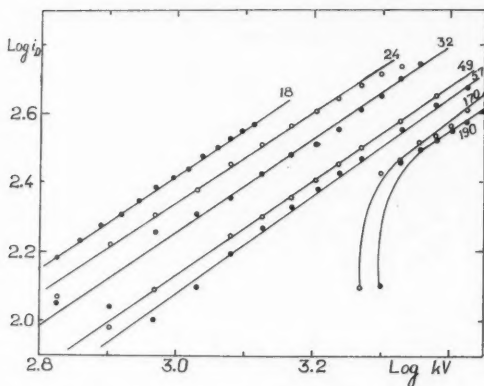
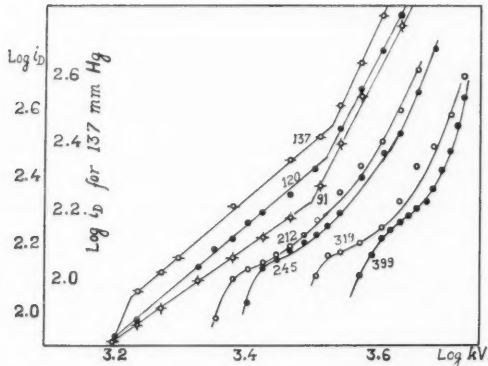
FIG. 2. Variation of the discharge current in dark, i_D , and that under light, i_L , with the applied potential, V . Current in arbitrary units, V in kv (r.m.s.). Numbers on curves indicate pressure of hydrogen in mm Hg.

ionization between the electrodes, Thomson (Thomson and Thomson 1934) has shown that this holds good when there is uniform ionization. This equation has been further extended by Langmuir and Compton (1931) for concentric cylinders, the current i , assuming negligible velocities of emission, being given by

$$(2) \quad i = \left(\frac{2}{9}\right) \sqrt{\frac{2e}{m}} \cdot \frac{LV^{3/2}}{r\beta^2}$$

where L is the length of the cylinder, r the radius of the collector (anode for electrons) and β^2 is a coefficient to be taken from the data given by Langmuir and Compton (1931). This equation is also applicable in the case of discharge in coaxial cylinders when the collector is surrounded by a space charge sheath of radius r_0 . As a first approximation, if it is assumed that the change in r_0/r and hence β^2 due to a change in V is negligible because of the large value of the inner cylinder, it is to be expected that the double logarithmic plots will be linear. These are shown in Figs. 3 and 4, which show that up to about 200 mm Hg, the curves are linear beyond V_A . For pressures between 90 mm Hg and 200 mm Hg these curves also indicate a second linear region corresponding to the region of a final fast rise in conductivity beyond the transition potential V_B . At these high pressures and potentials, it is not unlikely that the assumption is not valid that β^2 does not change appreciably as a result of a change in V .

An examination of the slope of these double log plots, however, indicates

FIG. 3. Log i_D -log V plots for the Child-Langmuir relation.FIG. 4. Log i_D -log V plots for higher pressures of hydrogen.

that the slope is more nearly 2 instead of $3/2$, as is to be expected from the $3/2$ power law. The data is therefore further examined from the standpoint of the Werner's equation (1934), which reads

$$(3) \quad V(V - V_s) = \frac{\pi C p i}{K} \left[(A^2 - a^2) - (r_u^2 - a^2) \frac{\log(A/a)}{\log(r_u/a)} \right]$$

where V refers to the applied potential, V_s to the starting potential, A and a are, respectively, the radii of the outer and inner electrodes, r_u is the radius of the zone of intense ionization surrounding a , p is the gas pressure, i is the current at V , K is the ionic mobility at 1 mm Hg, and C is a constant of proportionality and is equal to $\{\log(A/a)\}/2\pi$. This equation was derived by Werner in a study of Geiger counter action. Neglecting a compared to A and $(r_u^2 - a^2)$ compared to A^2 , the equation becomes

$$(4) \quad V(V - V_s) = \frac{\rho i A^2}{2K} \log(A/a),$$

which was derived by Townsend (1914) as early as 1914, on the same reasoning but with simplified assumptions. According to these equations the current is zero at $V = V_s$ and rises as a parabolic function of V for $V > V_s$ (Fig. 2). While the general shape of the curves in the present case does correspond approximately to a parabola at least above V_A , a further examination revealed that the curves show appreciable deviation especially for higher pressures. This is shown in Figs. 5 and 6, in which i is plotted against $V(V - V_m)$. Ac-

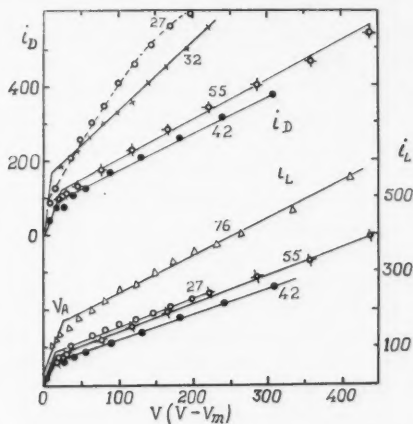


FIG. 5. Variation of i_D and i_L with $V(V - V_m)$ for the modified Townsend-Werner equation.

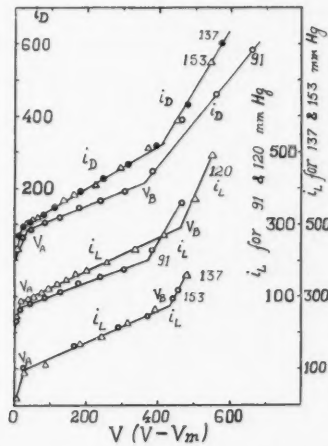


FIG. 6. Variation of i_D and i_L with $V(V - V_m)$ for higher pressures of hydrogen.

cording to Townsend's equation, these curves should be linear. The same holds good according to Werner's equation on the assumption that r_u does not change with increasing V . Figs. 5 and 6 show that i varies linearly with $V(V - V_m)$ only for the intermediate pressure range, from 30 to 100 mm Hg. It is of interest to note that for lower pressures, e.g. 24 and 27 mm Hg, while the curves for i_L are linear, those for i_D are not so (Fig. 5). The curves for higher pressures (Fig. 6) show three almost linear regions corresponding to the three regions in the current-potential characteristics. As suggested earlier (Jatar 1957; 1956b) V_A corresponds to the potential at which space charges set in. A change in the slope of the curves as seen in Figs. 4 and 5 is therefore to be anticipated. Werner's equation, as given above, may be modified to $V - V_m = iR$ where R has the dimensions of a resistance and expresses the corona gap resistance. When $r_u = A$, R becomes zero because the term in brackets in Werner's equation becomes zero. Under these conditions, theoretically no space charges are active. This condition holds for the region above V_B . A change in slope at V_B , as seen in Fig. 6, lends support to the above view. It is significant to note, however, that at V_B , i does not become infinite, as would be the case if $R = 0$. Thus while a change in the slope of the curves in Fig. 6 indicates a decrease in the corona resistance, the latter does not become zero at any potential in the range investigated here. This suggests that even at these high potentials, while they do not play a prominent role, meager space charges are present. In view of the simplifying assumptions made in deriving the equation and also in applying it to the present case, the agreement is more than satisfactory. It is to be concluded that the three distinct regions in the $i_D - V$ characteristics correspond to the space-charge-free, the space-charge-limited, and steady corona regimes.

REFERENCES

- AHMED, R. and GILL, P. S. 1950. Current Sci. **19**, 206.
 CHILD, C. D. 1911. Phys. Rev. **32**, 492.
 DEB, S. and GHOSH, N. 1948. J. Indian Chem. Soc. **25**, 449.
 HARIES, W. L. and ENGEL, A. 1951. Proc. Phys. Soc. (London), B, **64**, 916.
 JATAR, D. P. 1951. Ph.D. Thesis, Banaras Hindu University.
 ——— 1956a. J. Chem. Phys. **24**, 1273.
 ——— 1956b. Proc. Natl. Acad. Sci. **25**, 38.
 ——— 1956-57. J. Sci. Research, Banaras Hindu Univ. **7** (1), 10.
 ——— 1957. Saugar Univ. J. **6**(II)A, 60.
 JATAR, D. P. and SHARMA, H. D. 1956. J. Sci. Ind. Research, B, **15**, 417.
 LANGMUIR, I. 1913. Phys. Rev. **2**, 450.
 LANGMUIR, I. and COMPTON, K. T. 1931. Revs. Modern Phys. **3**, 131.
 THOMSON, J. J. and THOMSON, G. P. 1934. Conduction of electricity through gases. Vol. II (C.U.P.).
 TOWNSEND, J. S. 1914. Phil. Mag. **28**, 83.
 WERNER, S. 1934. Z. Physik, **90**, 384; **92**, 705.

THE VISIBLE EMISSION SPECTRUM OF Cl_2^+ ¹

V. VENKATESWARA RAO AND P. TIRUVENGANNA RAO

ABSTRACT

Two visible emission band systems attributed to the ionized molecule Cl_2^+ were studied using the second order of a 21-ft concave grating spectrograph (dispersion 1.25 Å/mm). Rotational analyses have been carried out for six bands of system I and six of system III for which new vibrational analyses have recently been proposed by Haranath and Rao. The rotational analyses of the bands of these two systems are consistent with the vibrational assignments. Rotational constants for the upper and lower states of the two systems have been derived. Both the vibrational and rotational analyses of systems I and III indicate case (c) 1/2-1/2 and 3/2-3/2 transitions respectively for the two systems. Potential energy curves are drawn for the upper and the lower states of each of the two systems. The lower states dissociate into a normal $\text{Cl}(^3P) + \text{Cl}^+(^3P)$ while the upper states dissociate into a normal $\text{Cl}(^3P) + \text{an excited Cl}^+(^1D)$. It is suggested that the lower state of system III is probably the normal state of Cl_2^+ from theoretical and experimental evidence.

INTRODUCTION

The emission spectrum of chlorine was investigated by early workers (Uchida and Ota 1928; Elliot and Cameron 1937 and 1938) and is well known to consist of a series of bands in the visible region degraded towards the red. These bands do not correspond to the well-known absorption bands of chlorine in the visible region and were attributed by Elliot and Cameron (hereafter to be referred to as EC) to the molecule Cl_2^+ from a vibrational analysis and rotational analysis of some of the bands. EC proposed a vibrational analysis of the bands on the basis of two systems designated as systems I and II and suggested that the observed features of the two band systems indicate a transition of the type ${}^2\text{II}-{}^2\text{II}$. The following vibrational formulae were derived by them.

$$\text{System I } \nu = 20797.3 + [572.3(v'+1/2) - 5.32(v'+1/2)^2 - 0.013(v'+1/2)^3] \\ - [645.3(v''+1/2) - 2.91(v''+1/2)^2],$$

$$\text{System II } \nu = 20596.9 + [564.8(v'+1/2) - 4.13(v'+1/2)^2 - 0.038(v'+1/2)^3] \\ - [645.2(v''+1/2) - 2.89(v''+1/2)^2].$$

The rotational analysis of some of the bands belonging to both the systems showed that the quantum number J is half integral, which confirmed that the two systems arise from the ionized molecule Cl_2^+ . Although the vibrational analysis was supported by the observed chlorine isotope effect, there were several inconsistencies, some of which were pointed out recently by Howell (1953). (i) The intensity distribution in both the systems is inconsistent with the values of ω_e' and ω_e'' derived from the analysis. (ii) The values of the rotational constants B' and B'' do not run parallel to the derived values of

¹Manuscript received May 30, 1958.

Contribution from the Spectroscopic Laboratories of the Andhra University, Waltair, S. India.

ω'_e and ω''_e , that is the ratio B_e/ω_e is not constant for each of the pairs of electronic states of systems I and II. As mentioned by Howell for the neutral halogen molecules the ratio B^2/ω_e is approximately constant for a pair of electronic states of the same molecule. Using the rotational and vibrational data of EC for Cl_2^+ , it is found that this rule fails badly. (iii) The value of the energy of dissociation in the normal state of Cl_2^+ obtained from a Birge-Sponer extrapolation is 4.4 ev as against 2.23 ev, which can be indirectly determined from the accepted values of the ionization potentials I of Cl and Cl_2 and the dissociation energy D of Cl_2 . (iv) As detailed electron configurations and predicted states for Cl_2^+ indicate (Mulliken 1934) the probable transition ${}^2\Pi_g - {}^2\Pi_u$ expected for the two systems corresponds to the transition of an electron from a bonding $w\pi$ orbital to an antibonding $v\pi$ orbital and should be accompanied by a considerable difference in the relative values of ω'_e and ω''_e . (v) The large number of gaps in the vibrational schemes suggests a fundamental weakness in the analysis which leaves a large number of prominent bands unclassified.

In view of the above weak points in EC's analyses, Haranath and Rao (1956) re-investigated the emission spectrum of Cl_2^+ and proposed a vibrational analysis on the basis of three systems designated as systems I, II, and III. The possibility of another system (IV) was also indicated. A detailed paper on the analysis is now in the course of publication in the Indian Journal of Physics. The vibrational constants of systems I and III are summarized below:

	ν_e	ω'_e	$x'_e \omega'_e$	ω''_e	$x''_e \omega''_e$
System I	20448.0	350.0	2.0	656.0	4.6,
System III	20569.0	347.5	2.0	655.0	5.5.

As can be seen from Figs. 5 and 6, most of the prominent bands belong to these systems. The new vibrational assignments were supported by the agreement between the observed and calculated chlorine isotopic separations. The proposed vibrational analysis of these two systems is entirely different from that of EC. The vibrational constants seem to indicate that these two systems may form two subsystems.

The present investigations on the visible emission bands of Cl_2^+ were carried out on a 21-ft concave grating spectrograph with a view to checking the correctness of the new vibrational assignments of Haranath and Rao and to derive the rotational constants of the upper and lower states of systems I and III.

EXPERIMENTAL

The spectrum was excited in high frequency discharge from a 100-watt oscillator of 16 Mc/sec frequency. The discharge tube was made of pyrex glass of length 30 cm and 18 mm in diameter. It had two side limbs which served as inlet and outlets for chlorine vapor. Chlorine was generated by electrical heating of cupric chloride in a separate tube and was allowed to pass through an absorbing tower containing P_2O_5 before entering the discharge tube. The main tube was also provided with a central tube of length 15 cm and was dipped in liquid air. The pressure of chlorine was regulated by

adjusting the current in heating coil. It was seen that chlorine vapor condensed both in the central tube and in the liquid-air trap which was introduced in between the discharge tube and a Cenco Hyvac pump. Occasional adjustment of the liquid-air level in the central flask was found necessary for obtaining a pure spectrum.

The spectrum was photographed in the region 5000 to 4000 Å in the second order of 21-ft concave grating spectrograph which was recently set up in this laboratory by one of the authors (V.V.). The grating has a dispersion of 1.25 Å/mm and a resolving power of 1,00,000 in the second order. Exposures varying from 8 to 16 hours were found suitable for obtaining good spectra using Ilford Special Rapid plates. In this region most of the prominent bands belonging to systems I and III were clearly obtained. Plates were measured using iron arc standards and the vacuum wavenumbers of the rotational lines were calculated. The relative accuracy of the measurements of the sharp lines is $\sim 0.07 \text{ cm}^{-1}$; however, for a few of the broad lines the error of measurement may be as great as 0.15 cm^{-1} .

ROTATIONAL ANALYSIS

On the basis of the predicted electronic states from electron configurations the possible electronic transition for systems I and III is expected to be of the type $^2\Pi_{\leftarrow}-^2\Pi_{\leftarrow}$. The vibrational constants of the upper and lower states of these two systems indicate that they may be the two components of the above transition. Further the doublet splittings in the two $^2\Pi$ states are expected to be large so that the transition may be $^2\Pi_{\leftarrow}-^2\Pi_{\leftarrow}$, with both the states approximating to Hund's case (a). Since large multiplet splittings of the order of 610 and 690 cm^{-1} are known in the ground states of Cl and Cl^+ atoms, one may even expect a tendency towards Hund's case (c). With case (a) each band splits into two subbands $^2\Pi_{3/2}-^2\Pi_{3/2}$ and $^2\Pi_{1/2}-^2\Pi_{1/2}$ and each subband consists of a single *P* and *R* branch and a very weak *Q* branch. In Hund's case (c) the two systems may better be represented as $3/2-3/2$ and $1/2-1/2$ transitions with the over-all rotational structure remaining the same as in case (a).

The wavenumbers of *R* and *P* lines follow the equation (Herzberg 1950)

$$\nu = \nu_0 + (B' + B'')m + (B' - B'' - D' + D'')m^2 - 2(D' + D'')m^3 - (D' - D'')m^4,$$

where $m = J+1$ for the *R* branch and $m = -J$ for the *P* branch. The effective rotational constants of the upper and lower states were determined from the equation

$$\Delta_2 F(J) = 4B_v(J+1/2) - 8D_v(J+1/2)^3,$$

in which the combination differences of the upper and lower states are obtained from

$$\Delta_2 F'(J) = R(J) - P(J),$$

$$\Delta_2 F''(J) = R(J-1) - P(J+1).$$

The detailed rotational analysis was carried out for six of the bands belonging to system I and six of the bands belonging to system III. The vacuum wave-

numbers and rotational assignments for the bands 11-3 and 11-4 of system I and 12-1 and 12-2 of system III are given in Tables I and II respectively.

TABLE I
VACUUM WAVENUMBERS AND ROTATIONAL ASSIGNMENTS FOR SYSTEM I

<i>J</i>	11-3		11-4	
	<i>P(J)</i>	<i>R(J)</i>	<i>P(J)</i>	<i>R(J)</i>
1.5	21974.67		21347.00	
2.5	973.66		346.15	
3.5	972.85	21976.14	345.19	
4.5	971.55	975.23	344.17	
5.5	970.36	974.67	342.70	21347.00
6.5	968.66	973.66	341.24	346.15
7.5	966.95	972.85	339.52	345.19
8.5	965.07	971.55	337.66	344.17
9.5	963.13	970.36	335.61	342.70
10.5	960.89	968.66	333.50	341.24
11.5	958.47	966.95	330.90	339.52
12.5	955.86	965.07	328.40	337.66
13.5	953.05	962.83	325.69	335.61
14.5	950.14	960.42	322.89	333.50
15.5	946.90	958.05	319.81	330.90
16.5	943.54	955.40	316.45	328.40
17.5	939.93	952.48	312.84	325.35
18.5	936.44	949.52	—	322.55
19.5	932.34	946.25	305.33	319.34
20.5	928.21	942.85	301.39	315.98
21.5	923.92	939.24	297.12	312.34
22.5	21919.55	21935.47	21292.81	—
23.5	914.91	931.53	288.10	21304.83
24.5	909.98	927.30	283.43	300.90
25.5	905.03	922.94	278.54	296.54
26.5	899.84	918.57	273.39	292.14
27.5	894.35	913.88	268.06	287.61
28.5	888.78	908.95	262.63	282.63
29.5	883.13	903.82	256.92	277.72
30.5	877.19	898.68	251.11	272.63
31.5	870.99	893.32	244.89	267.23
32.5	864.72	887.65	238.86	261.68
33.5	858.21	881.76	232.46	255.94
34.5	851.41	875.79	225.76	250.20
35.5	844.73	869.57	219.02	243.96
36.5		863.24	212.06	237.72
37.5		856.24		231.26
38.5		849.92		224.63
39.5		842.85		217.76
40.5				210.80

System I

In this system the 10-3, 10-4, 11-3, 11-4, 11-2, and 12-3 bands at 21669, 21041, 21976, 21349, 22610, 22280 cm⁻¹ respectively were found suitable for carrying out the rotational analysis. All these are accompanied by weaker isotopic heads on the longer wavelength side belonging to (Cl³⁵ Cl³⁷)⁺ species. However, for the 10-3, 10-4, 11-3, and 11-4 bands the rotational lines of the more abundant isotope can be clearly distinguished from those of the other. Hence these four bands are best suited for an accurate determination of upper and lower state rotational constants. For the 11-2 and 12-3 bands the rotational lines of the two species are partially superposed.

TABLE II
VACUUM WAVENUMBERS AND ROTATIONAL ASSIGNMENTS FOR SYSTEM III

<i>J</i>	12-1		12-2	
	<i>P(J)</i>	<i>R(J)</i>	<i>P(J)</i>	<i>R(J)</i>
5.5			22984.20	
6.5	23616.38		982.71	22987.53
7.5	614.66		980.96	986.44
8.5	612.59		979.04	985.14
9.5	610.38	23617.26	976.86	983.56
10.5	608.22	615.55	974.60	982.08
11.5	605.41	613.62	972.06	980.17
12.5	602.62	611.53	969.37	978.09
13.5	599.81	609.22	966.34	975.89
14.5	596.54	606.75	963.29	973.47
15.5	593.27	604.11	959.97	970.89
16.5	589.64	601.24	956.50	968.11
17.5	585.95	598.21	952.84	965.12
18.5	581.96	594.94	949.04	961.91
19.5	577.88	591.48	944.87	958.55
20.5	573.51	587.88	940.78	954.95
21.5	569.08	584.06	936.18	951.08
22.5	564.39	580.00	931.60	947.26
23.5	559.51	575.70	926.76	942.99
24.5	554.40	571.24	921.79	938.67
25.5	23549.08	23566.68	22916.56	22934.21
26.5	543.53	561.84	911.10	929.39
27.5	537.86	556.89	905.47	924.46
28.5	532.11	551.69	899.76	919.43
29.5	525.97	546.40	893.71	914.06
30.5	519.68	540.72	887.55	908.66
31.5	513.29	534.89	881.21	902.86
32.5	506.61	528.90	874.76	897.05
33.5	499.82	522.83	867.83	890.87
34.5		516.33		884.58
35.5		509.79		878.03
36.5		503.23		871.29
37.5		496.89		

The *J* numbering is fixed for 10-3, 11-3, and 12-3 bands by comparing the ground state combination differences. These combination differences are found to agree well within the accuracy of the measurements, thus confirming their vibrational assignments. Similarly for the 10-4 and 11-4 bands the *J* assignments are made. With *J* numbering derived above for the 10-3, 10-4 and 11-3, 11-4 bands it is found that the combination differences of the upper states of each of these two pairs agree well. The combination differences for upper state 11 in turn agree with those of 11-2. Thus the rotational analysis of these six bands is consistent with the vibrational assignments. It is interesting to note that although four of the bands 10-3, 10-4, 11-3 and 11-4 belong to two different systems in EC's vibrational analysis the absolute *J* numbering for these bands is the same in both the cases. The rotational lines of some of the bands are extended to high *J* values in our present work so that it has become possible to determine the *D*_v values. The rotational analysis also shows that *J* is half integral thus confirming EC's earlier conclusion that the emitter of these bands is Cl₂⁺.

Rotational Constants

After fixing the *J* numbering of the lines in the manner described, the

constants B_e and D_e are determined by plotting $\Delta_2 F(J)/(J+1/2)$ against $(J+1/2)^2$ both for the upper and lower states. The resulting B_e and D_e values are shown in Table III. In deriving B''_3 and D''_3 the average lower state combination differences of the 10-3, 11-3, and 12-3 bands were used, as these have well resolved P and R branches. Figure 1 is a reproduction of the 11-3 band. For B''_4 and D''_4 the 11-4 band is taken as the 10-4 band has superposed P and R branches throughout. The 11-4 band is reproduced in Fig. 2.

TABLE III
THE BAND ORIGINS, B_e AND D_e VALUES IN CM^{-1} FOR SYSTEM I

Band	ν_0	B'	B''	D'	D''
10-3	21668.14	0.175 ₅	0.265 ₇ *	$(0.34 \pm 0.04) \times 10^{-6}$	$(0.42 \pm 0.04) \times 10^{-6}$ *
10-4	21040.30	—	—	—	—
11-3	21975.67	0.173 ₈ *	0.265 ₇ *	$(0.21 \pm 0.04) \times 10^{-6}$ *	$(0.42 \pm 0.04) \times 10^{-6}$ *
11-4	21348.23	0.173 ₈ *	0.264 ₀	$(0.21 \pm 0.04) \times 10^{-6}$ *	$(0.21 \pm 0.04) \times 10^{-6}$

*Determined from the averages of combination differences.

The constants B'_{10} and D'_{10} are derived from the 10-3 band and B'_{11} and D'_{11} from the average upper state combination differences of 11-3 and 11-4 bands. As only few of the rotational lines are identified in 11-2 and 12-3 bands because of superposition, rotational constants B''_2 and B''_3 are not derived. The band origins shown in Table III are determined by plotting $R(J-1)+P(J)$ against J^2 according to the equation (Herzberg 1950)

$$R(J-1)+P(J) = 2\nu_0 + 2(B'-B'')J^2 - 2(D'-D'')J^2(J^2+1).$$

An examination of the 11-3 and 11-4 bands shown in Figs. 1 and 2 shows the rotational lines of the P branch down to $J = 1.5$. Although the P and R lines are superposed at low J values, an important conclusion can be drawn regarding the nature of the transition of system I. In both these bands the $P(1.5)+R(5.5)$ line is clearly observed. On the short wavelength side of this line the sudden drop in intensity of the rotational lines may be taken as an indication that the first P line has $J'' = 1.5$ and $J' = 0.5$. Thus the upper state has $\Omega = 1/2$ and the transition is ${}^2\Pi_{1/2}-{}^2\Pi_{1/2}$ in case (a) or $1/2-1/2$ in case (c).

Since the B''_3 and B''_4 are accurately determined the difference of these two is taken as approximate value for α''_e and B''_e was then deduced from the equation $B''_e = B''_3 - \alpha''_e (\nu''+1/2)$. Similarly B'_e was determined from $\sim \alpha'_e$ obtained from B'_{10} and B'_{11} . The B''_e and B'_e thus derived are given in Table IV. The I_e and r_e values for the upper and lower states are determined in the usual manner (Herzberg 1950) and are shown in Table IV.

FIG. 1. Enlargement of the 11-3 band of system I of Cl_2^+ showing the assignments of the rotational lines.

FIG. 2. Enlargement of the 11-4 band of system I of Cl_2^+ showing the assignments of the rotational lines.

FIG. 3. Enlargement of the 7-2 band of system III of Cl_2^+ showing the assignments of the rotational lines.

PLATE I

— λ —

21976.1 Cm^{-1}



21348.7 Cm^{-1}



21475.9 Cm^{-1}

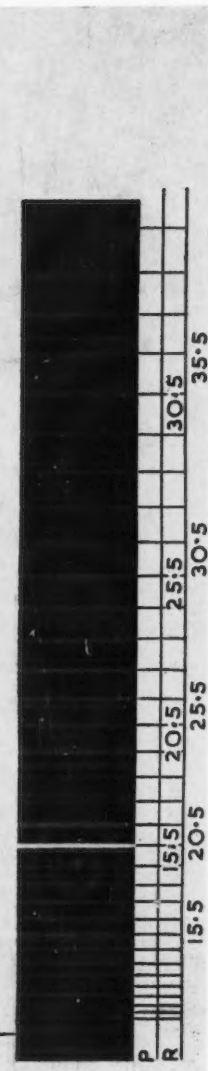


PLATE II

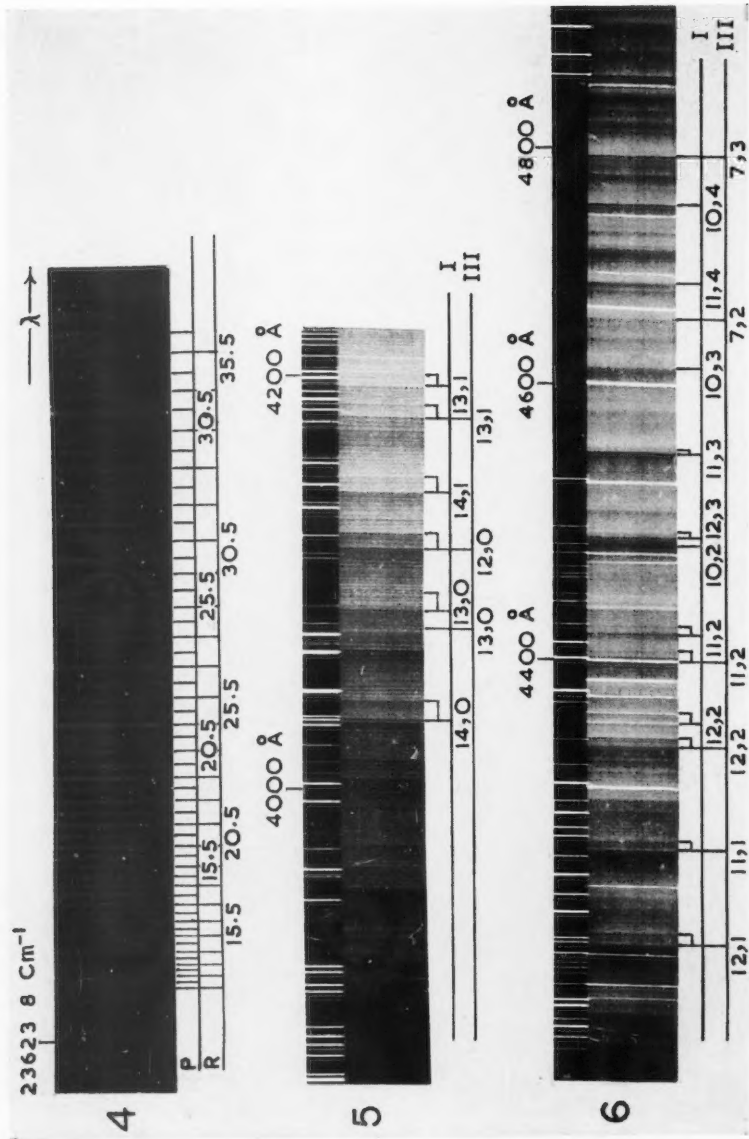


TABLE IV
CONSTANTS FOR SYSTEM I IN CM⁻¹

	Lower state	Upper state
B_s	0.271 ₆	0.193 ₃
α_s	0.0017	0.0017
I_e	103.01×10^{-40} g/cm ²	144.73×10^{-40} g/cm ²
r_e	1.884 Å	2.233 Å

System III

In this system the bands 11-1, 12-1, 13-1, 7-2, 11-2, and 12-2 at 23327, 23624, 23925, 21476, 22694, and 22990 cm⁻¹, respectively, are found suitable for a rotational analysis. In the first three bands which have clearly separate *P* and *R* branches the *J* numbering is fixed by comparing the lower state combination differences. These are found to agree exactly within the accuracy of the present measurements, thus confirming that all three have a common lower level. Similarly the *J* numbering was fixed for 12-2, 11-2, and 7-2 bands and again good agreement was found.

Using the *J* numbering derived above it is found that the upper state combination differences for the pairs of bands 11-1, 11-2, 12-1, and 12-2 agree with each other. Of the six bands analyzed here the 11-1 and 11-2 bands belong to system I and 12-1, 12-2 belong to system II whereas the 13-1 and 7-2 bands are unclassified in EC's analysis.

Rotational Constants

The rotational constants for the upper and lower states of this system are summarized in Tables V and VI. As the 7-2 band has superposed *P* and *R*

TABLE V
THE BAND ORIGINS, B_v AND D_v VALUES IN CM⁻¹ FOR SYSTEM III

Band	v_0	B'	B''	D''
7-2	21475.40	0.175 ₄		
11-1	23326.75	0.169 ₄ *	0.267 ₀ *	$(0.29 \pm 0.04) \times 10^{-6}$ *
11-2	22693.10	0.169 ₄ *	0.265 ₃ *	$(0.17 \pm 0.04) \times 10^{-6}$ *
12-1	23623.38	0.169 ₆ *	0.267 ₀ *	$(0.29 \pm 0.04) \times 10^{-6}$ *
12-2	22989.61	0.169 ₆ *	0.265 ₂ *	$(0.17 \pm 0.04) \times 10^{-6}$ *
13-1	23924.60	0.166 ₂	0.267 ₀ *	$(0.29 \pm 0.04) \times 10^{-6}$ *

*Determined from the averages of combination differences, D' is negligibly small.

branches throughout the B''_2 and D''_2 were determined from the 11-2 and 12-2 bands only. The constants B'_2 , B'_{11} , and B'_{12} can be fitted into the equation

$$B'_v = 0.1878 - 0.0016 (v' + 1/2)$$

FIG. 4. Enlargement of the 12-1 band of system III of Cl₂⁺ showing the assignments of the rotational lines.

Figs. 5 and 6. Fuess spectrograms of Cl₂⁺ showing the prominent bands of systems I and III.

showing that B'_e is linear in v . The values of B'_{12} shown in Table V calls for comment. It is almost equal to the B'_{11} . This irregularity may probably be done because of perturbations by the various excited electronic states which cross the upper potential curve.

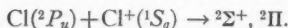
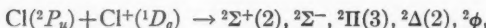
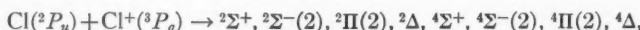
TABLE VI
CONSTANTS FOR SYSTEM III IN cm^{-1}

	Lower state	Upper state
B_e	0.269 ₅	0.187 ₈
α_e	0.0017	0.0016
I_e	$103.81 \times 10^{-40} \text{ g/cm}^2$	$149.00 \times 10^{-40} \text{ g/cm}^2$
r_e	1.891 Å	2.266 Å

The 7-2 band reproduced in Fig. 3 shows $P(2.5)+R(6.5)$ line on the long wavelength side of ν_0 . There is a clear gap between this line and ν_0 , the band origin. This may be taken as an indication that the first line has $J'' = 2.5$ and $J' = 1.5$. Thus the upper state has $\Omega = 3/2$ and the transition is ${}^2\Pi_{3/2}-{}^2\Pi_{3/2}$ in case (a) or $3/2-3/2$ in case (c).

POTENTIAL ENERGY CURVES AND DISSOCIATION PRODUCTS

Using the constants B_e , D_e , ω_e , and r_e for the upper and lower states derived from vibrational and rotational analyses of systems I and III the potential energy curves are drawn employing the Morse function. These curves are shown separately for systems I and III in Figs. 7 and 8. For deriving the low lying electronic states of Cl_2^+ from the states of the separate atoms Cl and Cl^+ , we may limit ourselves to the consideration of the three combinations $\text{Cl}(^2P_u) + \text{Cl}^+(^3P_g)$, $\text{Cl}(^2P_u) + \text{Cl}^+(^1D_g)$, and $\text{Cl}(^2P_u) + \text{Cl}^+(^1S_g)$. These combinations will give rise to the following states according to the Wigner-Witmer correlation rules



On the basis of electron configurations discussed later, the lower ${}^2\Pi$ states of systems I and III are regarded as ${}^2\Pi_{1/2}g$ and ${}^2\Pi_{3/2}g$ arising from the configuration $\sigma_g^2 \pi_u^4 \pi_g^3$. Since the ground state is expected to be an inverted ${}^2\Pi$, it is reasonable to assume that the ${}^2\Pi_{3/2}$ state, the lower state of system III dissociates into $\text{Cl}(^2P_{3/2}) + \text{Cl}^+(^3P_2)$ while the ${}^2\Pi_{1/2}$ state, the lower state of system I, dissociates into either $\text{Cl}(^2P_{3/2})$ or $(^2P_{1/2}) + \text{Cl}^+(^3P_2)$ (or 3P_1 or 3P_0).

The ${}^2\Pi$ lower state of systems I and III can be correlated unambiguously with one of the ${}^2\Pi$ states arising from $\text{Cl}(^2P_u) + \text{Cl}^+(^3P_g)$. The upper states of these systems may be identified as ${}^2\Pi_{1/2}u$ and ${}^2\Pi_{3/2}u$ of configuration $\sigma_g^2 \pi_u^3 \pi_g^4$. For the dissociation products of the upper states of systems I and III

only two possible combinations need be considered, namely $\text{Cl}({}^2P_u) + \text{Cl}^+({}^1D_g)$ and $\text{Cl}({}^2P_u) + \text{Cl}^+({}^1S_g)$. The latter possibility can easily be ruled out in each case as it will lead to values of dissociation energies of the lower states which are smaller than some of the observed vibrational levels of these states. The excited ${}^2\Pi_{1/2}$ and ${}^2\Pi_{3/2}$ states of systems I and III dissociate therefore into $\text{Cl}({}^2P_u) + \text{Cl}^+({}^1D_g)$. This is clearly illustrated in Figs. 7 and 8 for systems I and III respectively. Experimentally it will not be possible to reach an unambiguous decision as to whether the Cl atom is produced in the ${}^2P_{3/2}$ or ${}^2P_{1/2}$ state. However, there is some evidence from a consideration of the

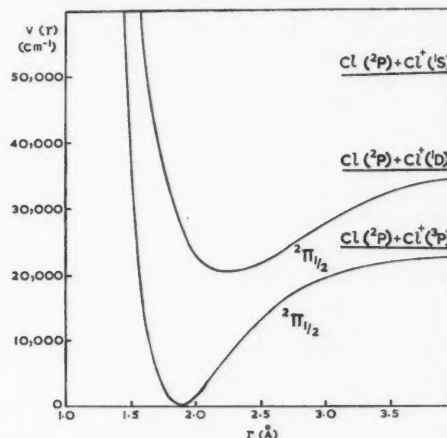


FIG. 7. Potential energy curve, system I.

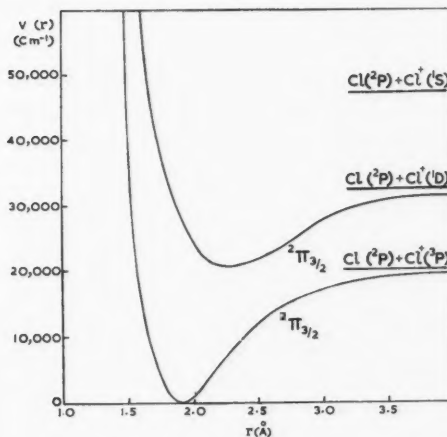


FIG. 8. Potential energy curve, system III.

bands 10-2, 11-2, and 12-2 shown in Table VII that the $^2\Pi$ interval in the upper state shows a decrease with increasing vibrational quantum number. If this interval decreases to zero as the dissociation limit is approached then the two components dissociate into $\text{Cl}(^2P_{3/2}u) + \text{Cl}^+(^1D_g)$. Theoretical evidence outlined by Mulliken (1928a, 1928b, 1930a, and 1930b) in a series of papers and discussed by Durie and Ramsay (1958) for analogous $^2\Pi$ upper state in ClO shows that the halogen atom is probably produced in the $^2P_{3/2}$ state.

TABLE VII

Classification, $v' v''$	System III, cm^{-1}	System I, cm^{-1}	$\Delta\nu$, cm^{-1}
10-2	22390	22301	89
11-2	22694	22610	84
12-2	22990	22914	76
13-0	24562	24485	77

From the dissociation products indicated above for system III it is possible to derive the dissociation energy of the lower state $^2\Pi_{3/2}g$, which is probably the normal state of Cl_2^+ . An estimate of the dissociation energy of this state can be made in one of the two ways. (i) By means of a Birge-Sponer extrapolation of the observed vibrational levels in the upper state. Applying the equation $D_e = \omega_e^2/4x_e\omega_e$ for the upper state we obtain a value of 15094 cm^{-1} . If we assume that this value is 20% high the true value of D of upper state is obtained as 12075 cm^{-1} . If we now add this value to the ν_e value of system III and subtract $^1D-^3P_2$ excitation energy of the Cl^+ atom (from Moore's tables, 1949) we obtain $D'_e = 20992 \text{ cm}^{-1}$ or 2.60 ev. (ii) The value of D''_e can also be determined directly from a Birge-Sponer extrapolation of the observed vibrational levels of the lower state. This is obtained as 2.42 ev. If we assume that this value is 10% high, it is seen to agree closely with the indirectly determined value (2.23 ev) of the energy of dissociation D of the normal state of Cl_2^+ .

ELECTRONIC TRANSITIONS IN Cl_2^+

Since Cl_2^+ is isoelectronic with ClO it is reasonable to expect the same electron configuration and term type for the ground state. Following Mulliken's notation (1932) this may be written as

$$(z\sigma)_g^2 (y\sigma)_u^2 (x\sigma)_g^2 (w\pi)_u^4 (v\pi)_g^3, ^2\Pi_{t(g)}$$

The first excited state as in ClO may also be derived from

$$(z\sigma)_g^2 (y\sigma)_u^2 (x\sigma)_g^2 (w\pi)_u^3 (v\pi)_g^4, ^2\Pi_{t(u)}$$

The transition from the excited state to the ground state is of the $^2\Pi_t-^2\Pi_t$ type giving rise to $^2\Pi_{1/2}-^2\Pi_{1/2}$ and $^2\Pi_{3/2}-^2\Pi_{3/2}$ components representing systems I and III respectively. The transition of an electron from the bonding $w\pi$ orbital to the corresponding antibonding $v\pi$ orbital should be accompanied by a considerable reduction in the vibrational frequency. This is consistent with the observed fact that ω_e value decreases from 655 to 348 cm^{-1} . A similar

decrease in the vibrational frequency is also observed in the case of a similar transition in ClO (viz. 868 to 557 cm⁻¹). The increase in vibrational frequency from 565 to 655 cm⁻¹ of the normal states of Cl₂ and Cl₂⁺ is also consistent with the fact that the electron removed in the process of ionization of Cl₂ molecule belongs to the antibonding π_g orbital.

The coupling constant '*A*' for each of the above $^2\Pi$ states is expected to be intermediate between the atomic coupling coefficients '*a*' of Cl and Cl⁺ atoms i.e., between 588 cm⁻¹ and 645 cm⁻¹ and may be taken as ~ 610 cm⁻¹. It is interesting to note that the pairs of bands in systems I and III shown in Table VII are separated by a wavenumber interval varying between 89 and 76. This small separation indicates that the $^2\Pi$ interval in both the states is of the same order of magnitude as predicted theoretically. If the $^2\Pi$ interval in the lower state is greater than in the upper state then the $^2\Pi_{3/2}-^2\Pi_{3/2}$ system is expected on the short wavelength side of the $^2\Pi_{1/2}-^2\Pi_{1/2}$ component system as observed. However, for the two component systems in ClO the situation is slightly different as the $^2\Pi_{1/2}-^2\Pi_{1/2}$ component occurs on the short wavelength side of the $^2\Pi_{3/2}-^2\Pi_{3/2}$ component. This implies that in ClO the $^2\Pi$ interval in the lower state is smaller than that in the upper state.

The B_e values for upper and lower states of the two components systems as obtained from the present analysis are somewhat different from each other. If Hund's case (*a*) strictly holds both for the upper and lower states they should be equal. If, however, there is a departure towards case (*b*) because of spin uncoupling, then the derived B_e values should be regarded as B_{eff} values where

$$B_{eff} = B(1 \pm B/A \text{ Å})$$

where *B* is the true value and the + sign refers to the $^2\Pi_{1/2}$ component. The B_{eff} values differ by the amount $2B^2/A$ Å. For the lower $^2\Pi$ state this difference would be about 0.0002 if *A* is assumed to be ~ 610 and *B* is taken as the mean of two B_{eff} values. The observed B_{eff} values for the lower state differ by as much as 0.0021. This discrepancy can be explained only if we assume that the coupling in the lower state shows a tendency towards case (*c*) rather than case (*b*). A similar discrepancy for the upper state also points to the conclusion that the coupling in this state also shows a tendency towards case (*c*). It is not unreasonable to expect case (*c*) coupling in both the states when doublet intervals of the order of 610 cm⁻¹ are expected. Hence systems I and III may better be represented as case (*c*) 1/2-1/2 and 3/2-3/2 transitions respectively.

In conclusion the authors would like to express their deep indebtedness to Dr. G. Herzberg for his interest in the work and for the contribution of some castings and blue print of his mount to Prof. K. R. Rao, which were used in the setup of the 21-ft concave grating spectrograph. One of the authors (V.V.) is grateful to Prof. S. T. Krishnaswamy Chetty for his valuable guidance and advice in setting up the grating. The authors' thanks are due to Prof. R. S. Mulliken and Prof. K. R. Rao for their interest in this work.

REFERENCES

- DURIE, R. A. and RAMSAY, D. A. 1958. Can. J. Phys. **36**, 35.
ELLIOT, A. and CAMERON, W. H. B. 1937. Proc. Roy. Soc. A, **158**, 681.
——— 1938. Proc. Roy. Soc. A, **164**, 531.
HARANATH, P. B. V. and RAO, P. T. 1956. Current Sci. (India), **25**, 47.
HERZBERG, G. 1950. Spectra of diatomic molecules (D. Van Nostrand Company, Inc., Princeton, N.J.)
HOWELL, H. G. 1953. Proc. Phys. Soc. A, **66**, 759.
MOORE, C. E. 1949. Atomic energy levels, Vol. I. Circular of the National Bureau of Standards, 467, Washington.
MULLIKEN, R. S. 1928a. Phys. Rev. **32**, 186.
——— 1928b. Phys. Rev. **32**, 761.
——— 1930a. Phys. Rev. **36**, 1440.
——— 1930b. Revs. Modern Phys. **2**, 60.
——— 1932. Revs. Modern Phys. **4**, 1.
UCHIDA, Y. and OTA, Y. 1928. Jap. J. Phys. **5**, 53.

POLARIZATION FLUCTUATIONS IN A FERROELECTRIC CRYSTAL¹

R. E. BURGESS

ABSTRACT

The theory of thermal fluctuations of electrical polarization in a ferroelectric crystal is considered with special attention to temperatures in the neighborhood of the Curie point. Models giving a second-order transition are discussed thermodynamically, and the free energy with its derivatives yield the mean value and variance of dipole moment. The fluctuations and their spectral density are related respectively to the real and imaginary parts of the susceptibility of the crystal in conformity with Nyquist's theorem, which is not violated by the presence of a constant applied electric field. The g-r. theorem is shown to be applicable to equilibrium and non-equilibrium conditions, and its extension to lambda-point phenomena generally is discussed.

1. INTRODUCTION

In an ideal gas the variance of the number N of particles in a small sub-volume V of a large enclosure is equal to the average number of particles. This result, which is essentially a consequence of probabilistic considerations, requires modification in a real gas to take into account the molecular interactions. If this is done thermodynamically (Fowler 1936) then to a high approximation the variance may be expressed in terms of the isothermal compressibility K of the gas which appropriately represents these interactions for the purposes of fluctuation analysis:

$$(1) \quad \text{var } N = -\frac{N^2 k T}{V^2 (\partial p / \partial V)_T} = \frac{N^2 K k T}{V}.$$

Under normal conditions this variance is still of the order of N and the distribution of N is gaussian. In the Appendix the variance is evaluated for various forms of the equation of state. However, near a critical point (e.g. the gas-liquid critical point) the compressibility becomes very large and in fact the first and second derivatives $\partial p / \partial V$ and $\partial^2 p / \partial V^2$ vanish simultaneously at this point and $\partial^3 p / \partial V^3$ determines the fluctuations. In these conditions the fluctuations are greatly enhanced and the effect is visible as "critical opalescence" when light is scattered from the fluid.

The formula given above is no longer valid at the critical point where the third derivative $\partial^3 p / \partial V^3$ determines the fluctuations of N , which, instead of being of order N , are now of order $N^{3/2}$. Furthermore the distribution law for N is no longer gaussian but of the sharper form $\exp[-a(N-\bar{N})^4]$.

It is relevant to consider what form of critical fluctuations should be observable in solids. The lambda-point transitions which occur in ferroelectric crystals are particularly interesting since the macroscopic phenomenon is

¹Manuscript received August 13, 1958.

Contribution from the Department of Physics, University of British Columbia, Vancouver, B.C. The research for this paper was supported by the Defence Research Board of Canada under Grant No. 9512-22.

readily observed and the fluctuations may be detected electrically as spontaneous electromotive forces at electrodes attached to the crystal. Various classes of crystal exhibit spontaneous polarization over a certain range of temperature at whose upper limit there occurs a transition with a very large peak in permittivity and an associated specific heat anomaly. Since in at least some cases these transitions are second order (and also because lambda-point phenomena are of general interest in physics) we shall discuss the fluctuations which occur in the vicinity of second order transitions.

A specific model of dipole polarization will be considered to indicate the statistical background of the problem and a general thermodynamical discussion will be given which is independent of any specific model. Compliance of the fluctuations in thermal equilibrium with Nyquist's theorem is established implying, as expected, that enhancement of the dipole moment fluctuations around the Curie point must correspond to a peak in the dissipative part of the permittivity in the same temperature range. The application of a steady electric field modifies the average dipole moment and its fluctuations. An independent derivation is readily obtained from the author's "g-r. theorem" (Burgess 1955, 1956) by identifying the "generation" process with a dipole aligning itself parallel to the field and the "recombination" process with anti-parallel alignment; the kinetics of the change of alignment lead to the variance, relaxation time, and spectral density of the net dipole moment.

Although the relation between the macroscopic and fluctuation aspects of a second order transition is discussed in the specific terms of a ferroelectric crystal, it can be extended to other cases where such phase transitions occur, e.g. in an AB alloy (such as CuAu) with long-range order, in liquid helium at the lambda point, or in a superconductor in the absence of a magnetic field. In all these processes co-operative effects are strongly acting to produce ordering below the critical temperature, and the degree of order decreases rapidly as this temperature is approached.

2. DIPOLE MODEL

Consider a crystal of volume V containing N identical dipoles all situated on equivalent sites with moment m which may be oriented either parallel or antiparallel with the applied uniform external field E . If at any instant, N_1 of the dipoles are in the parallel position we can introduce an order parameter x such that $N_1 = N(1+x)/2$ and $N - N_1 = N(1-x)/2$ corresponding to a net dipole polarization.

$$(2) \quad P = \frac{(2N_1 - N)m}{V} = nmx,$$

where $n = N/V$. The net dipole moment $M = PV = Nmx$.

In a real crystal, other sources of polarization may be present but these will be ignored in order to clarify the situation; this will be done justifiably since near the transition the dipole polarization will dominate over other forms in the present model.

The local electric field acting at each dipole is of the Weiss form

$$(3) \quad E' = E + \beta P,$$

where β is the Lorentz factor, which, however, does not need to be given the value $4\pi/3$ but simply expresses the linear dependence of the local field on the polarization.

The internal energy is

$$U = -V \int_0^P E' dP = -VEP - \frac{1}{2}V\beta P^2,$$

which represents the work done in orienting the dipoles in the presence of the local field.

The entropy of the configuration is

$$S = k \ln \frac{N!}{N_1!(N-N_1)!},$$

and the free energy is

$$(4) \quad F = U - TS \\ = -V \left(EP + \frac{\beta P^2}{2} \right) - kNT \ln 2 + \frac{kNT}{2} \\ \times [(1+x) \ln (1+x) + (1-x) \ln (1-x)],$$

where Stirling's theorem has been applied to the factorials. The condition of equilibrium is obtained by minimizing the free energy with respect to the dipole moment.

$$(5) \quad 0 = \left(\frac{\partial F}{\partial M} \right)_{E,V,T} = -(E + \beta P) + \frac{kT}{m} \tanh^{-1} x$$

giving

$$(6) \quad x = \tanh \frac{mE'}{kT} = \tanh \frac{m(E + \beta nm x)}{kT}.$$

This equilibrium condition is equivalent to the Boltzmann ratio for the populations of the parallel and antiparallel states:

$$(7) \quad \frac{N_1}{N-N_1} = \frac{1+x}{1-x} = \exp \frac{2mE'}{kT}.$$

It is readily deduced that the critical temperature, which is the upper bound of T for a non-zero root of this equation to exist when $E = 0$, is given by

$$(8) \quad T_c = \frac{\beta nm^2}{k}.$$

When $E = 0$ the spontaneous polarization P_s when $T < T_c$ is given by

$$(9) \quad \frac{P_s}{nm} = \tanh \left(\frac{P_s T_c}{nm T} \right).$$

Just below the Curie point

$$(10) \quad x = \frac{P_s}{nm} \simeq \pm 3^{\frac{1}{2}} \left(\frac{T_c}{T} - 1 \right)^{1/2}.$$

The susceptibility X is appropriately defined as dP/dE rather than P/E since this removes the effect of the spontaneous polarization below the Curie point and furthermore the differential coefficient is required in fluctuation problems to relate the small variations of P and E around the average values.

Now the reciprocal of the susceptibility is

$$(11) \quad \frac{1}{X} = \left(\frac{dE}{dP} \right) = \beta \left[\frac{T}{T_c(1-x^2)} - 1 \right],$$

which is positive above and below the Curie point. In the region of T_c there are two forms for the zero-field values:

$$(12) \quad T > T_c \quad 1/X = \beta(T-T_c)/T_c,$$

$$(13) \quad T < T_c \quad 1/X = 2\beta(T_c-T)/T_c.$$

This model gives polarization and entropy which are continuous through the Curie temperature although their derivatives are discontinuous, characteristic of a second order transition.

In discussing the thermodynamical aspects of the transition and the thermal fluctuations of polarization it is necessary to have the first four derivatives of free energy with respect to dipole moment at the equilibrium value and for constant E , V , and T :

$$(14a) \quad \frac{\partial F}{\partial M} = 0,$$

$$(14b) \quad \frac{\partial^2 F}{\partial M^2} = \left[-\beta + \frac{\beta T}{T_c(1-x^2)} \right] \frac{1}{V} = \frac{1}{XV},$$

$$(14c) \quad \frac{\partial^3 F}{\partial M^3} = \frac{2x\beta T}{nmT_c(1-x^2)^2 V^2},$$

$$(14d) \quad \frac{\partial^4 F}{\partial M^4} = \frac{2\beta T}{(nm)^2 T_c V^3} \frac{(1+3x^2)}{(1-x^2)^3}.$$

In the absence of an applied electric field the transition occurs with $x = 0$, which implies that at the critical point

$$(14e) \quad \frac{\partial^2 F}{\partial M^2} = 0 = \frac{\partial^3 F}{\partial M^3}, \quad \frac{\partial^4 F}{\partial M^4} > 0$$

3. FLUCTUATIONS

3.1 Total Fluctuations

The total mean square fluctuation of the dipole moment can be determined from the free energy function. If we expand F about the equilibrium value

$$(15) \quad F - F_0 = (1/2)(M - M_0)^2 \frac{\partial^2 F}{\partial M^2} + \frac{(M - M_0)^3}{6} \frac{\partial^3 F}{\partial M^3} + \frac{(M - M_0)^4}{24} \frac{\partial^4 F}{\partial M^4} + \dots,$$

where the suffix zero denotes the mean value in equilibrium. We see that so long as $\partial^2 F / \partial M^2$ does not vanish we have for small fluctuations

$$(16) \quad F - F_0 = (1/2)(M - M_0)^2 \partial^2 F / \partial M^2.$$

Now

$$(17) \quad W(M)dM = W_0 \exp\left(-\frac{F-F_0}{kT}\right) \cdot dM$$

is the form of the probability distribution function which implies that M has a gaussian distribution about M_0 with variance

$$(18) \quad \text{var } M = \overline{(M-M_0)^2} = kTXV = \frac{kT_e V}{\beta \left[\frac{1}{1-x^2} - \frac{T_e}{T} \right]}.$$

This fluctuation of polarization will manifest itself as a fluctuation of potential difference v between electrodes applied to the crystal. In the next section these observable fluctuations will be related to the dipole moment fluctuations.

The expressions above for fluctuations are valid whether the temperature of the crystal is above or below the Curie temperature (but not too near to it) and also in the presence of a steady electric field E . The potential difference fluctuation corresponds to the classical equipartition formulation applied to the electrostatic energy of the crystal, as might be expected from equation (7).

A generalization of the preceding arguments is readily achieved such that quite general dependences of the internal energy and the entropy on the order parameter will still lead to the equipartition result for the total fluctuations.

Thus, writing the free energy in its most general functional dependence on the applied electric field E and the dipole moment M :

$$F = U(E, M) - kTS(M)$$

gives, for the equilibrium condition $M = M_0$,

$$U'(E, M_0) = kTS'(M_0),$$

where prime denotes partial differentiation with respect to M .

The susceptibility X is found from the variation of P with an infinitesimal change of E while equilibrium is maintained:

$$\frac{\partial U'(E, M_0)}{\partial E} + U''(E, M_0) \frac{\partial M_0}{\partial E} = kTS''(M_0) \frac{\partial M_0}{\partial E}$$

or

$$X = \frac{1}{V} \frac{\partial M_0}{\partial E} = -\frac{\partial U'(E, M_0)/\partial E}{F''(M_0)} = \frac{1}{VF''(M_0)}.$$

Thus $\text{var } M = kT/F''(M_0) = kTXV$, demonstrating the general validity of equation (18) under non-critical conditions where $F''(M_0)$ does not vanish.

Just as higher derivatives need to be taken into account in considering critical point fluctuations in gases, so in the ferroelectric we need to consider additional terms in the development of the free energy or electric field in terms of P . As a first approximation, near to but not at the Curie point, we

have from (14b), (12), and (13) for the dipole moment fluctuations in the absence of an applied electric field:

$$(19) \quad \overline{M^2} = \frac{kTVT_c}{\beta(T-T_c)} = \frac{Nm^2T}{T-T_c}, \quad T > T_c$$

$$(20) \quad \overline{(M-M_0)^2} = \frac{kTVT_c}{2\beta(T_c-T)} = \frac{Nm^2T}{2(T_c-T)}. \quad T < T_c$$

These expressions indicate that the dipole fluctuations have a pronounced maximum (theoretically infinite in the first approximation) at $T = T_c$ when $E = 0$. This infinity is removed by going to the fourth derivative, as the first three all vanish; since $\partial^4 F / \partial M^4 = 2\beta/nm^2NV^2$ we find that

$$(21) \quad W(M) = W_0 \exp\left(-\frac{M^4}{12N^3m^4}\right).$$

This is not a gaussian distribution and gives a dipole moment variance

$$(22) \quad \overline{M^2} = 1.17 N^{3/2} m^2,$$

which implies that in a crystal having $N \gg 1$ the fluctuations of dipole moment given by (19) can be used at temperatures quite close to the Curie point.

The mean internal energy due to fluctuations of the total dipole moment about zero above the Curie temperature is

$$(23a) \quad \overline{U} = \frac{\beta \overline{M^2}}{2V} = \frac{kT_c T_e}{T-T_c}, \quad T > T_c$$

$$(23b) \quad = 1.17 N^{1/2} kT_c. \quad T = T_c$$

In terms of number fluctuations, the variance of the number N_1 of dipoles oriented parallel to the field is found from

$$(24) \quad \text{var } N_1 = \text{var } M/4m^2 = 0.29 N^{3/2},$$

which illustrates the tendency of critical fluctuations to be of order $N^{3/2}$ rather than of order N .

The mean fourth power fluctuations of M and N_1 are also of interest for the type of distribution given by equation (21):

$$(25) \quad \overline{M^4} = 3N^3m^4 \quad \text{or} \quad \overline{N_1^4} = 3N^3/16,$$

which gives for the increment of free energy due to fluctuations around the critical point:

$$(26) \quad \bar{F} - F_0 = kT_c/4$$

in contrast with the value $kT/2$ when normal quadratic fluctuations occur.

Some reservations about the results obtained at the Curie point should be mentioned. The representation of the long-range co-operative action of the dipoles by a parameter β requires reexamination at the Curie point since localized interactions will tend to predominate. This is evident in the macroscopic properties of ferroelectrics and so far there seems to be no theory which

predicts a finite value for the permittivity at the Curie point, and furthermore the occurrence of domains of alternating polarities represents a complexity in the interaction.

When the crystal is not near the critical temperature the proportionality of the variance of the dipole moment M with the volume V (equation 18) implies that this formula is valid for each subvolume of the crystal and that the fluctuations in all elements are independent and additive. Near the Curie point covariance becomes important and the model used is inadequate because of the need to include a distance-dependent correlation between the fluctuations in any two elements. Landau has suggested (Frenkel 1946) that this may be represented by including a term in $|\text{grad } P|^2$ in the energy density associated with the polarization. Since there is no satisfactory model for this case our remarks will remain qualitative; it will be noted likewise that the finite maximum of the susceptibility at the Curie temperature is not predicted by existing theory.

3.2 Spectral Density of Fluctuations

Since in thermal equilibrium the fluctuations obey Nyquist's theorem we may readily deduce their spectral density in terms of the dissipative part of the susceptibility. At frequency f the admittance of a parallel plane crystal of area A and thickness L is

$$Y(f) = \frac{j\omega A}{L} \left[\frac{1}{4\pi} + X(f) \right] = \frac{j\omega A}{L} \left[\frac{1}{4\pi} + X' - jX'' \right]$$

where $X(f) = X' - jX''$ is the complex susceptibility at f . Hence the spectral density of the fluctuation potential difference is

$$(27) \quad S_v(f) = 4kT \frac{G(f)}{|Y(f)|^2} = 4kT \frac{\omega X'' A}{L |Y|^2}$$

and the spectral density of the short-circuit current fluctuations is

$$(28) \quad S_i(f) = 4kT(\omega X'' A/L)$$

and thus the fluctuations of dipole moment are

$$(29) \quad 4m^2 S_{N_1}(f) = S_M(f) = \frac{L^2 S_i(f)}{\omega^2} = \frac{4kT X'' V}{\omega}$$

When integrated over all frequencies this correctly leads to the earlier expression (18) for the total moment fluctuations:

$$\text{var } M = \int_0^\infty S_M(f) df = 4kTV \int_0^\infty \frac{X''}{\omega} df = kTVX$$

using the Kronig-Kramers relation and noting that the susceptibility X defined earlier as dP/dE is synonymous with the low frequency limit of the real part $X'(0)$ of the complex susceptibility.

These results indicate that measurements of fluctuations of polarization in a ferroelectric crystal give no more information about the internal co-operative and relaxation mechanisms than would measurements of the complex sus-

ceptibility of the crystal. The peak in $X''(f)$ near the Curie temperature will give rise to a proportional peak in the fluctuation current measured in a narrow band at frequency f . If the dissipative mechanism can be characterized by a polarization relaxation time τ , then under conditions where the order parameter x is small compared with unity (so that P is a linear function of E , and E' can be regarded as the driving force) the complex susceptibility is for $T > T_c$:

$$(30) \quad X(f) = \frac{T_c/\beta}{T(1+j\omega\tau)-T_c} = \frac{T_c}{\beta} \frac{(T-T_c)-j\omega\tau T}{(T-T_c)^2 + (\omega\tau T)^2}.$$

Thus the peak of X'' as the temperature is taken through T_c should be most pronounced at low frequencies where $\omega\tau \ll 1$.

For this model the spectral density of the dipole moment fluctuations is

$$(31) \quad S_M(f) = \frac{4kT^2 T_c V/\beta}{(T-T_c)^2 + (\omega\tau T)^2}.$$

The fluctuations observed electrically will depend on whether the measurement circuit to which the crystal is connected has a lower or higher impedance than the crystal. The variation with temperature will also be determined by the variation of τ , which is related to the tangent of the loss angle of the dielectric:

$$(32) \quad \tan \delta = \frac{X''}{X'} = \frac{\omega\tau T}{T-T_c} = \omega\tau_0$$

where τ_0 is the spectral relaxation time appropriate to the representing of the spectra of i , M , P , or N_1 in the form $(1+\omega^2\tau_0^2)^{-1}$.

The equivalent circuit which represents the admittance of the ferroelectric crystal and its fluctuation properties consists of the vacuum capacitance $C_0 = A/4\pi L$ in parallel with a series combination of the dipole capacitance $C_d = AX(0)/L$ and the loss resistance $R = L\beta T\tau/AT_c$. The spectral density of the potential difference fluctuations at the terminals of the system is

$$(33) \quad S_v(f) = \frac{4kTR}{(1+C_0/C_d)^2 + (\omega C_0 R)^2},$$

$$= \frac{4kT^2 \beta \tau L / AT_c}{\left[1 + \frac{\beta(T-T_c)}{4\pi T_c}\right]^2 + \left[\frac{\omega\beta T\tau}{4\pi T_c}\right]^2}.$$

Thus as $\beta \ll 4\pi/3$ is usually true in ferroelectrics (Jaynes 1953) it is seen that the major change in $S_v(f)$ as T passes through T_c will be due to the change of τ with temperature.

The total fluctuations of potential difference integrated over all frequencies can be related to the dipole moment fluctuations:

$$\bar{v^2} = \frac{kTC_d}{C_0(C_0+C_d)} = \left(\frac{4\pi}{A}\right)^2 \frac{\bar{M^2}}{\epsilon(0)}$$

where $\epsilon(0)$ is the zero frequency permittivity of the crystal.

3.3 Application of the g-r. Theorem to Polarization Fluctuations

It has been shown (Burgess 1955, 1956) that if a reversible reaction $A \leftrightarrow B$ in the most general sense is proceeding such that the state of the system can be specified by a number variable y (e.g. number of particles in state A) then if $g(y)$ is the rate at which the reaction tends to increase y , while $r(y)$ is the rate at which it tends to decrease y , such that $dy/dt = g - r$, the steady state is given by

$$(34) \quad g(y_0) = r(y_0)$$

and the mean square fluctuation of y about the mean value y_0 is given by

$$(35) \quad \text{var } y = \frac{g(y_0)}{r'(y_0) - g'(y_0)} = \left[\left(\frac{d}{dy} \ln \frac{g}{r} \right) y = y_0 \right]^{-1}$$

where the prime denotes differentiation with respect to y .

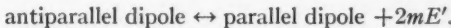
The relaxation time for the reaction, defined in terms of the return to the steady state after a slight perturbation, is given by:

$$(36) \quad \tau_0 = \frac{1}{r'(y_0) - g'(y_0)} = \frac{\text{var } y}{g(y_0)}$$

corresponding to a spectral density of the fluctuations in y given by

$$(37) \quad S_y(f) = \frac{4 \text{ var } y}{1 + \omega^2 \tau_0^2}.$$

These results have been applied to generation and recombination processes involving mobile carriers and ions in semiconductors. However, they are of much wider applicability and can be used to discuss diffusional processes, photon fluctuations, and order-disorder phenomena. We will now apply it to the dipole polarization problem by identifying the variable y with the number N_1 of dipoles oriented parallel to the field, and consider the "reaction"



We would then write g and r in the forms

$$(38a) \quad g(N_1) = \gamma(N - N_1) \exp - \frac{(\epsilon - mE')}{kT},$$

$$(38b) \quad r(N_1) = \gamma N_1 \exp - \frac{(\epsilon + mE')}{kT},$$

where γ is a constant and ϵ is the height of the potential barrier between the two positions.

It is evident from earlier work on the g-r. representation that only the ratio g/r is important in determining the moments of the variable under consideration. Thus the parameters γ and ϵ are not relevant for the moments of N_1 although they are important in determining the rate at which the process proceeds and hence the relaxation time and spectral density.

It is seen that g and r depend on N_1 directly and also indirectly through E' , which is linearly related to N_1 . This feature is the consequence of the

co-operative manner in which the state of the crystal as a whole determines the transition probabilities of any one dipole between the parallel and anti-parallel states. The logarithm of r/g is related to the change of free energy when one dipole is reversed from the antiparallel to the parallel position:

$$\frac{dF}{dN_1} = kT \ln \frac{r}{g} = -\frac{2mE'}{kT} + kT \ln \frac{N_1}{N-N_1} = -\frac{2mE}{kT} - \frac{2T_e x}{T} + kT \ln \frac{1+x}{1-x}$$

and this quantity is zero in equilibrium ($r = g$).

The derivative of this expression is

$$\frac{d^2F}{dN_1^2} = kT \left(\frac{r'}{r} - \frac{g'}{g} \right) = \frac{4kT}{N} \left(\frac{1}{1-x^2} - \frac{T_e}{T} \right),$$

and this must be positive in an equilibrium state corresponding to a minimum of the free energy. This is seen to be the case since

$$\frac{1}{1-x^2} > \frac{\tanh^{-1}x}{x} = \frac{T_e}{T} + \frac{mE}{kTx}$$

and E/x is taken as positive corresponding to the crystal polarization having the same polarity as the applied electric field.

The spectral time constant given by equation (36) is now

$$\tau_0 = \frac{1}{2 \left(\frac{1}{1-x^2} - \frac{T_e}{T} \right)} \frac{\exp(\epsilon/kT)}{\gamma(1-x^2)^{1/2}}.$$

Thus by comparison with (32) it is seen that the τ_0 introduced there (for $x^2 \ll 1$) is related to τ by

$$\tau = \left(1 - \frac{T_e}{T} \right) \tau_0 = \frac{\exp(\epsilon/kT)}{2\gamma}.$$

The variance of N_1 is

$$(39) \quad \text{var } N_1 = \frac{N-N_1}{\frac{N}{N_1} - \frac{4\beta m^2}{V k T} (N-N_1)} = \frac{N/4}{\frac{1}{1-x^2} - \frac{T_e}{T}},$$

which is in agreement with the earlier equation (18) for the dipole moment fluctuations.

For comparison, if it had been naively assumed that the dipole statistics obeyed the binomial distribution corresponding to N Bernoulli "trials" with chance $(1+x)/2$ of "success" the variance of N_1 would have been $N(1-x^2)/4$. It is seen that it approaches this value for $T \gg T_e$ but that when T is only a few times T_e the thermal energies are not sufficient to override the co-operative effect (represented by β) which enhances the fluctuations considerably by a form of "positive feedback."

The g-r. theorem is based on statistical considerations and does not require thermodynamical equilibrium to obtain and consequently it can be used to determine the validity of free energy analysis when it is uncertain. As an

example the verification of (18) shows that whether or not a steady electric field is being applied to the crystal the variance is correctly given by this formula.

When the critical condition is approached, equation (35) no longer correctly gives the variance and it is necessary to go to higher derivatives of g and r just as it is for the free energy. In fact it may be shown quite generally that the free energy is related to g and r by

$$(40) \quad F - F_0 = kT \int_{y_0}^y \ln \left(\frac{r}{g} \right) dy,$$

whence

$$(41) \quad \frac{dF}{dy} = kT \ln \frac{r}{g},$$

which vanishes in the steady state where $r_0 = g_0$.

Thus

$$(42) \quad \left(\frac{d^2F}{dy^2} \right)_{y_0} = \frac{kT(r'_0 - g'_0)}{g_0},$$

$$(43) \quad \left(\frac{d^3F}{dy^3} \right)_{y_0} = \frac{kT}{g_0^2} [g'^2 - r'^2 + g_0(r''_0 - g''_0)],$$

$$(44) \quad \left(\frac{d^4F}{dy^4} \right)_{y_0} = \frac{kT}{g_0^3} [2(r'^3 - g'^3) + 3g_0(g'_0g''_0 - r'_0r''_0) + g_0^2(r'''_0 - g'''_0)].$$

Now at a symmetrical critical point where $r_0 = g_0$ and $r'_0 = g'_0$ it is readily seen that $r''_0 = g''_0$ must also hold because of the necessity for dy/dt to be an odd function of $(y - y_0)$ requiring the even derivatives of $(r - g)$ to vanish. Thus the critical point corresponds to contact of the second order of the two curves $g(y)$ and $r(y)$ occurring at a common point of inflection where the slope of both curves is zero. This demonstrates that the point is a region of relatively large fluctuations because the restoring force when y departs slightly from y_0 is small since the rate of the reaction depends on the cube of the disturbance:

$$(45) \quad \begin{aligned} dy/dt &= g(y) - r(y), \\ &= \frac{(y-y_0)^3}{6} (g'''_0 - r'''_0) + \dots \end{aligned}$$

From stability considerations it is clear then $r'''_0 - g'''_0$ must be positive. It is also seen that because of the cubic behavior it is impossible to accord a relaxation time to the reaction at the critical point. In this condition the probability distribution of y is given by

$$\frac{P(y)}{P(y_0)} = \exp \left[\frac{-(r'''_0 - g'''_0)(y - y_0)^4}{24 g_0} \right],$$

which is the analogue of the distribution in terms of free energy at a critical point (cf. equation 21).

These considerations relating to the higher derivatives of $(r-g)$ are directly related to the derivatives of the free energy and correspond to equations (14) at a critical point.

REFERENCES

- BURGESS, R. E. 1955. Proc. Phys. Soc. B, **68**, 661. 1956. B, **69**, 1020.
 FOWLER, R. H. 1936. Statistical mechanics (Cambridge, The University Press, London) Chap. 20.
 FRENKEL, J. 1946. Kinetic theory of liquids (Oxford at the Clarendon Press) Chap. 2.
 JAYNES, E. T. 1953. Ferroelectricity (Princeton Univ. Press, Princeton, N.J.).

APPENDIX

DENSITY FLUCTUATIONS IN AN IMPERFECT GAS JUST ABOVE THE CRITICAL POINT

An imperfect gas departs from the ideal gas (whose equation of state is $pV = NkT$) by virtue of intermolecular forces and the finite size of the molecules. Such a gas has a critical point (p_c , V_c , T_c) where

$$\frac{\partial p}{\partial V} = 0 = \frac{\partial^2 p}{\partial V^2}, \quad \frac{\partial^3 p}{\partial V^3} < 0$$

A little above the critical temperature we can take

$$\frac{\partial p}{\partial V} = \frac{\partial^2 p}{\partial V \partial T} (T - T_c).$$

The number N of molecules in a volume V will have a gaussian distribution with variance.

$$\text{var } N = \frac{N^2 k T}{-V^2 (\partial^2 p / \partial V \partial T) (T - T_c)},$$

and this will always be of the form: const. $NT/(T - T_c)$ where the constant is of order unity and is determined by the precise character of the "imperfection" of the gas.

(i) For the *van der Waals* equation of state

$$(p + a/V^2)(V - b) = NkT,$$

$$p_c = \frac{a}{27b^2}, \quad V_c = 3b, \quad NkT_c = \frac{8a}{27b},$$

$$\text{var } N = \frac{4}{9} \frac{NT}{T - T_c} = 0.444 \frac{NT}{T - T_c}.$$

(ii) *Berthelet's* modification of the van der Waals equation of state consists of replacing a by a'/T with the following result:

$$\text{var } N = \frac{2}{9} \frac{NT}{T - T_c} = 0.222 \frac{NT}{T - T_c}.$$

In both the van der Waals and the Berthelet equations the critical point parameter $NkT_c/p_c V_c = 8/3$, which is considerably below the values observed for real gases. Better agreement is given by:

(iii) Dieterici's equation

$$p(V-b) = NkT \exp(-a/NkTV)$$

for which

$$V_e = 2b, \quad p_e = \frac{a}{4b^2 e^2}, \quad NkT_e = \frac{a}{4b}$$

giving

$$NkT_e/p_e V_e = 3.695$$

and

$$\text{var } N = \frac{e^2}{4} \frac{NT}{T-T_e} = 1.84 \frac{NT}{T-T_e}.$$

The variation of the numerical constant with the equation of state demonstrates the sensitivity of the fluctuations to the form of the intermolecular forces, expressed through the compressibility. This is analogous to the susceptibility which, in the ferroelectric crystal, represents the effect at any one dipole of the polarization due to the other dipoles, and also directly enters into the magnitude of the fluctuations of the net dipole moment.

NOTES

MILLIMICROSECOND PULSES FOR CHECKING FAST TRANSIENT ANALYZERS¹

A. S. DENHOLM

INTRODUCTION

During a study of fast pulses generated by a corona discharge, a generator was needed which could produce a pulse with a rise time shorter than those of the discharge and of amplitude sufficient to give a satisfactory deflection on a high writing speed oscilloscope. By attenuating this pulse to the level of the comparatively small corona pulses being measured, and then amplifying it through the pulse measuring system, an indication of the minimum rise time of the system could be obtained.

The corona pulses which were being studied are the prime cause of radio interference from high voltage transmission lines, but not of television interference, which generally is traced to bad contacts, i.e. the sparking of small gaps. Apparently, the time for such gaps to change from nonconducting to conducting is very short, which is confirmed by experiments in this laboratory on the generation of step functions for checking the transient response of high voltage dividers (Creed 1958). The spark gap has been used to produce very fast pulses at the higher voltages (e.g. 20 kv, Fletcher 1949) and there is evidence that under certain modes of operation mercury relays produce fast pulses due to spark discharge as the contacts close (Lewis and Wells 1954). The above suggested that a very small gap could be used to generate fast pulses using comparatively low voltage which would need only conventional components.

CIRCUITRY

The circuit is shown in Fig. 1. When the hydrogen thyratron (T_2) is tripped, capacitor C discharges and a fast rising pulse is developed across the 100-ohm resistor. Coaxial cable (D) is charged through the 2-kilohm resistor to the voltage at which the small gap breaks down, whereupon the cable discharges through the 50-ohm resistor giving a rectangular pulse with a very fast rise and fall. The pulse duration is equal to twice the electrical length of the cable. After the cable has discharged, the gap extinguishes, the cable re-charges, and again the gap breaks down to produce another pulse. Pulses recur, as shown in Fig. 2, until the cable fails to charge to a voltage sufficient to break down the gap.

The relays in the circuit allow the generation of positive or negative pulses without resorting to components such as transmission line transformers. Negative impulses are the more usual output of the impulse generator circuit

¹Issued as N.R.C. No. 4909.

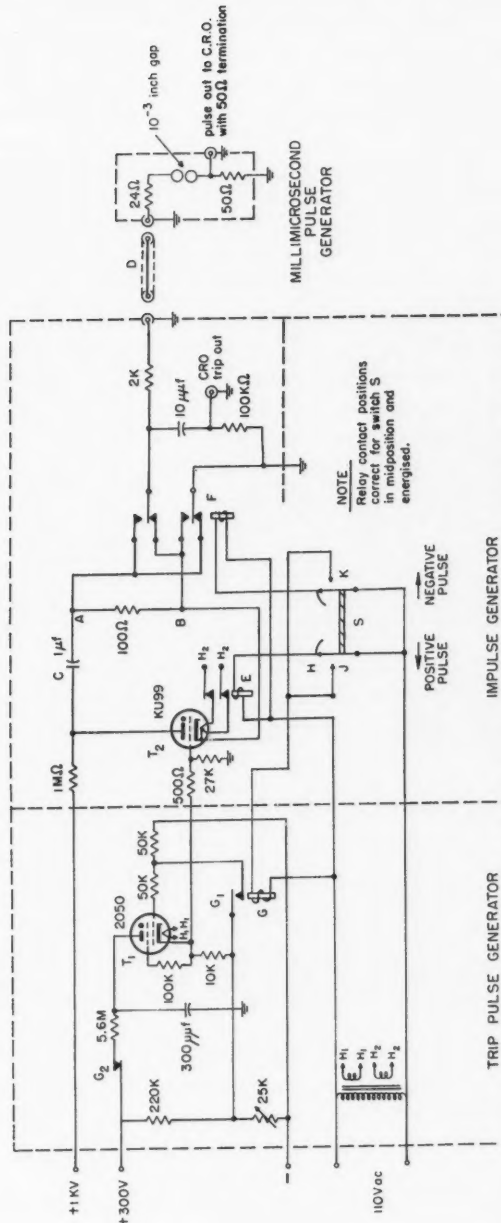


FIG. 1. Generator of positive or negative pulses of short duration (millimicroseconds).

of Fig. 1 and are given at point A when B is grounded. Grounding A and taking the output from B obviously gives a positive pulse, but the presence of the heater winding is usually unfortunate, if only because it introduces capacitance to ground which limits the rate of rise of voltage across AB. The circuit of Fig. 1 removes such effects by using the high thermal time constant of the hydrogen thyratron heaters. When a positive pulse is required, relay E opens the heater circuit just before the thyratron is fired and then closes it afterwards. Relay F operates as a reversing switch to give the desired output polarity.

Key S controls the operation of relays E, F, and G. Immediately the key is pushed to the left (positive pulse), contact H is broken, relay E is de-energized, and the heater of tube T_2 is isolated from its transformer. At the end of the key travel, contact is made at J, which initiates the tripping pulse for the hydrogen thyratron (T_2) by causing contact G_1 to close and remove the bias on tube T_1 . (Contact G_2 opens to ensure that only one tripping pulse occurs.) When the key is pushed to the right (negative pulse) F is de-energized to reverse the output connections before contact is made at K to fire T_2 .

PERFORMANCE

The rectangular pulse generated by the circuit is shown in Fig. 3. The rise time, as measured on the oscilloscope, is 1.5×10^{-9} seconds, but as this is close to the estimated time constant of the CRO plate system, the actual rise time of the pulse may be less than this. The fall time of the pulse is about 2.5×10^{-9} seconds. The steps on the top of the pulse seem to be due to the oscilloscope rather than the pulse generator.

The average time between the time base tripping and the first output pulse is 37×10^{-9} seconds, but the actual values are very inconsistent, apparently because of the performance of the gap, since the oscilloscope time base normally trips stably. Illuminating the gap with ultraviolet light gave no improvement. However, the time between the first pulse and the second was reasonably consistent (standard deviation, 5%) as was the amplitude of the second (standard deviation, 5.6% cf. first pulse, standard deviation, 9%), so that a relatively stable display of the second pulse may be obtained if the first pulse is used for time base triggering. It seems that the initial pulse conditions the gap in some way, perhaps by residual ionization, so that the state of the gap prior to each second pulse is essentially the same.

We hope to continue work in this field.

CONCLUSIONS

A simple circuit for generating millimicrosecond pulses has been given which uses only conventional components and two small spheres. It is expected that almost any electrode geometry would be satisfactory, as long as the gap was small.

Apart from its original purpose, which was for checking amplifiers and

PLATE I

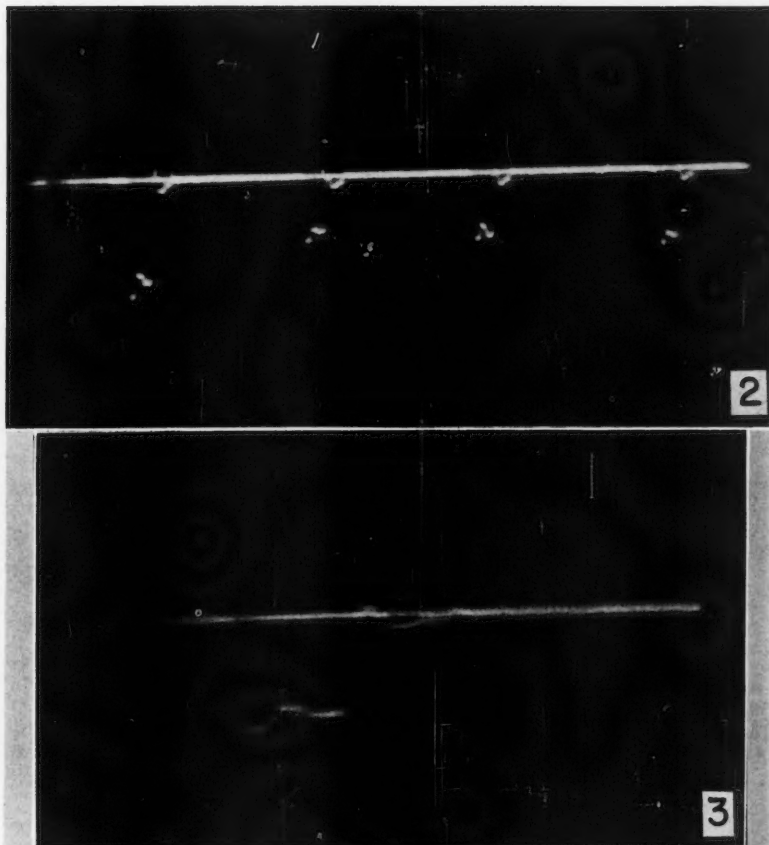


FIG. 2. Repetitive rectangular pulses generated by spark gap. Pulse duration, 24×10^{-9} seconds. Pulse amplitudes, No. 1—145 volts, No. 2—80 volts, No. 3—80 volts, No. 4—89 volts.

FIG. 3. Output pulse. Duration, 24×10^{-9} seconds. Amplitude, 125 volts.

194

circuitry, this generator circuit could be useful for the fast operation of electro-optical shutters such as the image converter.

The careful assistance of N. A. Lackey, who built the equipment and made the measurements of the generator performance, is gratefully acknowledged.

CREED, F. C. 1958. C.I.G.R.E. 320.

FLETCHER, R. C. 1949. Mass. Inst. Technol. Research Laboratory for Insulation Research, Tech. Rept. No. 20.

LEWIS, I. A. D. and WELLS, F. H. 1954. Millimicrosecond pulse techniques, 102. The Pergamon Press, Ltd., London.

RECEIVED AUGUST 6, 1958.

DIVISION OF RADIO AND ELECTRICAL ENGINEERING,
NATIONAL RESEARCH COUNCIL,
OTTAWA, CANADA.

A NEW TRANSITION IN MOLECULAR NITROGEN¹

P. K. CARROLL²

In the course of studying the $C^2\Sigma \rightarrow X^2\Sigma$ system of N_2^+ a new headless band with origin at 1589.745 Å was discovered. The source employed in the experiments was a hollow cathode discharge through pure nitrogen at low pressure. The excitation conditions were vigorous and the spectrum in the visible and ultraviolet regions was dominated by the first negative system and the $C^2\Sigma \rightarrow X^2\Sigma$ bands of N_2^+ . The new band was photographed in the fourth order of the three-meter vacuum spectrograph at the National Research Council of Canada. Details of the instrument and of the procedure employed are given in recent publications by Brix and Herzberg (1954) and Carroll (1956).

A reproduction of the new band is shown in Fig. 1. The zero gap can be located with certainty and the rotational analysis follows in a straightforward manner. The data for the new band are presented in Table I and by the usual graphical methods the analysis leads to the following constants:

$$\nu_0 = 62,903.18 \text{ cm}^{-1},$$

$$B' = 1.8644 \text{ cm}^{-1}, \quad D' = 7.1 \times 10^{-6} \text{ cm}^{-1},$$

$$B'' = 1.8801 \text{ cm}^{-1}, \quad D'' = 6.9 \times 10^{-6} \text{ cm}^{-1}.$$

At first sight the band appears to be a 0-0 transition, but the B values quoted above show that the $v = 0$ level of none of the many states of N_2 and N_2^+ for which B_0 values are known is involved. This raises the problem of identifying the transition.

¹Issued as N.R.C. No. 4930.

²National Research Council Postdoctorate Fellow, 1953-55. Present address: Physics Department, University College, Dublin, Ireland.

TABLE I
WAVE NUMBERS OF THE LINES OF THE NEW BAND

<i>N</i>	<i>P(N)</i>	<i>R(N)</i>	<i>N</i>	<i>P(N)</i>	<i>R(N)</i>
0		62907.47	20	22.23	74.64
1	62899.55	10.57	21	17.79	77.64
2	95.62	14.29	22	13.45	80.54
3	91.80	17.83	23	08.97	83.54
4	87.81	21.43	24	04.54	86.42
5	84.04	25.10	25	00.18	89.40
6	80.18	28.60	26	62795.55	92.18
7	76.20	32.14	27	91.15	98.21
8	72.24	35.59	28	86.55	97.65
9	68.26	38.97	29	81.85	63000.43
10	64.26	42.39	30	77.26	03.11
11	60.07	45.74	31	72.57	05.79
12	56.06	49.21	32	67.99	08.41
13	51.95	52.43	33	63.20	10.81
14	47.76	55.69	34	58.60	13.51
15	43.57	58.88	35	53.65	16.14
16	39.36	62.19	36	48.93	18.29
17	35.07	65.34	37	44.51	
18	30.83	68.44			
19	26.48	71.51			

The clear alternation of intensities leaves no doubt that the emitter is molecular nitrogen. The absence of any structure at the zero gap requires that Δ must be zero for both states. Furthermore, triplet states are not involved as no sign of spin splitting is detected, even at low *N* values. It therefore seems that the band must arise from a $^1\Sigma \rightarrow ^1\Sigma$ or $^2\Sigma \rightarrow ^2\Sigma$ transition. The fact that, in the intensity alternation, the lines of odd *N* values are the weaker ones shows that the lower state is either a Σ_g^+ or a Σ_u^- state.

It is very unlikely that the band is due to a transition between excited states of N_2 . If this were so the lower state could scarcely lie above 80,000 cm^{-1} as otherwise the upper state would lie at an improbably high energy. The lower level would also have to be metastable as it has not been observed in transitions to the ground state. On a consideration of molecular orbitals there seems to be only one state likely to satisfy these requirements, namely the $^1\Sigma_u$ state arising from the configuration $KK(\sigma_g 2s)^2 (\sigma_u 2s)^2 (\pi_u 2p)^3 (\sigma_g 2p)^2 (\pi_u 2p)$ (cf. Herzberg 1946). But this state is almost certainly the lower state of the fifth positive bands (cf. Gaydon 1944 and Lofthus 1956), which is definitely not the same as the lower state of the new transition. It therefore seems that the band cannot be assigned to N_2 . This is consistent with the experimental conditions which, as mentioned above, were such that ionized spectra were strongly favored.

In attempting to assign the band we will consider the following possibilities:

1. A transition between excited states of N_2^+ . To identify the lower state we consider the electron configuration of N_2^+ and again confine our attention to states which are not likely to have excessively high energy. The configuration: $KK(\sigma_g 2s)^2 (\sigma_u 2s)^2 (\pi_u 2p)^3 (\sigma_g 2p) (\pi_u 2p)$, which gives rise to two $^2\Sigma_u^+$, two $^2\Sigma_u^-$, and two $^2\Delta_u$ states is the only one likely to be of interest. One of the

PLATE I

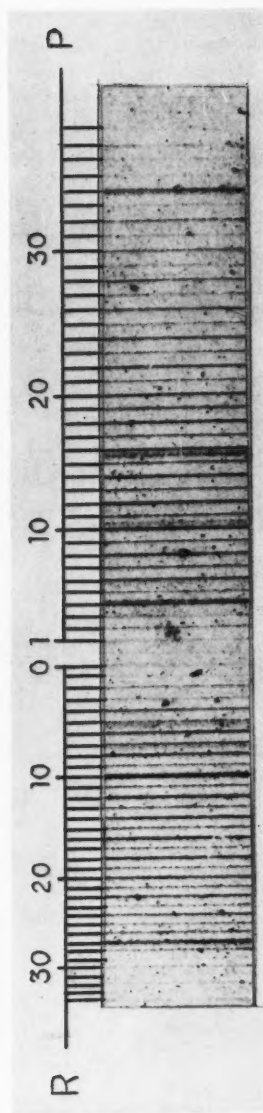
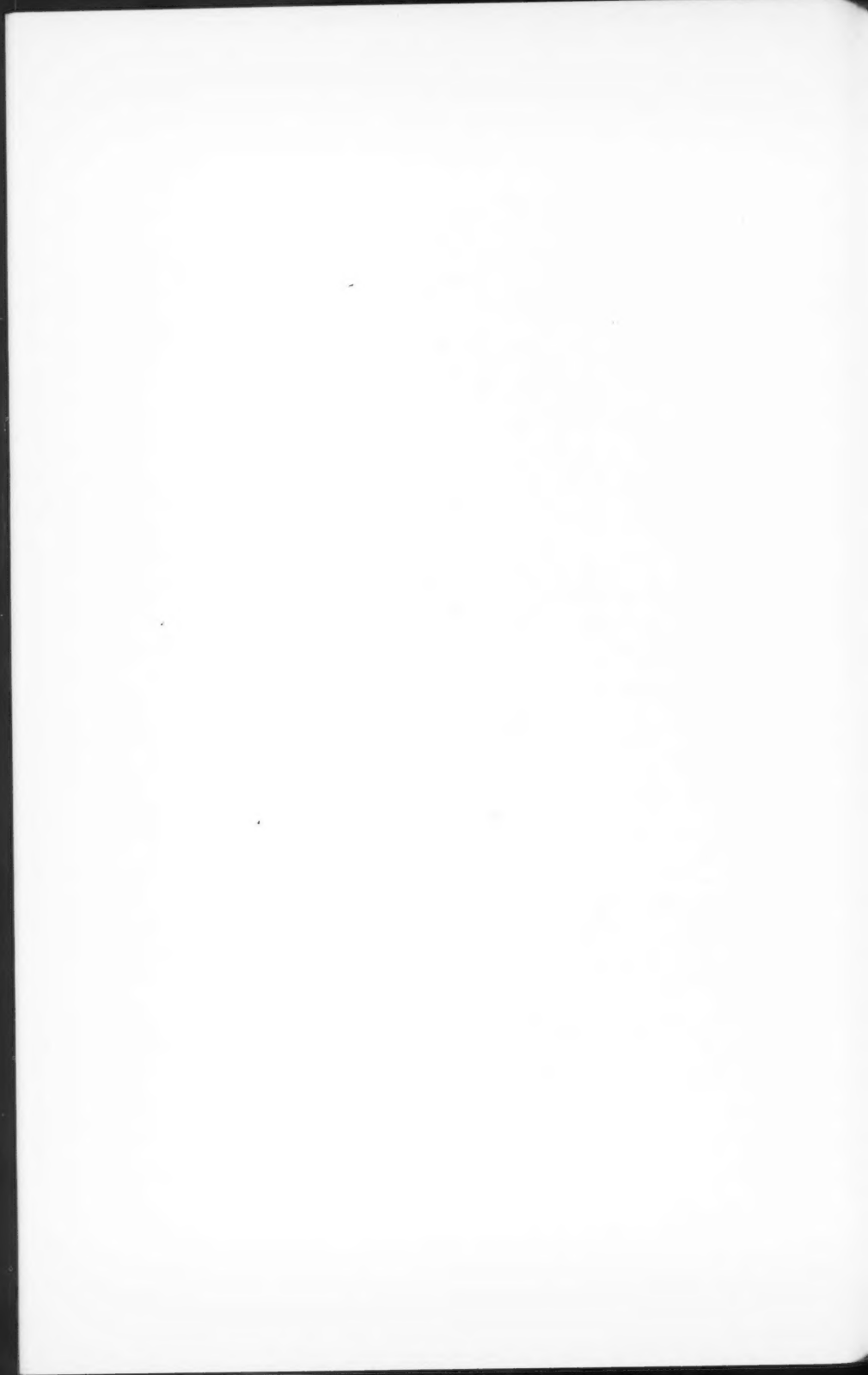


FIG. 1. New nitrogen transition at 1589.745 Å.



$^2\Sigma_u^+$ states is undoubtedly the upper state of the $C^2\Sigma \rightarrow X^2\Sigma$ system; one of the $^2\Sigma_u^-$ states could be the lower level of the new transition. If this is so the lower state of the new band should lie at about $65,000 \text{ cm}^{-1}$. Furthermore if it is a $^2\Sigma_u^-$ state it would be metastable with respect to all other known states of N_2^+ , which would explain the fact that hitherto it has escaped observation.

2. A transition to the ground state of N_2^+ ($v = 2$). Dr. A. E. Douglas pointed out to the author that the B'' value from the above analysis (1.8801 cm^{-1}) agrees very well with the B_2 value (1.879 cm^{-1}) for the ground state of N_2^+ . We might therefore tentatively identify the band as the 0-2 transition from a $^2\Sigma$ state at $67,220 \text{ cm}^{-1}$ to the ground state, $X^2\Sigma_g^+$. On this interpretation one would expect such bands at 0-0, 0-1, and 0-3 to be present as well. A search for these bands, however, proved negative. A further argument against this interpretation arises from the fact that $r' \sim r''$ so that one would expect the strongest bands of the system to lie in the 0-0 sequence. It is just possible, however, that the band is the 2-2 transition to the ground state of N_2^+ . This would satisfy the requirement that the strongest bands lie on the 0-0 sequence and it is conceivable that the strongest of these might be 2-2. Failure to observe other bands of the sequence might be due to relative weakness and overlapping by other structure.

3. A $^1\Sigma \rightarrow ^1\Sigma$ (ground state) transition of N_2^{2+} . This transition has been observed for the isoelectronic molecules C_2 and CN^+ . The Mulliken bands of C_2 form a headless system with $\nu_0 = 43,227.23 \text{ cm}^{-1}$ while the CN^+ bands of Douglas and Routly (1954) form a similar system with origin at $45,844.65 \text{ cm}^{-1}$. It is tempting to identify the present transition as the analogue of these two systems. This interpretation, however, requires that N_2^{2+} have not only a remarkably stable ground state, but also an almost equally stable excited state. Because of Coulomb repulsion in a doubly ionized molecule one would expect the electronic states to be considerably less stable in general than those of the singly ionized or neutral molecule.

It can be seen from the present discussion that the assignment of the band cannot be made with any certainty. Other transitions to the states involved must be observed before a final decision can be taken.

In conclusion the author would like to express his indebtedness to Dr. G. Herzberg and Dr. A. E. Douglas for valuable discussions on the above problem and to Mr. J. Shoosmith for his expert assistance in operating the vacuum spectrograph.

- BRIX, P. and HERZBERG, G. 1954. Can. J. Phys. **32**, 110.
 CARROLL, P. K. 1956. Can. J. Phys. **34**, 83.
 DOUGLAS, A. E. and ROUTLY, P. M. 1954. Astrophys. J. **119**, 303.
 GAYDON, A. G. 1944. Proc. Roy. Soc. A, **182**, 286.
 HERZBERG, G. 1946. Phys. Rev. **69**, 362.
 LOFTHUS, A. 1956. J. Chem. Phys. **25**, 494.

RECEIVED AUGUST 12, 1958.
 DIVISION OF PURE PHYSICS,
 NATIONAL RESEARCH COUNCIL,
 OTTAWA, CANADA.

ERRATA AND SOME ADDITIONAL COMMENTS ON CRITICAL STUDY OF VIBRONIC INTERACTION CALCULATIONS*

ANDREW D. LIEHR

The use of an incorrect co-ordinate transformation to relate the cartesian symmetry co-ordinates of benzene to the appropriate internal symmetry co-ordinates invalidates the *numerical* results reported by Liehr (1955, 1957, 1958a) for the intensity of the ${}^1A_{1g} \rightarrow \{{}^1B_{1u}, {}^1B_{2u}\}$ benzene vibronic transitions. The corrected intensities are given in Tables I through IV.† As is readily apparent, although the quantitative results are somewhat improved, *the previous qualitative conclusions remain unchanged.*

TABLE I
CORRECTION OF LIEHR'S (1957) TABLE I

	Intensities calc. on basis of:			Experimental intensities
	Eq. (2)	Eq. (6)	Eq. (7)	
${}^1A_{1g} \rightarrow {}^1B_{1u}$	0.0636	0.0121	0.0167	0.094
${}^1A_{1g} \rightarrow {}^1B_{2u}$	0.000320	0.00586	0.00591	0.0014
${}^1A_{1g} \rightarrow {}^1B_{1u}$	199	2.06	2.83	67
${}^1A_{1g} \rightarrow {}^1B_{2u}$				

TABLE II
CORRECTION OF LIEHR'S (1957) TABLE II

Intensities calculated:				
With $Z_a = 1$ in eqs. (10) and (7)	Using Craig's screening assumption in eqs. (10) and (7), and $Z_a = \sqrt{2}$	Using assumption of zero overlap, etc. in eqs. (10) and (7), $Z_a = Z$	By Liehr (1955) and Liehr and Moffitt (1958) using either the normal or the Wilsonian sym- metry co-ordinates	
${}^1A_{1g} \rightarrow {}^1B_{1u}$	0.0065	0.040	0.013Z ²	0.10
${}^1A_{1g} \rightarrow {}^1B_{2u}$	0.0040	0.0015	0.0047Z ²	$\sim 10^{-2}f({}^1A_{1g} \rightarrow {}^1B_{1u})$
${}^1A_{1g} \rightarrow {}^1B_{1u}$	1.6	26	2.9	~100
${}^1A_{1g} \rightarrow {}^1B_{2u}$				

TABLE III
CORRECTION OF LIEHR'S (1957) TABLE III

	$\frac{f(s)}{f(s)}$ by:	Eq. (2)	Eq. (6)	Eq. (7)
${}^1A_{1g} \rightarrow {}^1B_{1u}$	0.128	0.185	0.184	
${}^1A_{1g} \rightarrow {}^1B_{2u}$	0.00748	3.51	4.43	

*Liehr (1957).

†For the algebraic details of the correction see Liehr (1958b). In Table I of this paper please read for D_{MS} the number -0.8836.

TABLE IV
CORRECTION OF LIEHR'S (1957) TABLE IV

		$\frac{f_{(6)}}{f_{(8)}}$ by:		
Eqs. (10) and (7)	Eqs. (10) and (7) with Craig's screening assumption	Eqs. (10) and (7) with zero overlap, etc.	Liehr (1955) and Liehr and Moffitt (1958) with internal symmetry co-ordinates	
$^1A_{1g} \rightarrow ^1B_{1u}$	0.32	0.90	0.85	2.8
$^1A_{1g} \rightarrow ^1B_{2u}$	4.9	1.3	4.7	—

Recently Pople and Sidman (1957) have utilized the Murrell and Pople (1956) semiempirical model to transcribe Herzberg and Teller's (1933) qualitative discussion of the forbidden bands of formaldehyde into a quantitative form. The success of their treatment is quite spectacular. It therefore appears that an unduly pessimistic attitude was expressed by the present author upon the basis of his benzene intensity studies (Liehr 1957).

As an illustration of the sensitivity of the calculations to the numerical values of the benzene electronic energy differences and the $^1A_{1g} \rightarrow ^1E_{1u}$ intensity utilized in the computation, we have presented in Table V the result of using the *experimental* energy differences and $^1A_{1g} \rightarrow ^1E_{1u}$ intensity in equations (2), (6), and (7) of Liehr (1957).

TABLE V
COMPARISON OF THE VARIOUS NON-EMPIRICAL INTENSITIES USING THE EXPERIMENTAL ENERGY DIFFERENCES (PARR, CRAIG, AND ROSS 1950) AND THE EXPERIMENTAL $^1A_{1g} \rightarrow ^1E_{1u}$ INTENSITY (HAMMOND AND PRICE 1955)

Intensities calc. on basis of:			
	Eq. (2)	Eq. (6)	Eq. (7)
$^1A_{1g} \rightarrow ^1B_{1u}$	0.171	0.0480	0.0527
$^1A_{1g} \rightarrow ^1B_{2u}$	0.000378	0.00695	0.00699
$^1A_{1g} \rightarrow ^1B_{1u}$	452	6.91	7.54
$^1A_{1g} \rightarrow ^1B_{2u}$			

HAMMOND, V. J. and PRICE, W. C. 1955. Trans. Faraday Soc. **51**, 605.

HERZBERG, G. and TELLER, E. 1933. Z. Physik. Chem. B, **21**, 410.

LIEHR, A. D. 1955. The interaction of vibrational and electronic motions in some simple conjugated hydrocarbons. Thesis, Harvard University, Cambridge, Mass. (*Corrected* copies of this thesis are available from the author upon request.)

— 1957. Can. J. Phys. **35**, 1123.

— 1958a. Z. Naturforsch **13a**, 311.

— 1958b. Z. Naturforsch **13a**, 596.

LIEHR, A. D. and MOFFITT, W. E. 1958. To be published.

MURRELL, J. N. and POPLE, J. A. 1956. Proc. Phys. Soc. (London), A, **69**, 245.

PARR, R. G., CRAIG, D. P., and ROSS, I. G. 1950. J. Chem. Phys. **18**, 1561.

POPLE, J. A. and SIDMAN, J. W. 1957. J. Chem. Phys. **27**, 1270.

RECEIVED MAY 20, 1958.

BELL TELEPHONE LABORATORIES, INCORPORATED,
MURRAY HILL, NEW JERSEY.

RADICAL SPECTRA AT LIQUID HELIUM TEMPERATURES*

G. WILSE ROBINSON AND MACLYN McCARTY, JR.

Recently we reported on the electronic absorption spectra of certain radicals trapped in an argon matrix at 4.2° K (Robinson and McCarty 1958 *a, b*). Figures 1 and 2 show the results of some of this preliminary work in regard to the NH₂, HNO, OH, and NH radicals. The photographs were made in the first order of a 2-meter, 15000-line per inch grating instrument. Many of the observed absorption "bands" are surprisingly sharp, especially those of NH₂, which are only about 3 cm⁻¹ wide. Because of environmental perturbations of the ground and excited electronic states, the spectra of all the molecules studied exhibit "matrix shifts" of upward to 300 cm⁻¹. These shifts may be either to the red or to the blue with respect to the gas phase bands. The spectrum of trapped HNO clearly shows a number of fine structure features which are a result of interactions of the molecular motion with the lattice. Besides the three strong bands which we reported previously, three additional bands belonging to HNO have been found in the solid phase spectrum at 6445.9 Å, 6255.6 Å, and 5899.6 Å. These transitions involve the excited state vibrational levels $\nu_2 + \nu_3$, $2\nu_2$, and $2\nu_2 + \nu_3$.

Thirteen of the sharp absorption lines have now been correlated with the flash photolysis spectrum of NH₂ (Ramsay 1957), and these account for all the lines of strong and medium intensity expected in the 4000–7000 Å region, as well as for a few weak ones. Rotational structure in the electronic spectrum of trapped NH₂ indicates that this molecule is experiencing nearly free end-over-end rotation in the matrix phase. Fine structure in the OH ($A^2\Sigma^+ \leftarrow X^2\Pi_{3/2}$) and NH ($A^3\Pi \leftarrow X^3\Sigma^-$) bands is very likely associated with somewhat more hindered motions of these molecules, since there is poorer correlation with the gas phase rotational levels. In NH₂ the relative strength of the absorption from the first excited rotational level ($0_0 + 21.1 \text{ cm}^{-1}$) shows an actual population which is about 100-fold that expected for thermal equilibrium at 4.2° K. The level is metastable because of the $s \leftrightarrow a$ selection rule for exchange of identical nuclei, but the rotational part of this selection rule is expected to be somewhat relaxed because of electron and nuclear spin interactions with the molecular rotation. A weak absorption line occurs at 30466 cm⁻¹ which is attributed tentatively to trapped NH radicals in the metastable $a^1\Delta$ electronic state. The photographs show the presence of emission lines associated with the $A^3\Pi \leftarrow X^3\Sigma^-$ absorption band of trapped NH. The emission results from resonance fluorescence from the low-lying rotational levels in the $A^3\Pi$ state. No evidence has been found as yet for CH₂, HO₂, BH₂, or HCO, but current efforts are expected to yield fruitful results for at least some of these species.

*Work supported in part by the OOR, U.S. Army under Project No. TB2-0001 of Contract No. DA-36-034-ORD-2169.

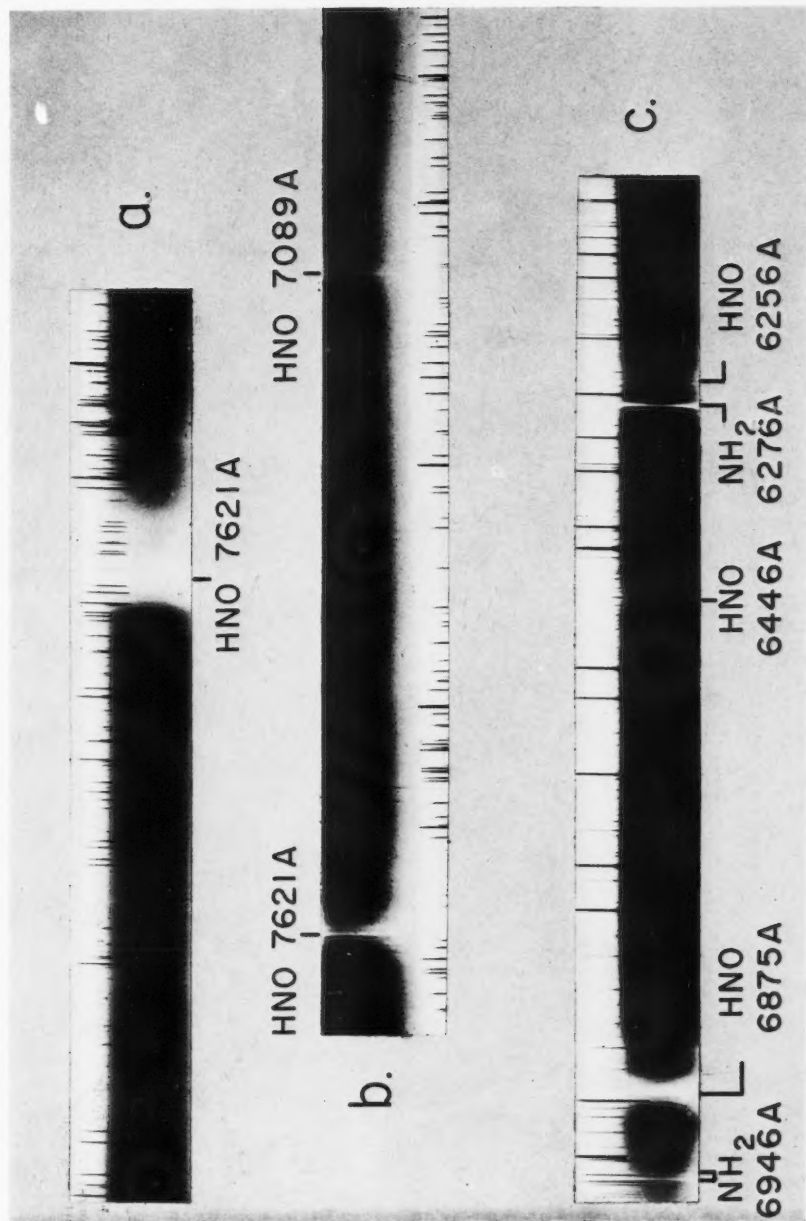


FIG. 1. Trapped radicals from argon-hydrazine discharge containing a trace of water and oxygen. Deposit times: (a) 10 hours; (b) 1 hour; (c) 10 hours, showing the 9.4 cm^{-1} spin doublet of NH_2 at 6946 \AA .

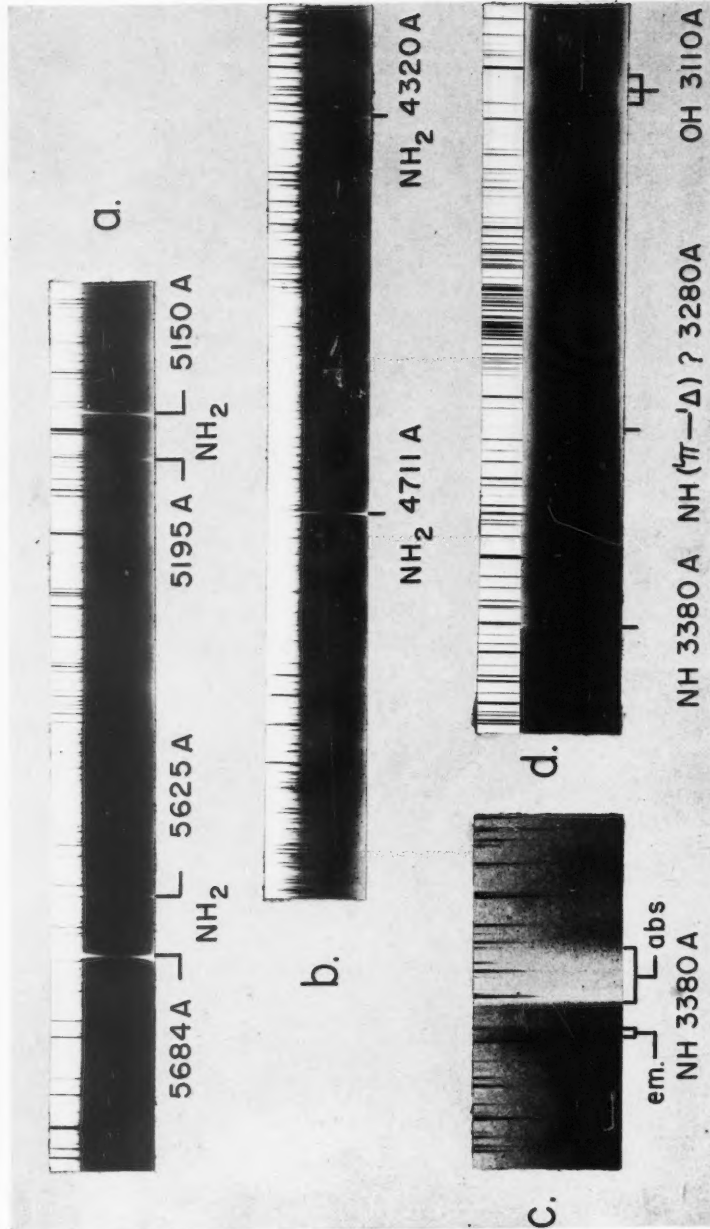


FIG. 2. Trapped radicals from argon-hydrazine discharge containing a trace of water and oxygen. Deposit times: (a) 10 hours; (b) 10 hours; (c) 2 hours; (d) 30 minutes. The complex structure in (b) is NO₂. When the oxygen impurities are removed the bands of HNO₃, NO₂, and OH are absent.

Because of the relatively unperturbed condition in which small molecules can be trapped at liquid helium temperatures, the technique should prove to be a very useful one for the study of diatomics and simple polyatomics throughout the entire optical region of the spectrum. Studies of this type should be especially valuable in the vacuum ultraviolet and the infrared regions where little is known about free radical spectra.

Details concerning some of our low temperature free radical work will be published shortly in another journal.

RAMSAY, D. A. 1957. *Mém. soc. roy. sci. Liège*, **18**, 471.
ROBINSON, G. W. and McCARTY, M., JR. 1958a. *J. Chem. Phys.* **28**, 349.
— 1958b. *J. Chem. Phys.* **28**, 350.

RECEIVED APRIL 3, 1958.
DEPARTMENT OF CHEMISTRY,
THE JOHNS HOPKINS UNIVERSITY,
BALTIMORE, MARYLAND.



THE PHYSICAL SOCIETY

MEMBERSHIP of the Society is open to all who are interested in Physics. FELLOWS pay an Entrance fee of £1 1s. (\$3.00) and an Annual Subscription of £2 2s. (\$6.00).

STUDENTS: A candidate for Studentship must be between the ages of 18 and 26, and pays an Annual Subscription of 5s. (\$0.75).

MEETINGS: Fellows and Students may attend all Meetings of the Society including the annual Exhibition of Scientific Instruments and Apparatus.

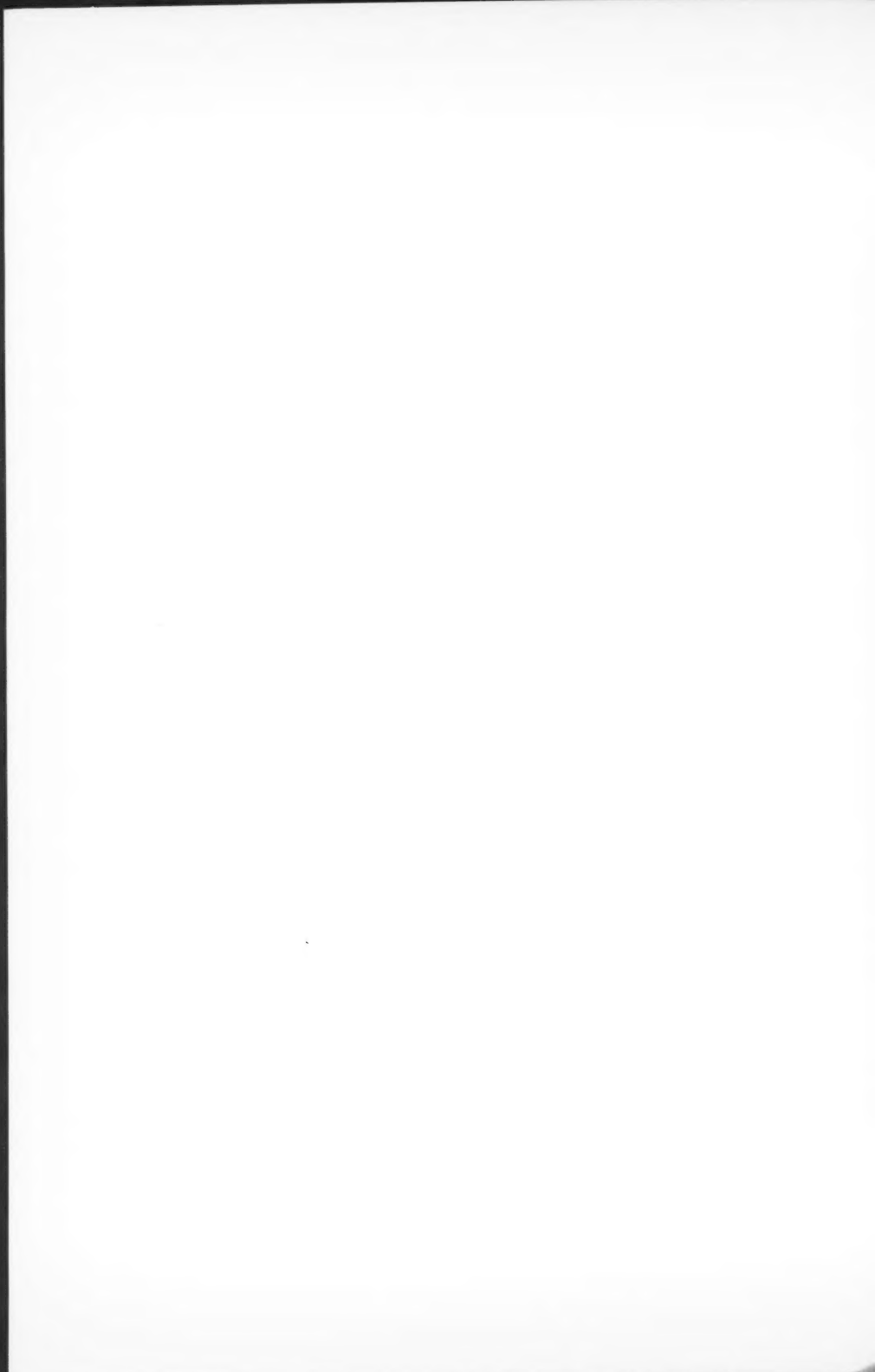
PUBLICATIONS include the *Proceedings of the Physical Society*, published monthly, and *Reports on Progress in Physics*, published annually. Volume XX, 1957, is now available (price £3 3s. (\$9.00)). Members are entitled to receive any of the Publications at a reduced rate.

Further information can be obtained from:

THE PHYSICAL SOCIETY
1, LOWTHER GARDENS, PRINCE CONSORT ROAD
LONDON, S.W.7, ENGLAND







CANADIAN JOURNAL OF PHYSICS

Notes to Contributors

Manuscripts

(i) **General.** Manuscripts, in English or French, should be typewritten, double spaced, on paper $8\frac{1}{2} \times 11$ in. **The original and one copy are to be submitted.** Tables and captions for the figures should be placed at the end of the manuscript. Every sheet of the manuscript should be numbered.

Style, arrangement, spelling, and abbreviations should conform to the usage of recent numbers of this journal. Names of all simple compounds, rather than their formulas, should be used in the text. Greek letters or unusual signs should be written plainly or explained by marginal notes. Superscripts and subscripts must be legible and carefully placed.

Manuscripts and illustrations should be carefully checked before they are submitted. Authors will be charged for unnecessary deviations from the usual format and for changes made in the proof that are considered excessive or unnecessary.

(ii) **Abstract.** An abstract of not more than about 200 words, indicating the scope of the work and the principal findings, is required, except in Notes.

(iii) **References.** References should be listed **alphabetically by authors' names**, unnumbered, and typed after the text. The form of the citations should be that used in current issues of this journal; in references to papers in periodicals, titles should not be given and only initial page numbers are required. The names of periodicals should be abbreviated in the form given in the most recent *List of Periodicals Abstracted by Chemical Abstracts*. All citations should be checked with the original articles and each one referred to in the text by the authors' names and the year.

(iv) **Tables.** Tables should be numbered in roman numerals and each table referred to in the text. Titles should always be given but should be brief; column headings should be brief and descriptive matter in the tables confined to a minimum. Vertical rules should not be used. Numerous small tables should be avoided.

Illustrations

(i) **General.** All figures (including each figure of the plates) should be numbered consecutively from 1 up, in arabic numerals, and each figure referred to in the text. The author's name, title of the paper, and figure number should be written in the lower left corner of the sheets on which the illustrations appear. Captions should not be written on the illustrations (see Manuscripts (i)).

(ii) **Line Drawings.** Drawings should be carefully made with India ink on white drawing paper, blue tracing linen, or co-ordinate paper ruled in blue only; any co-ordinate lines that are to appear in the reproduction should be ruled in black ink. Paper ruled in green, yellow, or red should not be used. All lines should be of sufficient thickness to reproduce well. Decimal points, periods, and stippled dots should be solid black circles large enough to be reduced if necessary. Letters and numerals should be neatly made, preferably with a stencil (do NOT use typewriting) and be of such size that the smallest lettering will be not less than 1 mm high when reproduced in a cut 3 in wide.

Many drawings are made too large; originals should not be more than 2 or 3 times the size of the desired reproduction. Whenever possible two or more drawings should be grouped to reduce the number of cuts required. In such groups of drawings, or in large drawings, full use of the space available should be made; the ratio of height to width should conform to that of a journal page ($4\frac{1}{2} \times 7\frac{1}{2}$ in), but allowance must be made for the captions.

The original drawings and one set of clear copies (e.g. small photographs) are to be submitted.

(iii) **Photographs.** Prints should be made on glossy paper, with strong contrasts. They should be trimmed so that essential features only are shown and mounted carefully, with rubber cement, on white cardboard, with no space between them. In mounting, full use of the space available should be made to reduce the number of cuts required (see Illustrations (ii)). Photographs or groups of photographs should not be more than 2 or 3 times the size of the desired reproduction.

Photographs are to be submitted in duplicate; if they are to be reproduced in groups one set should be mounted, the duplicate set unmounted.

Reprints

A total of 50 reprints of each paper, without covers, are supplied free. Additional reprints, with or without covers, may be purchased at the time of publication.

Charges for reprints are based on the number of printed pages, which may be calculated approximately by multiplying by 0.6 the number of manuscript pages (double-spaced type-written sheets, $8\frac{1}{2} \times 11$ in) and including the space occupied by illustrations. An additional charge is made for illustrations that appear as coated inserts. Prices and instructions for ordinary reprints are sent out with the galley proof.

Any reprints required in addition to those requested on the author's reprint requisition form must be ordered officially as soon as the paper has been accepted for publication.

Contents

<i>L. G. Bonar and G. B. Craig</i> —Activation energy for creep of tin	1445
<i>J. M. Robson</i> —The electron neutrino angular correlation in the beta decay of the free neutron	1450
<i>A. E. Scheidegger and V. C. Larson</i> —Asymmetry of the concentration front during miscible displacement in porous media	1476
<i>Carl Dahlstrom, J. S. Foster, and A. L. Thompson</i> —Discovery of Pr ¹³⁷	1483
<i>G. T. Danby, J. S. Foster, and A. L. Thompson</i> —Successive decays from Pr ¹³⁷ and Ce ^{137m} : Decay of adjacent praseodymium isotopes	1487
<i>E. R. Niblett</i> —The stability of couette flow in an axial magnetic field	1509
<i>K. Suryanarayana Rao</i> —Rotational analysis of ¹⁸ He γ system of the PO molecule	1526
<i>R. L. Williams</i> —Properties of cadmium sulphide photoconductive cells	1536
<i>D. P. Jatar</i> —Space charge relations for the low-frequency silent electric discharge in hydrogen	1551
<i>V. Venkateswara Rao and P. Tiruvenganna Rao</i> —The visible emission spectrum of the Cl ₂ ⁺	1557
<i>R. E. Burgess</i> —Polarization fluctuations in a ferroelectric crystal	1569
Notes:	
<i>A. S. Denholm</i> —Millimicrosecond pulses for checking fast transient analyzers	1582
<i>P. K. Carroll</i> —A new transition in molecular nitrogen	1585
<i>Andrew D. Liehr</i> —Errata and some additional comments on critical study of vibronic interaction calculations	1588
<i>G. Wilse Robinson and Maclyn McCarty, Jr.</i> —Radical spectra at liquid helium temperatures	1590

